Title

Egocentric and Episodic Navigational Maps in Dendrites and Somata of Posterior Parietal Cortex and Dorsal Hippocampus

Author

Moore, Jason James

Publication Date

2016

Peer reviewed|Thesis/dissertation

UNIVERSITY OF CALIFORNIA

Los Angeles

Egocentric and Episodic Navigational Maps in Dendrites and Somata of Posterior Parietal Cortex and Dorsal Hippocampus

A dissertation submitted in partial satisfaction of the

requirements for the degree Doctor of Philosophy

in Neuroscience

by

Jason James Moore

2016

ABSTRACT OF THE DISSERTATION

Egocentric and Episodic Navigational Maps in Dendrites and Somata of

Posterior Parietal Cortex and Dorsal Hippocampus

by

Jason James Moore

Doctor of Philosophy in Neuroscience

University of California, Los Angeles, 2016

Professor Mayank R. Mehta, Chair

The hippocampus is a brain structure critical for the formation of new memories. Case studies have demonstrated that a properly functioning hippocampus is required to form new episodic memories. But hippocampal cellular electrophysiology has traditionally studied hippocampal function by quantifying the role of the hippocampus in navigation and spatial localization through "place cells." The mechanisms through which allocentric spatial representations arise from egocentric sensory cues are not well-understood, nor are the ways in which these representations are used to navigate or relate to episodic memory. This dissertation addresses three key issues in understanding the mechanisms of episodic memory.

First, *in vivo* electrophysiology has traditionally focused on somatic spiking as the output of the brain structures under study, completely ignoring the activity in the massive dendritic arbors that

neurons maintain, and which have been proposed to have important contributions to neural computation. Here we describe development of a novel recording method and report the first long-term recordings during unrestrained, natural behavior of cortical dendritic activity representing egocentric motion. Second, confounds between different sensory or behavioral parameters can lead to problems in interpreting analyses when traditional methods of determining neural receptive fields are used. This work develops and applies powerful statistical analyses known as generalized linear models to identify the independent contributions of different sensory modalities to hippocampal tuning. Finally, in vivo electrophysiology has never been performed in the Morris Water Maze, one of the most widely-used behavioral tests of spatial memory, largely due to the incompatibility of water with recording electronics. By training rats to do an analogous task in virtual reality, we demonstrate that hippocampal pyramidal cells, which function as place cells in most environments, do not encode allocentric position in this task, but rather encode episodic distance within trials.

This multiple-level investigation of episodic memory, from cortical dendrites to hippocampal soma, is facilitated by novel technologies and methods. Each level of analysis reveals important new details of the computational principles utilized by neural circuits, and lead us to a more complete understanding of episodic memory.

The dissertation of Jason James Moore is approved.

Hugh T. Blair

Dean Buonomano

Thomas J. O'Dell

Mayank R. Mehta, Committee Chair

University of California, Los Angeles

2016

Dedication

To my family and friends, for supporting and guiding me, for laughing and crying with me, for working and relaxing with me, for simply being with me on this journey, and for teaching me the deep importance of personal connection. Familial bonds and friendship mean more to me now than when I started, and I am thankful to know that I have both.

Table of Contents

Dedication v

Table of Contents vi

List of Figures and Tables xi

Acknowledgments and Preface xiv

Vita xviii

1. Introduction 1

2. General Methods 4

Subjects 4

Tetrodes 5

Extracellular Recording 5

Extracellular Unit Classification 6

Virtual Reality 7

Quantification of Neural Responses 8

Constructing Rate Maps 8

Selectivity Quantification 9

Information Content 9

Sparsity 10

Dispersion 10

Coherence 10

Mean Vector Length 10

Statistics 10
Significance Tests 10
Confidence Intervals 11

3. In vivo intracellular dendritic dynamics in neocortex 12

Abstract 12
Introduction 12
Results 15
DAP vs extracellular spikes 15
Mechanism of DMP recording, glial sheath hypothesis 18
bAP vs DAP 21
Subthreshold dendritic potential dynamics during SWS 24
Dendritic sub- and supra-threshold membrane potential during unrestrained behavior 27
Modulation of DAP, DMP, and soma by behavior 30
Conclusions 33
Discussion 34
Methods 38
Recording Procedure 38
Subjects: 38
Surgery and in vivo electrophysiology: 38
Behavior 39
Position tracking: 39
Rest box: 40
Random foraging: 40
Behavioral state identification: 40

Extracellular electrophysiology and spike sorting 41
Extracellular unit classification: 41
Complex spike index (CSI): 42
MUA estimation: 43
Amplitude Variation: 43
Dendritic detection and quantification 44
DAP Detection: 44
DAP Quantification: 44
Duration of Recording: 45
Peak Rate and Inter-spike Interval Calculations: 45
Impedance Spectroscopy: 45
Subthreshold Responses 47
Subthreshold Magnitude Estimation: 47
Initiation Range: 47
Voltage-Rate (V-R) Curve: 48
Goodness of Fit: 48
Solitary DAP Analysis: 49
Egocentric Responses 49
Position Tracking: 49
Construction of Egocentric Rate Maps: 49
Information Content: 50
Coherence: 51
Number of Dendrites: 51
Statistics 51
Significance Tests: 51
Confidence Intervals: 52
Validation of Detection Algorithm and Generation of Surrogate High Rate Data: 52
Extended Data Figures and Figure Legends 54

4. Hardware Development 68
Low-cost, Simple, Circuit Board for In-Vivo Stimulation 68
Motivation 68
Physical Constraints 69
Stimulator Design 71
Assembly and Cost 74
Proof of Concept 75
Tetrode Plating Protocols 79
5. Hippocampal somatic activity during random exploration in virtual reality 84
Generalized Linear Model to Separate Multiple Determinants of Firing 84
Generation of surrogate data to validate the GLM method 85
Non-parametric generation of simulated place fields 85
Parametric generation of simulated place fields 86
GLM Specifics 87
Spuriously High Pixels 87
Independence of Number of Bins on Reconstruction 89
Surrogate Data 91
Confounding Factors 93

Behavioral Bias 93

Firing Rate and Number of Spikes 95

Mitigation of Spurious Correlations 98

Implications for Future Analyses 101

6. Hippocampal neural dynamics in a virtual water maze 103

Introduction 103

The Virtual Water Maze 105

Behavioral Results 107

Allocentric Spatial Responses 108

Episodic Distance Selectivity 110

Head-Direction Selectivity 112

Modulation by Reward 114

Discussion 115

7. Conclusions 119

References 120

List of Figures and Tables

Figure 3-1 | Measurements of DAP in vivo. 16

Figure 3-2 | DAP are similar across all electrodes of a tetrode and stable for long periods. 19

Figure 3-3 | DAP are likely to be from pyramidal neurons but have much greater firing rates and stronger short-term plasticity. 22

Figure 3-4 | Large subthreshold membrane potential fluctuations modulate DAP rates during SWS. 26

Figure 3-5 | Large subthreshold membrane potential fluctuations modulate DAP rates during RUN. 28

Figure 3-6 | DAP show non-anticipatory egocentric responses. 31

Extended Data Table 3-1 | Comparison of Spike Types. 54

Extended Data Figure 3-1 | Distributions of somatic spikes, DAP and its derivatives. 55

Extended Data Figure 3-2 | Variability of DAP Width and Rise Time. 56

Extended Data Figure 3-3 | Proposed schematic of glial sheath mechanism of DAP recordings. 57

Extended Data Figure 3-4 | Reduction of MUA on tetrode channels with DMP signal. 59

Extended Data Figure 3-5 | Validation of DAP detection algorithm and separated nature of measured DAP. 60

Extended Data Figure 3-6 | Spiking properties and short term plasticity of pyramidal neurons, interneurons, and DAP. 61

Extended Data Figure 3-7 | Modulation of DAP by subthreshold membrane potentials. 62

Extended Data Figure 3-8 | Comparison of LFP and subthreshold DMP modulation during SWS and RUN. 64

Extended Data Figure 3-9 | Properties of solitary DAP in SWS and RUN. 65
Extended Data Figure 3-10 | Sample egocentric rate maps, evaluation of significance, additional measures, and long-term stability. 66
Figure 4-1 | Design and Assembly of Stimulator Board. 71
Figure 4-2 | Interfacing with NanoZ Connector. 72
Figure 4-3 | Interface with the EIB and Pre-Amplifier. 73
Figure 4-4 | Electrode Signals above 3 Hz are Unaffected by the Presence of the Stimulator 76
Figure 4-5 | No evidence of Cross-talk between Channels due to Stimulator 77
Figure 4-6 | Stimulation Modulates Multiunit Firing Rate 78
Figure 4-7 | Optical Characterization of Tetrodes with Different Plating Procedures 81
Figure 4-8 | SEM Characterization of Tetrodes with Different Plating Procedures 82
Figure 5-1 | Fixing Spuriously High Pixels in the GLM Output. 88
Figure 5-2 | GLM-Derived Sparsity is Unaffected by the number of Bins used for Reconstruction. 90
Figure 5-3 | Generation of Surrogate Data to Validate the GLM. 92
Figure 5-4 | Global Behavioral Biases. 94
Figure 5-5 | Effect of Behavioral Bias on Tuning. 96
Figure 5-6 | Dependence of Tuning on the Mean Firing Rate and the Number of Spikes. 97
Figure 5-7 | Correcting for Latent Correlations. 99
Figure 6-1 | The Virtual Water Maze Task. 106
Figure 6-2 | Trajectories are Efficient, Repeated, and Differ between Start Locations. 108
Figure 6-3 | CA1 Pyramidal Neurons Lack Allocentric Spatial Selectivity in the Virtual Water Maze. 109

Figure 6-4 | CA1 Pyramidal Neurons Show Strong Egocentric Distance Selectivity in the Virtual Water Maze. 111

Figure 6-5 | Head-direction Tuning in the Virtual Water Maze. 113

Figure 6-6 | Rate Modulation by Reward. 115

Acknowledgments and Preface

I thank everyone who has made this dissertation possible, either by directly contributing to the work or for being part of my reality. The act of writing a dissertation can be a fairly solitary, isolating process, but it has also made me keenly aware of the support I am thankful to have.

First, I want to thank my family, my mom Wendy, my dad Jim, and my brother Jeff. They have been nothing but supportive, understanding, and loving for my entire life. I know I always have them to lean on during rough times and to celebrate with during the good times. Mom, you have helped me through my lowest times. I cannot thank you enough for helping me reach this point.

I want to thank everyone in my cohort for making my graduate school experience what it was. I feel honored and grateful that I can call such bright and varied people my peers. I hope we can stay in touch as much as possible as we go to the next stage in our lives.

I particularly want to thank Lavanya and Zahra for their friendship. You both were a source of personal connection and joy in lab, even when we were slogging through endless paper revisions. Even though we don't see each other every day any more, you have taken the effort to stay in communication, which lets me know you care and that I have a friend in both of you. Thank you.

I also want to thank James Simonelli for being my friend, peer, fellow musician, and four-year apartment-mate. I am grateful for being able to decompress with you after a busy day, and for the fun adventures through these years.

All of the data presented here was recorded by Pascal Ravassard, Ashley Kees, David Ho, Lavanya Acharya, Jesse Cushman, and Cliff Vuong, who also trained all of the rats along with Briana Popeney, Ayaka Hachisuka, and a host of undergraduate researchers. Daniel Aharoni and Bernard Willers, senior lab members when I joined, built the virtual reality system from scratch. I thank Zahra M. Aghajan, who was my best source for discussing analysis techniques. I also want to thank Joe Dwyer, Paul Botros, Nick Ambrosio, Sam Yang, Vincent Tang, and David Khachatrian, the undergraduate researchers to whom I served as mentor. Everyone in lab has helped me develop as a scientist and a person; I thank you all and wish you nothing but the best.

I thank my committee for giving me guidance through their expertise, and encouraging me to pursue these difficult but rewarding projects.

Finally, I thank my mentor, Mayank Mehta, for the opportunity to grow as a researcher in this lab. I came into neuroscience as an outsider, and the quantitative, interdisciplinary nature of this lab has let me grow in directions I had not thought possible. I can attribute my resilience, ability to work independently, and attention to detail to my experiences in this lab, and I know they will serve me well in the future.

Additional thanks go to Sven Berberich and Thomas Hahn for use of histology images, and Felix Schweizer and Istvan Mody for discussion and careful reading of the material in Chapter Three.

Chapters Two and Three are adapted from

> Moore, J. J., Ravassard, P. M., Acharya, L., Kees, A. L., Vuong, C., Mehta, M.R. Dynamics of cortical dendritic membrane potential and spiking during natural behavior. Submitted.

Author contributions are as follows: J.J.M. designed analysis techniques, analyzed the data and wrote the paper; P.M.R., D.H., L.A., A.L.K., and C.V. trained and implanted the rats and collected the data. M.R.M. designed analysis techniques and wrote the paper. All authors discussed the results and commented on the manuscript.

Chapter Five includes material from

> Acharya, L., Aghajan, Z. M., Vuong, C., Moore, J. J., Mehta, M. R. Causal Influence of Visual Cues on Hippocampal Article Causal Influence of Visual Cues on Hippocampal Directional Selectivity. Cell 164, 197–207 (2016). doi: 10.1016/j.cell.2015.12.015.

Author contributions are as follows: Conceptualization, L.A., Z.M.A., and M.R.M.; Methodology, L.A., C.V., and M.R.M.; Software, Z.M.A. and J.J.M.; Formal Analysis, Z.M.A.; Investigation, L.A. and C.V.; Writing – Original Draft, L.A., Z.M.A., J.J.M., and M.R.M.; Writing – Review & Editing, L.A., Z.M.A., J.J.M., and M.R.M.; Visualization, Z.M.A.; Supervision, M.R.M.; Project Administration: M.R. M.; Funding Acquisition, M.R.M.

Figure 5-3 is an adaptation of Figure S1 from the above publication, and the section “Generation of surrogate data to validate the GLM method” is an excerpt of the Supplemental Experimental Procedures section of the same publication.

Chapter Six contains material to be used in

> Moore, J. J., Cushman, J. D., Acharya, L., Vuong, C., Mehta, M. R. Hippocampal neural dynamics in a virtual Morris water maze navigation task. *In preparation for publication.*

Author constibutions are as follows: Conceptualization, J.D.C, L.A., C.V., J.J.M., and M.R.M. Methodology, J.D.C, L.A., C.V., and M.R.M.; Software, J.J.M.; Formal Analysis, J.J.M..; Investigation, J.J.M., C.V., and M.R.M.; Writing – Original Draft, J.J.M., and M.R.M.; Writing – Review & Editing, J.J.M., C.V., J.D.C., L.A., and M.R.M.; Visualization, J.J.M.; Supervision, M.R.M.; Project Administration: M.R. M.; Funding Acquisition, M.R.M.

Sources of funding include grants to Mayank R. Mehta from the W. M. Keck Foundation, the Whitehall Foundation, NSF Career #0969034 and NIH #1-R01-MH-092925, as well as the NIH Neural Microcircuits Training Grant, and the BRI/Semel Institute Neuroscience Graduate Travel Award.

Vita

Education	**University of California, San Diego, Jacobs School of Engineering (UCSD)** Bachelor of Science in Computer Science Graduated Summa cum Laude	**6/09**
Publications	**Dynamics of cortical dendritic membrane potential and spiking during natural behavior** **Moore, J. J.**, Ravassard, P. M., Acharya, L., Kees, A. L., Vuong, C., Mehta, M.R. (2015)	**In Review**
	Causal Influence of Visual Cues on Hippocampal Directional Selectivity Acharya, L., M. Aghajan, Z., Vuong, C., **Moore, J. J.**, Mehta, M. R. (2016). *Cell* **164,** 197–207.	**1/16**
	Impaired spatial selectivity and intact phase precession in two-dimensional virtual reality Aghajan, Z. M., Acharya, L., **Moore, J. J.**, Cushman, J. D., Vuong, C., Mehta, M. R. (2015). Nature Neuroscience. 2015 Jan; 18(1):121-8.	**1/15**
Invited Talks and Panels	**STEM Career Panelist** Santa Monica College Cool Careers STEM Panel	**11/15**
	Dendrites and virtual reality: Novel recording and behavioral techniques using tetrodes in freely behaving animals Stanford University – Schnitzer Lab Seminar	**1/15**
	Dendritic recordings in freely behaving animals UCLA Neuroscience IDP Retreat	**5/14**
	Long-term *in-vivo* dendritic recording UCLA Neuroscience After-hours Research Forum	**6/13**
	Long-term recording of putative dendritic spikes in the neocortex of freely behaving animals UCLA Neurobiology Retreat	**5/13**

Posters and Presentations

Hippocampal neural dynamics in a virtual Morris water maze navigation task

- UCLA's 10th Annual Symposium for Neural Microcircuits **5/16**
- UCLA Brain Research Institute (BRI) Neuroscience Poster Session **11/15**
- Society for Neuroscience Conference 2015 **10/15**

Behavioral modulation of neocortical dendritic spikes in freely behaving rats

- 2015 Joint Symposium on Neural Computation, USC **5/15**
- UCLA's 9th Annual Symposium for Neural Microcircuits **5/15**
- UCLA BRI Neuroscience Poster Session **12/14**
- Society for Neuroscience Conference 2014 **11/14**

Dendritic spiking and subthreshold membrane potential of cortical neurons during slow-wave-sleep in unanesthetized animals

- UCLA's 8th Annual Symposium for Neural Microcircuits **5/14**
- Society for Neuroscience Conference 2013 **11/13**

Long-term recording of putative dendritic spikes in the neocortex of freely behaving animals

- UCLA BRI Neuroscience Poster Session **12/12**
- Society for Neuroscience Conference 2012 **10/12**

Awards and Funding

UCLA BRI/Semel Institute Neuroscience Graduate Travel Award **6/15**

- Competitive departmental travel grant: **$400**

UCLA Neural Microcircuits Training Grant **6/14**

- Competitive NIH-Funded training grant: **$11,000**

UCLA Regents Stipend: **5/13**

- UCLA Graduate Division award: **$5000**

UCLA Chancellor's Prize **9/09**

- UCLA Graduate Division award: **$10,000**

Teaching and Mentoring

Entering Mentoring Training Program **8/15**

Teaching Assistant – Neurophysics of the Mind-Brain Problem **1/15 – 4/15**

Graduate Student Advisor to Undergraduate Students **1/12 – 8/15**

1. Introduction

The hippocampus is a brain structure critical for the formation of new memories. Case studies like the famous patient HM first demonstrated that a properly functioning hippocampus is required to form new declarative and episodic memories[1]. Episodic memories, such as where you went to elementary school or the path you took from your house to work today, have two key components to them. First, they are spatiotemporally positioned at a particular place and at a particular time. Second they typically involve the subjective viewpoint of the person with the memory. Behavioral testing has clearly shown the important of the hippocampus in spatial and episodic memory[2,3], but cellular electrophysiology has traditionally approached hippocampal function from an entirely different angle.

Electrophysiological studies have revealed the presence of "place cells" in the dorsal hippocampus[4–6]. These are neurons that become very active in only a small segment of any given environment, and are otherwise silent. Much work has been spent studying the impact of visual[7–9], olfactory[10,11], auditory[12], and tactile[13] cues, as well as differing task type[14,15], on the properties of these place cells and their changes with experience[16,17]. Place cells are thought to represent an abstract notion of allocentric space, and behavioral measurements of spatial navigation assume an allocentric cognitive map supporting behavior. Though well-studied, many properties of place cells are still unknown, particularly what defines "place," how allocentric space is computed from egocentric movements and sensations[18,19], and how such a code for space might be used to navigate[20].

All sensory information that comes in to the brain is necessarily in an egocentric, or self-centered, reference frame. The sights we see, the sounds we hear, the smells we smell, all depend

on the relative orientation and distance between ourselves and any given object. All motor output, too, is necessarily represented in an egocentric reference frame. We must move forward or backward from our current position or rotate to change our current orientation. The mechanisms of interaction between self-referenced sensorimotor information and the allocentric map of space in the hippocampus, as well as the computational principles that underlie these interactions, are not well-understood.

This work capitalizes on the use of new electrophysiological, statistical, and behavioral methods that allow researchers to address questions previously out of reach, and to begin to link the realms of *in vivo* electrophysiology and episodic memory. Three key roadblocks have stood in the way of answering these questions.

First, *in vivo* electrophysiology thus far has focused on somatic spiking as the output of the brain structures under study. But principal neurons maintain vast dendritic arbors with a variety of nonlinear voltage gated ion channels. The impact of these active dendrites on the computations described above has not at all been characterized, though theoretical work suggests they may be vitally important to network behavior[21–25]. Our development of novel electrode recording techniques allows us to directly measure the sub- and supra-threshold voltages of these dendrites.

Second, interactions between different sensory or behavioral parameters can lead to problems in interpreting analyses when traditional methods of determining neural receptive fields are used[14,26–28]. Hence, it is most straightforward to manipulate only one parameter (space, head angle, context, etc.) at a time and attempt to clamp all other variables. Only the most carefully designed experiments have been able to investigate the joint or independent contributions of

multiple parameters on neural firing. By utilizing a class of statistical models known as generalized linear models, we are better able to dissociate these parameters.

Finally, one of the most widely-used behavioral tests of spatial memory, the Morris Water Maze[29,30], has not been able to be combined with *in vivo* electrophysiology. This can be attributed to a number of reasons, not least of all the incompatibility of water with recording electronics[31–33]. Place cells are supposed to make up the "cognitive map" of an environment[5], and it is this cognitive map that is supposed to support spatial learning and memory, but the direct link between spatiotemporal hippocampal activity and spatial memory has not been established. Using Virtual Reality technology[34–37], we are able to construct a virtual water maze compatible with electrophysiological recordings, allowing us to link cellular dynamics with behavior.

This work investigates spatial navigation from the dendritic level in neocortex to the cellular level in hippocampus to episodic memory-related behavior. Novel technologies and methods facilitate this multiple-level analysis of memory and behavior, revealing important computational principles along the way.

2. General Methods

Subjects

Data were obtained from singly housed adult male Long-Evans rats, 350-425g at the time of surgery, trained to perform the spatial exploration tasks described below. The animals were water restricted (minimum of 30mL/day) in order to increase motivation to perform tasks, and received sugar water or solid cereal rewards during spatial exploration tasks. Further, they were food restricted (minimum of 15g/day) to maintain a stable body-weight and increase motivation to perform tasks with food reward. All experimental procedures were approved by the UCLA Chancellor's Animal Research Committee and in accordance with NIH-approved protocols.

Rats with satisfactory behavioral performance on spatial exploration tasks were anesthetized using isoflurane and implanted with custom-made hyperdrives with 22 independently adjustable tetrodes. Four rats were implanted with drives targeting right prefrontal cortex and right posterior parietal cortex and dorsal CA1 of the hippocampus. All others were implanted with drives targeting both left and right dorsal CA1 and the posterior parietal cortex above it. After recovery from surgery, all tetrodes were slowly lowered through cortex over a span of several days to months. Subsets of tetrodes were advanced daily, typically ~70μm and rarely more than 140μm in one day.

Tetrodes

Extracellular Recording

All electrophysiological recording was performed with tetrodes, bundles of 4 wires constructed in-house from 13 µm-diameter NiChrome (NiChr) wire coated with 2 µm thick polyimide insulation. After the tetrodes were cut, the tips were electroplated with a gold particle solution containing 75% gold plating solution and 25% multi-walled carbon nanotube solution.

Electroplating is performed in order to reduce the impedance of the recording electrodes. The impedance is measured as the total impedance between the amplifier and ground. When preparing tetrodes, the largest source of impedance, and the easiest to manipulate, is the impedance of the electrode-electrolyte interface. Impedance is a frequency-dependent quantity, and is typically measured at 1 kHz, the typical frequency of an extracellular action potential. An unplated NiChr electrode has an impedance of several MΩ.

Because the resistance of the amplifier (~ 1 TΩ) is several orders of magnitude larger than the electrode-electrolyte impedance, changes to the electrode impedance do not affect overall signal amplitude. The motivation for plating comes from reducing the thermal noise, also termed Johnson Noise, arising from the resistance. A lower impedance allows the recording of a large amount of neurons, critical for investigating population-level dynamics

A current of 150 nA was passed for 2 seconds with the electrode tip as the anode. This was repeated until the impedance at 1 kHz decreased below 130 kΩ for each electrode of every tetrode. Additional checks ensured that the four channels of a tetrode were not shorted.

Signals were recorded using a Neuralynx data acquisition system at a sampling rate of 32 or 40 kHz; all signals were initially digitally filtered through a 32 tap low-pass FIR filter with a cutoff frequency of 9000 Hz and a high-pass DC offset filter with a cutoff frequency of 0.1 Hz.

Slow fluctuations in the signal (<100 Hz) typically represent the local field potential (LFP), thought to represent the summed input to a brain region, and is typically synchronous over large areas. This signal is typically no more than several hundred μV in amplitude. Somatic action potentials are extracellularly visible as fast (~1000 Hz) spikes in the signal. These correspond to the current going into and coming out of the soma. A single tetrode may record spikes from up to 30 nearby neurons.

Extracellular waveforms were extracted from the LFP filtered between 300 and 9000 Hz with a zero-phase second order Butterworth bandpass filter. Peaks with values above an adaptive threshold based on the magnitude of the noise in the signal (typically >40 μV) were identified as putative somatic action potentials.

Extracellular Unit Classification

Spike sorting and single unit classification were done offline using custom software. We take advantage of the different amplitudes of spikes on the different channels of a tetrode to perform spike sorting. Several features of each spike are computed, including peak amplitude, trough amplitude, and valley amplitude, as well as principle components computed from these measures. Spikes from a single neuron will cluster along these dimensions, and spikes are assigned to different neurons by manually drawing boundaries in different projections of these dimensions. Though time-consuming, this process ensures that all units used for analysis are not

missing any spikes or are contaminated by spikes from other units, and faithfully represent the spiking activity of single neurons.

We used several metrics of a clustered unit to classify the putative neuron type of extracellular units into one of two broad categories of Pyramidal Neurons or Interneurons based on previous studies. Such features include mean firing rate, width at half-maximum, and time from spike peak to trough,

Complex spike index (CSI) is another feature used to differentiate pyramidal neurons from interneurons, especially in the hippocampus. For all pairs of adjacent spikes with spike time T_n and amplitude A_n and belonging to a single unit, the inter-spike-interval (ISI) was defined as

$$ISI = T_n - T_{n-1}$$

and the adaptation index (ADI) was defined as the ratio

$$ADI = \frac{A_n - A_{n-1}}{A_n + A_{n-1}}$$

The CSI was then computed as

$$CSI = 100 * \frac{S-L}{S+L}$$

where S is the number of spike pairs with ISI < 20 ms and ADI < 0, and L is the number of spike pairs with ISI < 20 ms and ADI >=0.

Virtual Reality

Virtual reality experiments are done using a custom-built system designed to isolate the contribution of different sensory modalities to behavior and neural responses. The rat is

harnessed atop a hollow, Styrofoam ball 1 meter in diameter. This provides body-fixation so the rat is always facing the same direction in the room frame of reference. The ball is floated on a cushion of air. When the rat moves, the ball rotates, and its rotation is tracked by laser sensors on the sides of the ball. This input is fed to a computer outside the room running the first-person virtual reality program. The visual scene is then projected via a polished, shaped mirror onto a screen that covers the rat's entire field of view. The room that we typically use has a 2 meter diameter table that is 75 centimeters above a virtual floor. The pattern on the table provides optic flow but has no local cues that could give information about space. The square virtual room is 4.5 by 4.5 meters, and the walls extend from the floor to 3.2 meters above the table. Each wall has a distinct visual cue on it. Thus only distal visual cues contain any information about position in the virtual environment, with no smells, sounds, or textures that are reliably associated with any position in the virtual world.

Quantification of Neural Responses

Constructing Rate Maps

To quantify the effect of any given stimulus or behavioral pattern has on a neuron, rate maps are constructed. The stimulus space is split up in to several (L) bins. The total number of spikes N in each bin is divided by the total time T spent in each bin to obtain an estimate of the mean firing rate λ of that neuron as a function of the stimulus space: $\lambda_i = \frac{N_i}{T_i}$

The firing rate plotted as a function of the entire stimulus space is referred to as the rate map. Given large amounts of data, this procedure generates an accurate representation of the neuron's response. However, experiments are finite in length (< 1 Hour), and some neurons may not fire

often enough to obtain an accurate representation of the true firing rate. The first way these problems are mitigated is to exclude bins in which insufficient time is spent. This avoids spuriously high firing rates in isolated regions of the stimulus space. The second way to address this problem is to "smooth" the rate maps, usually by convolving a Gaussian kernel with the rate map. This is motivated by the observation that neural responses are typically continuous within a stimulus space; that is, the firing rate of a neuron for stimuli close in the stimulus space will be similar.

The size of the bins used to construct the rate maps, the minimum occupancy time, and the size of the Gaussian smoothing kernel are all free parameters that may differ from experiment to experiment, depending on the amount of data available, affecting the minimum occupancy time, and the desired resolution, affecting bin size and smoothing size.

Selectivity Quantification

Once a rate map is constructed, there are several ways to quantify how "well-tuned" the neuron is to the given stimulus space. Each has strengths and weaknesses, and thus each provide different insights into the nature of neural responses.

Information Content

The information content of a single unit rate map (in bits) is defined as

$$I = \sum_{i}^{L} P_i \left(\frac{\lambda_i}{\bar{\lambda}}\right) \log_2 \frac{\lambda_i}{\bar{\lambda}}$$

Sparsity

Sparsity of a rate map given N bins and r_n as the rate in the n_{th} bin is defined as:

$$S = \sum_{i}^{L} P_i \left(\frac{\lambda_i}{\bar{\lambda}}\right)^2$$

Dispersion

The dispersion of a rate map is defined as the mean distance between the pixels with the highest 10% of all values.

Coherence

Coherence was calculated by evaluating the correlation coefficient between each pixel of a rate map and the mean of all surrounding pixels[45]. Pixels with undefined firing rate were excluded from this analysis.

Mean Vector Length

The mean vector length, for circular rate maps, is computed as:

$$MVL = abs\left(\frac{\sum_n^N r_n e^{-i\theta_n}}{\sum_n^N r_n}\right)$$

where θ_n and r_n are the angle and rate in the n_{th} circular bin respectively.

Statistics

Significance Tests

Due to the relatively small sample size of some datasets and potential non-Gaussian distribution of measures, we employed non-parametric tests and resampling statistics to assess statistical

significance. Significance between unpaired data was assessed using the Wilcoxon rank-sum test. Significance between paired data was assessed using the Wilcoxon signed-rank test. These tests make few assumptions about the distributions of data being tested and are robust to non-equal sample sizes or non-Gaussian nature of data. Correlation coefficients and their related significance were calculated using the built-in corrcoef() function in MATLAB, which calculates a two-sided *t* statistic to assess significance.

Confidence Intervals

Unless otherwise stated, all values are reported as median [95% confidence interval], in the form M [L, U], with M representing the median and L and U representing the lower and upper bounds, respectively, of the 95% confidence interval. Confidence intervals were estimated using resampling statistics to allow analysis of non-Gaussian distributions. Briefly, a surrogate population was constructed by drawing with replacement from the original distribution and the median of the resulting distribution recorded. This was repeated 100,000 times to form a distribution of the estimated median. The cutoff values of the 2.5^{th} and 97.5^{th} percentile of the estimated distribution were designated as the 95% confidence interval of the original population.

3. In vivo intracellular dendritic dynamics in neocortex

Abstract

Neural activity *in vivo* is primarily measured using extracellular somatic spikes, which provide limited information about neural computation. To understand neural dynamics it is necessary to measure the activity of difficult-to-record extensive neuronal dendrites, which possess voltage-gated ion channels supporting dendritic action potentials (DAP). Here we measured neocortical sub- and supra-threshold dendritic membrane potential (DMP) using tetrodes in freely behaving, drug-free rats over multiple days with a high degree of stability and sub-millisecond temporal resolution, which is unfeasible using other techniques. DMP exhibited digital spiking, i.e. DAP, with firing rates greatly exceeding somatic spike rates, suggesting that only a fraction of DAP contribute to somatic spiking. DAP rates were modulated by analog, subthreshold DMP fluctuations, which were far larger than the DAP amplitude even during locomotion, demonstrating interacting analog and digital dendritic computation *in vivo*. During unrestrained behavior, somatic spikes in parietal cortex encoded future egocentric movement. Egocentric maps were found in the DAP and DMP as well, but they were more diffuse and lacked the anticipatory component observed in somatic spikes. These results reveal surprising features of dendritic computations in parietal cortex during natural behavior.

Introduction

Microelectrode techniques have enabled the measurement of extracellular action potentials in drug-free subjects during natural behavior over long periods of time. However, action potentials

are brief (~1 ms), occur rarely (~1.5 Hz in principal neocortical neurons), and only represent the binary output of the somata, while their dendritic arbors span more than 1000 µm[38]. *In vitro* studies show that dendrites possess voltage-gated ion channels that support local spike initiation of dendritic action potentials (DAP)[21,39–49] and back-propagating action potentials (bAP) initiated at cell somata[42,44–46,50–53]. Further, they show that these nonlinear processes profoundly influence synaptic integration[42–44,53] and plasticity[47–49], and computational models show that this can alter circuit dynamics and information capacity of single neurons[21–25,54]. All of these effects can influence behavior and cognition, but the nature of sub- and supra-threshold dendrite dynamics during natural behavior, particularly those of electrotonically distal dendrites where the majority of excitatory synapses are localized, have remained largely elusive. Thus it is essential to measure the dendritic membrane potential (DMP) during natural behavior. Sharp electrode[39] or patch-clamp techniques[55] can measure intracellular subthreshold voltage from somata and proximal dendrites at sub-millisecond temporal resolution, but the damage caused by rupturing the membrane and dialyzing the intracellular medium limits the duration of recording allowed by these methods[56], may alter *in vivo* signal properties including firing rates[57], and is ill-suited to record from thin tertiary dendrites. Two-photon imaging techniques can estimate the dendritic calcium influx[53,58,59], but do not directly measure subthreshold membrane potential or dendritic sodium spikes and lack sub-millisecond resolution.

"In-cell" recording technique can measure intracellular voltage[60,61], where cells attempt to endocytose the recording electrodes, yielding a large seal resistance, allowing measurement of the intracellular voltage without the electrode penetrating the cell membrane, yielding positive polarity spikes as in patch-clamp recordings, as opposed to negative polarity spikes during extracellular measurements. *In vivo*, glial cells also engulf chronically implanted

microelectrodes, forming a high impedance glial sheath[62,63].The high impedance of the glial sheath also blocks the signals from surrounding neurons.

A similar technique is the use of "quasi-intracellular" recordings in anesthetized animals[64–68] where sharp glass pipettes occasionally measure intracellular like signals, including positive spikes riding on subthreshold potentials[65–67]. These recordings can be stable for at most a few hours[65]. Spikes measured with quasi-intracellular and patch-clamp techniques have identical shapes, of~1 ms width , typical of somatic recordings[65,67,68]. The proposed mechanism for quasi-intracellular recording is that a region of high electrical resistance electrically isolates the membrane under the microelectrode, resulting in a large, intracellular-like signal.

We hypothesized that a combination of tetrode technology, in-cell (quasi-intracellular) recording, and glial response to electrode implantation could provide high quality dendritic recordings *in vivo*. If a tetrode with four closely spaced (~4 µm) tips is positioned near a dendrite when the tetrode is encapsulated by the glial immune response the dendrite would become trapped between the tetrode tips; an equipotential region would then be formed in which the voltage at all four tips would closely match the intracellular DMP. This would be biased towards thin dendrites and not somata or proximal dendrites because thin dendrites could be cradled in the ~4 µm spacing between tetrode tips until the glial sheath forms, but cell somata and proximal dendritic trunks would be ruptured by the tetrode due to their large size. This is a different configuration than the in-cell recordings in cell cultures described above, but utilizes the same principle of increasing the seal resistance between the electrode and ground. Hence, we closely examined the signal properties of tetrodes *in vivo* to see if such "glial-assisted" recordings of

intracellular voltages could be achieved and maintained over long periods in freely behaving animals.

Results

We implanted 9 rats with hyperdrives containing up to 22 individually adjustable tetrodes, as described previously[34,36], targeting both prefrontal and parietal cortices (see Methods). Unless specified otherwise, these data were pooled together, as there were no systematic differences between them. Tetrodes usually recorded standard signatures of extracellular signal, including thin (<1 ms) extracellular spikes of negative polarity with ~100 μV amplitude (Fig. 3-1a), presumably of somatic origin[69]. However, in several instances (25 over 194 total tetrodes over 847 total recording days across 9 rats), the signal was dramatically altered to that resembling an intracellular dendritic recording (Fig. 3-1b). These signals manifested overnight while all tetrodes were stationary. Here the signal amplitude was orders of magnitude larger, containing broad (>5ms) positive polarity spikes with amplitudes of the order of thousands of microvolts (Fig. 3-1b, c). In fact, these signals could easily be mistaken for artifacts as their amplitude saturated the amplifiers set at high gains typically used in extracellular recording. Hence, we used data acquisition system settings with high dynamic range to record these large amplitude signals. All such measurements were obtained at a median of 18 (between 6 and 55) days after surgery and discontinuation of any psychoactive drug, ruling out any possible anesthesia effects.

DAP vs extracellular spikes

For reasons described below, we refer to these spikes as DAP. We computed several features of the 25 DAP sources measured *in vivo* from our data (Fig. 3-1d, see Methods), and compared

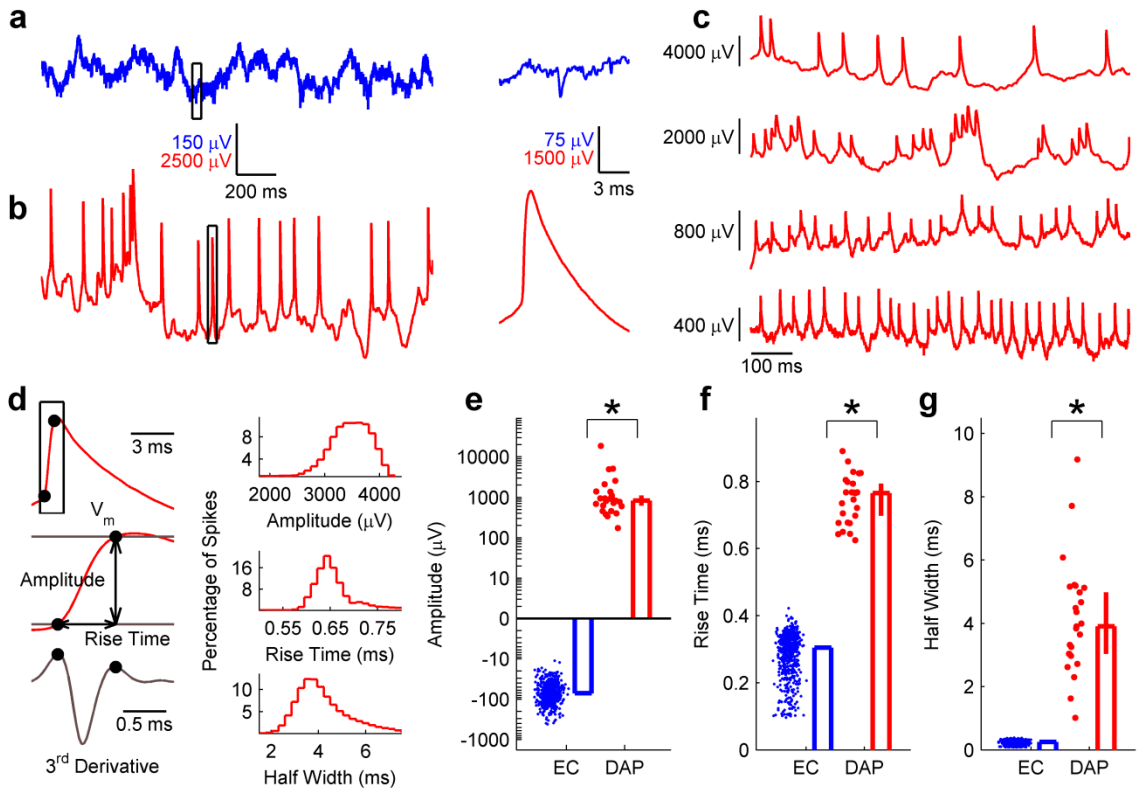

Figure 3-1 | Measurements of DAP in vivo.
a, Typical extracellular local field potential (LFP) showing ~100 μV fluctuations. Somatic action potentials are visible as thin, ~100 μV negative-polarity spikes (inset to right). **b,** Putative dendritic membrane potential recording on the same tetrode presented in **a** on the following day. Fluctuations are ~5000 μV. DAP are visible as broad, positive-polarity, ~5000 μV spikes with a much longer falling phase than rising phase (inset to right). **c,** Example membrane potential traces from four separate tetrodes, each exhibiting spontaneous dendritic spiking. **d,** Left, Quantification of DAP shape parameters (see Methods). Top right, distribution of DAP amplitudes within a single recording session, median 3420, [3410, 3430] μV, n=8187 spikes. Middle right, distribution of DAP rise times for the same recording session, median 0.65, [0.65, 0.65] ms, n=8187 spikes. Bottom right, distribution of DAP half widths for the same recording session, median 4.06, [4.02, 4.09] ms, n=8187 spikes. **e,** Extracellular spike amplitude (EC, blue) was always negative (−77.5, [−81.1, −73.4] μV, n=754 units), in comparison to DAP (red) which were always positive (833, [621, 1120] μV, n=25 dendrites), and more than 10 times larger in magnitude ($p=1.7\times10^{-17}$, Wilcoxon rank-sum test). **f,** The rise time of DAP (0.77, [0.70, 0.80] ms, n=25 dendrites) was significantly larger ($p=1.7\times10^{-17}$, Wilcoxon rank-sum test) than that of extracellular spikes (0.31, [0.31, 0.31] ms, n=754 units). **g,** The half-width of DAP (3.90, [3.04, 4.98] ms, n=25 dendrites) was also significantly larger ($p=1.7\times10^{-17}$, Wilcoxon rank-sum test) than that of extracellular spikes (0.26, [0.26, 0.26] ms, n=754 units). Throughout the figure, data are reported and presented as median and 95% confidence interval of the median, and * indicates significance at the $p<0.05$ level.

these to our extracellular somatic spike measurements from 754 units across 9 rats *in vivo* (Fig. 3-1e-g) and to available intracellular reports of dendritic spiking (Extended Data Table 3-1)[40,42,44–46]. First, similar to in-cell and quasi-intracellular measurements[60,61,65,66], DAP amplitude was always positive (Median 850 μV, range 175 to 20,000 μV) (Fig. 3-1d, e, Extended Data Fig. 3-1), in contrast to extracellularly recorded somatic spikes simultaneously recorded from nearby tetrodes; these were always of negative polarity and of much smaller amplitude (Median −70 μV, range −40 to −925 μV) (Fig. 3-1e, Extended Data Fig. 3-1). DAP rise time (0.77 ms) was fairly consistent across all recordings, similar to that of dendritic sodium spikes *in vitro*, and much larger than the rise time of the extracellular spikes (0.31 ms), but much shorter than the rising phase of calcium spikes (Fig. 3-1d, f, Extended Data Table 3-1)[40,42,46,58]. Also consistent with *in vitro* data, the full-width at half maximum (half-width) of DAP (3.90 ms) (Fig. 3-1d, g) was much longer than the DAP rise time (Extended Data Fig. 3-2a, b), and far greater than the half-width of extracellular (0.26 ms, Fig. 3-1g) or intracellular (~0.7ms, Extended Data Table 3-1) somatic spikes; DAP were also much wider than reported "high-amplitude positive spikes" from cortex[70] and somatic spikes recorded quasi-intracellularly[64–68]. However, DAP half-width was much shorter than the typical half-width of dendritic calcium spikes (Extended Data Table 3-1). Further, DAP width was more variable both within and across recordings (Extended Data Fig. 3-2), in contrast to very consistent DAP rise times across data, and there was no significant correlation ($r=0.24$, $p=0.26$) between DAP rise time and width across recordings (Extended Data Fig. 3-2f). These differences in the variability of rise time and width across DAP are also characteristic of dendritic sodium spikes (Extended Data Table 3-1)[40,42,44–46,50,53,58,59]. Hence, the above results are consistent with the hypothesis that our signals represent the intracellular dendritic membrane potential, and suggest that our spikes are sodium-based, not calcium-based.

These results raise several important questions: What mechanism allowed the intracellular-like measurement of DAP using tetrodes? Are the measurements stable over long periods and during locomotion? What type of cell do these DAP belong to? Are these locally generated DAP or back propagating action potentials? Are these signals recorded from proximal or distal dendrites? How prevalent are DAP during natural behavior and how are they modulated by internal and behavioral variables? Because these questions are impossible to unequivocally resolve in freely behaving animals using present techniques, we used signal analysis techniques to address them.

Mechanism of DMP recording, glial sheath hypothesis

We hypothesize that the DMP recordings were achieved by the above-mentioned in-cell (quasi-intracellular) recording[60,61,65,66] and glial-sheath mechanisms[62,63], where our tetrodes, ~40 µm in diameter with each uninsulated electrode ~13 µm in diameter, measured intracellular-like signals from dendrites only a few microns thick[38,46], and trapped in the ~4 µm gap between the electrode tips (Extended Data Fig. 3-3a, b). Specifically, increased resistance from the electrode tips to ground due to the proposed glial encapsulation of the electrode would allow recording of the intracellular membrane potential (Extended Data Fig. 3-3b). To validate this model we performed impedance spectroscopy measurements on electrodes during either DMP or the local field potential (LFP) recordings (Extended Data Fig. 3-3d). Fitting parameters to an electric circuit equivalent model of glial encapsulation[71,72], the only parameter that was significantly higher ($p=1.8x10^{-3}$) for DMP-recording electrodes was the resistance between the electrode tip and ground, through the glial sheath (Extended Data Fig. 3-3d, e). The estimated glial resistance was more than 6-fold larger for DMP-recording electrodes compared to LFP-recording; which is

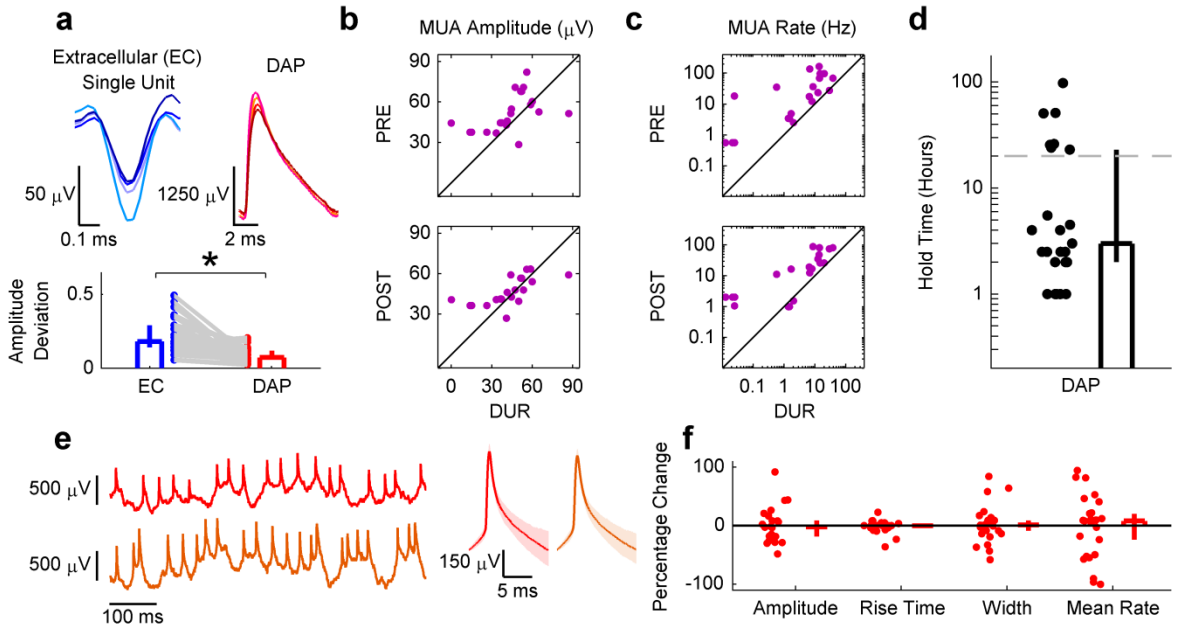

Figure 3-2 | DAP are similar across all electrodes of a tetrode and stable for long periods.
a, Top, the waveform of a single extracellular spike has very different amplitudes on each of the 4 tetrode channels (left), but the waveform of a single DAP on the same tetrode the following day has very similar amplitudes (right). Bottom, the spike amplitude variation across four electrodes (see Methods) was significantly greater for extracellular single units recorded the day before DAP were recorded (PRE) (0.18, [0.14, 0.29], n=25 units) compared to DAP during DMP recording (DUR) (0.09, [0.06, 0.12], n=25 DAP sources) on the same tetrode the following day ($p=6.2x10^{-6}$, Wilcoxon signed-rank test) **b,** Multi-unit activity (MUA) amplitude during DMP recording (DUR) (41.8, [36.9, 53.4] μV, n=25 recordings) was significantly lower than that during PRE (45.8, [44.3, 54.6] μV, n=25 recordings; $p=6.6x10^{-3}$, Wilcoxon rank-sum test). MUA amplitude was also smaller in DUR compared to that the day after DMP recording (POST, 44.1, [40.6, 53.9] μV, n=25 recordings), but not significantly so ($p=6.7x10^{-2}$, Wilcoxon rank-sum test). **c,** MUA rate was significantly lower in DUR (5.19, [1.29, 10.7], n=25 recordings) compared to both PRE (17.5, [4.84, 34.7] Hz, n=25 recordings; $p=2.1x10^{-5}$, Wilcoxon rank-sum test) and POST (16.5, [2.01, 25.5] Hz, n=25 recordings; $p=8.0x10^{-5}$, Wilcoxon rank-sum test). **d,** DAP recordings were stable for long periods of time (3, [2, 23] hours, n=25 recordings), with the shortest recording lasting 1 hour and the longest lasting 97.5 hours, or more than 4 days. Durations between 5.5 and 23 hours are absent due to restrictions on total recording duration in a single day, resulting in artificial bimodality. Hence, all recording durations are likely an underestimate of actual duration for which the DAP were held. **e,** Left, sample membrane potential at the beginning of recording (top), and 90 minutes afterwards (bottom) of recording, showing little change in the quality of recording. Right, averaged DAP (median and 25^{th}, 75^{th} percentile) in the first part of the recording to the left (n=616 DAP) was not qualitatively different from the averaged DAP in the later part of the recording (n=897 DAP). **f,** The percentage change from the first five minutes or recording to the last two minutes of recording was not significantly different from 0 for amplitude (−2.19, [−18.5, 9.17] % change, p=0.91, n=25 dendrites, Wilcoxon signed-rank test), rise time (0.00, [−3.57, 1.79] % change, p=0.52, n=25 dendrites, Wilcoxon signed-rank test), half-width (1.35, [−8.80, 8.87] % change, p=0.82, n=25 dendrites, Wilcoxon signed-rank test), nor mean firing rate (7.93, [−23.9, 20.5] % change, p=0.97, n=25 dendrites, Wilcoxon signed-rank test). Throughout the figure, data are reported and presented as median and 95% confidence interval of the median unless otherwise noted, and * indicates significance at the $p<0.05$ level.

precisely the condition predicted by the model that would yield glial-sheath assisted measurements of the intracellular voltage (Extended Data Fig. 3-3c).

The above result is corroborated by several properties of the signals on tetrodes that recorded DAP, evaluated before (PRE), during (DUR), and after (POST) the time in which the DMP signal was measured. First, DAP amplitudes were nearly identical on all four channels of a tetrode in DUR (see Methods), unlike in the PRE condition where the voltages of extracellular spikes were different across four channels (Fig. 3-2a). This would not occur if any single electrode of the tetrode had penetrated the dendrite, but would be expected if the dendrite and the entire tetrode tip were encapsulated during DMP recording. This would additionally result in the shielding off of the surrounding extracellular medium from the tetrode by the encapsulating glial sheath. Consistently, in the DUR condition both the amplitude and mean firing rate of detectable extracellular multi-unit activity (MUA) were significantly reduced (Fig. 3-2b, c, see Methods) compared to PRE. In a particular case where one of the four tetrode channels did not achieve an intracellular-like recording, MUA activity on only that channel was preserved, and its correlation with other channels remained low, suggesting that the single channel was not encapsulated by the glial sheath (Extended Data Fig. 3-4). There was also no evidence of damage to the tetrodes that yielded DMP measurements, as all MUA properties in POST were similar to those in PRE, including spike polarity, spike rate and spike amplitude with different amplitudes on the four channels (Fig. 3-2b, c).

DAP properties also remained stable for long periods of time (Fig. 3-2d-f). Our recordings typically lasted several hours, and DAP from the same tetrode could be recorded for up to 4 consecutive days (Fig. 3-2d, see Methods). From the beginning to the end of the recording span

of any single DMP, there was no systematic change in DAP amplitude, rise time, width, or mean firing rate (Fig. 3-2e, f). Together with the long recording duration, these observations indicate that the tetrode did not damage the dendrite during these measurements, a key advantage over other intracellular voltage measurement techniques, especially *in vivo*[56,57,73,74].

bAP vs DAP

While the rise times and widths of the spikes described above are consistent with dendritically generated sodium spikes, i.e. DAP, they are also consistent with somatically generated (bAP)[42,44–46,50–53]. To dissociate these two possibilities, we compared the firing properties of DAP to those of extracellular somatic spikes from well isolated units recorded simultaneously on nearby tetrodes (see Methods). We first examined data when the rats were quiescent, in slow wave sleep (SWS), to minimize the influence of behavioral parameters (Fig. 3-3, see Methods). DAP mean firing rates were high (6.4 Hz), 4-fold greater than the mean firing rates of extracellular units (1.6 Hz) (Fig. 3-3a, b). The high DAP firing rates were not due to multiple DAP sources being pooled together, as all DAP had inter-spike interval and amplitude distributions inconsistent with multiple independent sources (Extended Data Fig. 3-5, see Methods). The high rates were also unlikely due to damage or otherwise altered activity of dendrites because of the longevity of recording (Fig. 3-2d), and the absence of any systematic changes in DAP kinetics or rate (Fig. 3-2e, f) over long periods of time.

We further considered the possibility that the high DAP rates were a result of preferentially recording from interneurons, which typically have higher firing rates than pyramidal neurons[75]. This explanation would necessitate that DAP have other characteristics similar to interneurons'. For instance, interneurons exhibit very little spike amplitude attenuation within high frequency

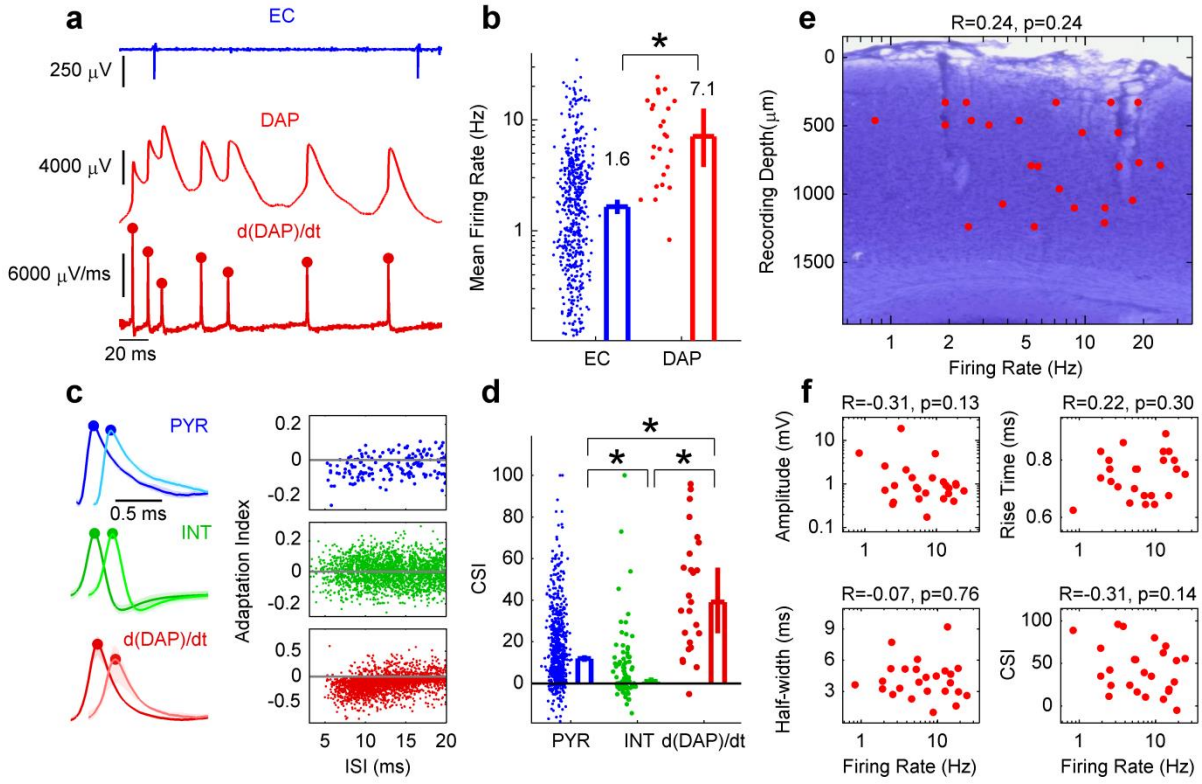

Figure 3-3 | DAP are likely to be from pyramidal neurons but have much greater firing rates and stronger short-term plasticity.

a, Top, sample LFP showing a single extracellular unit firing at a relatively low rate. Middle, sample putative membrane potential showing a DAP firing at a higher rate. Bottom, first temporal derivative of the MP trace. Dark red dots indicate the peak value of identified DAP and demonstrate activity-dependent attenuation. **b,** In SWS, the mean spontaneous firing rate of extracellularly recorded units (1.65, [1.41, 1.91] Hz, n=754 units) was more than 4-fold smaller ($p=4.1\times10^{-8}$, Wilcoxon rank-sum test) than the firing rate of DAP (7.07, [3.76, 12.6] Hz, n=25 dendrites). Notice the near complete absence of low (less than 1 Hz) firing rate DAP. **c,** Demonstration of CSI. Left, the median and 25th, 75th percentile of sample pyramidal neuron (blue, n=140 spike pairs) interneuron (green, n=6987 spike pairs) and d(DAP)/dt (red, 130 spike pairs) waveforms are plotted for the first spike in a burst (darker color) and the second spike in a burst (lighter color). For pyramidal neurons and DAP, the second spike has a smaller amplitude, but this is not the case for interneurons. Right, adaptation index (see Methods) plotted against inter-spike interval (ISI) for a sample pyramidal neuron, interneuron, and DAP. For pyramidal neurons and DAP, but not interneurons, the adaptation index tends toward negative values for ISI less than 20 ms. For clarity, every 5th spike pair is plotted for the interneuron and DAP. **d,** Pyramidal neuron CSI (12.0, [10.3, 13.5], n=657 units) was significantly greater ($p=1.0\times10^{-11}$, Wilcoxon rank-sum test) than that of interneurons (1.02, [0.25, 2.99], n=97units), but smaller ($p=7.1\times10^{-7}$, Wilcoxon rank-sum test) than that of DAP (39.1, [24.1, 55.6], n=25 dendrites). DAP CSI was significantly greater ($p=1.2\times10^{-9}$, Wilcoxon rank-sum test) than that of interneurons, indicating that DAP are unlikely to be recorded from interneurons. **e,** DAP mean firing rate was not significantly correlated with recording depth (770, [460, 960] μm, n=25 DAP sources; r=0.24, [−0.17, 0.58]; p=0.24, two-sided *t* test). The background shows a representative coronal slice of Nissl-stained posterior parietal cortex. Tetrode tracks are visible as dark bands descending from the top of

the slice. **f,** DAP mean firing rate was not significantly correlated with amplitude (r=−0.31, [−0.63, 0.10], p=0.13, two-sided *t* test), rise time (r=0.22, [−0.19, 0.56], p=0.30, two-sided *t* test), half-width (r=−0.07, [−0.45, 0.34], p=0.76, two-sided *t* test), or CSI (r=−0.31, [−0.63, 0.10], p=0.14, two-sided *t* test), suggesting that high rate DAP are not from a special population of neurons separate from those with low rate DAP and that the recording configuration did not systematically alter local membrane properties (membrane capacitance or resistance) which would artificially increase firing rates. Throughout the figure, data are reported and presented as median and 95% confidence interval of the median unless otherwise noted, and * indicates significance at the p<0.05 level.

bursts, characterized by the complex spike index (CSI)[75,76] (see Methods), in contrast to pyramidal neurons, which exhibit consistent amplitude attenuation. This distinction between cell types is present in dendrites as well, as *in vitro* reports show that DAP exhibit more amplitude attenuation with repeated firing compared to somatic spikes in pyramidal neurons[46,51,52] but do not show much attenuation in interneurons[77,78]. Thus, DAP should have a high CSI if recorded from pyramidal neurons and a low CSI if recorded from interneurons. Further, the same sodium channel inactivation kinetics that result in CSI differences between pyramidal neurons and interneurons would likely also influence peak firing rates[76], with reduced peak rates for pyramidal neurons and pyramidal DAP compared to the interneurons'.

To test these predictions, we separated the extracellular units into putative pyramidal neurons and interneurons (Extended Data Fig. 3-6a)[75] and compared their CSI with that of the first temporal derivative of DAP, as the rising phase of the extracellular spike closely corresponds to the rising phase of the first temporal derivative of the intracellular spike[69]. Consistent with previous studies[75,79], our data set contained far more pyramidal neurons (86%) than interneurons (14%), the pyramidal neurons' firing rates were lower than interneurons'[75] (Extended Data Fig. 3-6b), and the CSI of pyramidal neurons was greater than that of interneurons (Fig. 3-3c,d)[75,76]. DAP mean rate was significantly greater (more than five-fold) than that of pyramidal neurons ($p=2.4x10^{-9}$), but not interneurons (p=0.16) (Extended Data Fig. 3-6b). However, the peak firing

rates of DAP (92.6 Hz) were lower than those of interneurons (122 Hz, $p=2.1x10^{-2}$) but greater than those of pyramidal neurons (67.6 Hz; $p=1.8x10^{-2}$) (Extended Data Fig. 3-6c). The differential pattern of the mean and peak rates could be explained by differences in short term plasticity. Indeed, the CSI of DAP was far greater than that of CSI of interneurons ($p=1.1x10^{-9}$), and also greater than that of pyramidal neurons ($p=8.3x10^{-6}$) (Fig. 3-3c, d), supportive of the hypothesis that our recordings are predominantly from pyramidal dendrites. Other measures of short term plasticity, such as DAP amplitude and width, showed activity-dependent adaptation as well, similar to that of pyramidal neuron dendrites *in vitro*[51,52] (Extended Data Fig. 3-6d, e).

The high mean firing rate of DAP compared to pyramidal neuron somatic spike rates further implies that the majority of these measurements are not of bAP but are of locally generated DAP in dendrites that are electrotonically distant from the soma. These high DAP rates are unlikely to arise from measurement artifact or from specialized subpopulation of high-rate pyramidal neurons because the DAP rates were similar at all depths (from 330 µm to 1240µm, p=0.26, Fig. 3-3e). Other properties of DAP sources were uncorrelated with DAP rate as well, including amplitude (p=0.15), rise time (p=0.29) half-width (p=0.96), and CSI (p=0.09) (Fig. 3-3f). Hence, the disparate rates of DAP and somatic spikes suggests that only a fraction of DAP elicit somatic spiking, indicating a significant decoupling of dendrites and somata[39,43,44,46,52].

Subthreshold dendritic potential dynamics during SWS

We also quantified the subthreshold fluctuations accompanying DAP during SWS, which had characteristics suggesting they represent the DMP (Fig. 3-4a, see Methods). Like DAP amplitude, the subthreshold fluctuations were of the order of thousands of microvolts, reaching up to 20 mV, (Fig. 3-4a, b), far exceeding the range of the LFP recorded simultaneously on

nearby tetrodes (Fig. 3-4b).The magnitude of the subthreshold fluctuation was positively correlated with the DAP amplitude on the same recording (Fig. 3-4c); in contrast, nearby LFP magnitude was not correlated with DAP amplitude (Extended Data Fig. 3-7a). This suggests the subthreshold fluctuations originated from the same source as the DAP, and implicates a common cause of amplitude differences across different recordings, which we hypothesize to be the quality of glial-sealed encapsulation (Extended Data Fig. 3-3, 3-4). The subthreshold magnitude was also always greater (5.5-fold) than the corresponding DAP amplitude (Fig. 3-4c), a membrane property primarily observed *in vitro* in dendrites that are electrotonically distant from the soma[40–46]. Furthermore, in all but one case the DMP signal in SWS was significantly negatively correlated with the LFP signal simultaneously recorded on a nearby tetrode (Fig 3-4d, Extended Data Fig. 3-7b), similar to the anticorrelation observed between the somatic membrane and LFP[80]. This demonstrates that the direction of current flow was opposite between extracellular tetrodes and those recording DMP, another signature of recording intracellular membrane voltage.

We next tested if the subthreshold DMP influenced DAP dynamics[81] by quantifying the relationship between the instantaneous subthreshold DMP magnitude and DAP rate (see Methods). The range of subthreshold DMP at which DAP initiated was quite large, 4.6-fold larger than the magnitude of the corresponding DAP, and positively correlated with DAP amplitude (Fig. 3-4e). The large DAP initiation range, in some cases reaching up to 10 mV (Fig. 3-4e), is similar to that reported for dendrites *in vitro*[40–46], further supportive of the dendritic origin of our measurements.

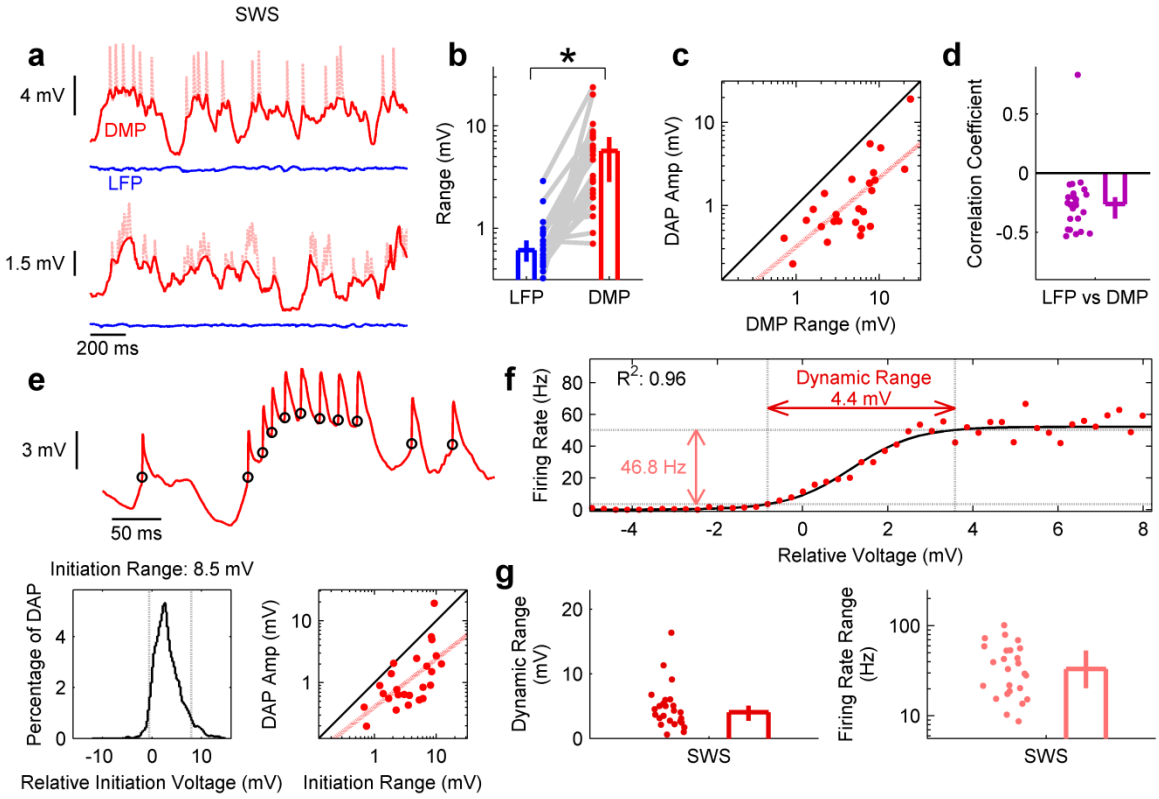

Figure 3-4 | Large subthreshold membrane potential fluctuations modulate DAP rates during SWS. **a,** Top, sample dendritic membrane potential (DMP, red) trace during SWS, showing prominent oscillations of the same order of magnitude as DAP. DAP are shown in light red to highlight the spike-clipped subthreshold membrane potential, which has a range of 6.5 mV. Shown below on the same scale is the local field potential (LFP, blue) recorded simultaneously on a nearby tetrode, showing much smaller fluctuations. Bottom, same as above but from a different pair of tetrodes in a different recording session, again showing prominent fluctuations as large as DAP, but at a reduced scale. **b,** The range of the LFP (0.61, [0.47, 0.76] mV, n=25 LFP) was nearly an order of magnitude (9.3-fold) smaller ($p=1.8x10^{-8}$, Wilcoxon signed-rank test) than the subthreshold DMP accompanying DAP (5.69, [2.85, 7.77] mV, n=25 dendrites). * indicates significance at the $p<0.05$ level. **c,** In SWS, the range of subthreshold DMP was always larger ($p=1.2x10^{-5}$, Wilcoxon signed-rank test) than the corresponding DAP amplitude (0.84, [0.63, 1.86] mV, n=25 dendrites), and positively correlated (r=0.73, [0.47, 0.87]; $p=3.7x10^{-5}$, two-sided *t* test). **d,** In all but one case, LFP and simultaneously recorded DMP during SWS were negatively correlated (r=-0.26, [−0.38, -0.20]), further indicating the DMP is a measure of the intracellular membrane potential. **e,** Top, sample DMP trace segment showing a dynamic threshold for DAP initiation, with the initiation points marked by black circles. Bottom left, histogram of initiation voltages for entire recording session from which the above was taken; the 5-95% range of initiation voltages spans 8.5 mV. Bottom right, DAP initiation range (3.67, [2.24, 6.99] mV, n=25 dendrites) was larger ($p=3.6x10^{-5}$, Wilcoxon signed-rank test) than the corresponding DAP amplitude, and positively correlated (r=0.64, [0.33, 0.83], n=25 dendrites; $p=5.6x10^{-4}$, two-sided *t* test). **f,** Sample DAP firing rate as a function of relative voltage, which was well-approximated (Extended Data Fig. 3-7g) by a sigmoidal logistic function (black line). Firing rates here vary by 47.2 Hz over a dynamic range of 4.4 mV. **g,** Left, the population of DAP had a large dynamic range of initiation voltages (4.03, [2.74, 5.07] mV, n=25 dendrites), as defined in **g**. Right, the firing rate range of the DAP population was similarly wide (33.1, [20.3, 53.1] Hz, n=25

dendrites). Throughout the figure, data are reported and presented as median and 95% confidence interval of the median.

Accompanying this variable initiation threshold was a strong modulation of DAP rates by subthreshold DMP. During SWS, DAP rate had a slowly increasing, sigmoidal dependence on subthreshold DMP (Fig. 3-4f), with rate increasing over a large dynamic voltage range (see Methods) which often exceeded the magnitude of DAP themselves (Fig. 3-4f, g, Extended Data Fig. 3-7c). The firing rate was modulated from nearly 0 Hz at low values of the membrane voltage up to 300 Hz at the highest membrane voltages (Fig. 3-4f, g, Extended Data Fig. 3-7c). Because short-term ion channel dynamics could influence spike initiation properties[81], the above calculations were also done for only those DAP separated from all others by at least 50ms (termed solitary DAP), with only minor differences (Extended Data Fig. 3-7d-h). These results suggest a form of analog-digital coding in the dendrites, in which the analog subthreshold DMP modulates the firing rate of digital suprathreshold DAP in a gradual fashion resulting in a high dynamic range of firing.

Dendritic sub- and supra-threshold membrane potential during unrestrained behavior

Do DAP occur during drug-free natural behavior and if so, how frequently? The stable nature of our recordings further allowed us to measure dendritic activity and its subthreshold modulation during wakefulness, when the rat was free to explore the recording chamber (RUN) (Fig. 3-5a, see Methods). Remarkably, DAP mean rate during RUN (12.8 Hz) was nearly twice as large compared to the mean rate during SWS (6.87 Hz, Fig. 3-5b), possibly due to increased excitatory drive from sensory inputs. Consistent with the observed activity-dependent adaptation (Fig. 3-3d,

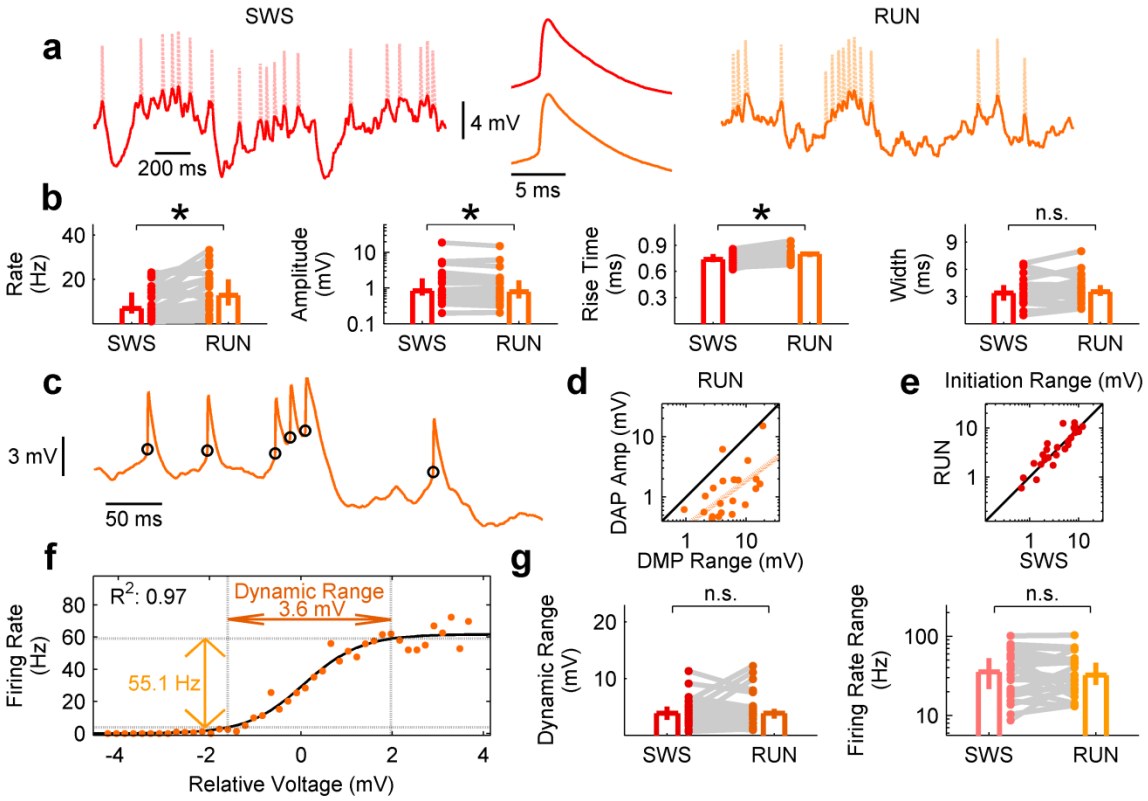

Figure 3-5 | Large subthreshold membrane potential fluctuations modulate DAP rates during RUN. **a,** Sample membrane potentials during SWS (red, left) and exploration (RUN, orange, right) show similar dynamics and amplitude of both DMP and DAP (middle). **b,** DAP mean firing rate was nearly twice as large($p=1.9x10^{-3}$, Wilcoxon signed-rank test) during RUN (12.8, [8.29, 20.0] Hz, n=25 dendrites) than during SWS segments of comparable duration (6.87, [4.66, 14.2] Hz, n=25 dendrites); DAP amplitude in RUN (0.79, [0.52, 1.66] mV, n=25 dendrites) was reduced ($p=3.8x10^{-3}$, Wilcoxon signed-rank test) compared to during SWS (0.79, [0.52, 1.66] mV, n=25 dendrites); DAP rise time in RUN (0.80, [0.77, 0.80] ms, n=25 dendrites) was slightly greater ($p=2.5x10^{-4}$, Wilcoxon signed-rank test) than rise time in SWS (0.74, [0.71, 0.80] ms, n=25 dendrites); DAP width during RUN (3.50, [3.10, 4.27] ms, n=25 dendrites) was slightly but not significantly larger (p=0.28, Wilcoxon signed-rank test) than width during SWS (3.38, [2.58, 4.25] ms, n=25 dendrites). **c,** Sample DMP trace during RUN shows a dynamic initiation range similar to that observed in SWS (Fig. 3-4e). **d,** DMP range during RUN (3.92, [2.82, 6.24] mV, n=25 dendrites) was significantly larger ($p=1.8x10^{-5}$, Wilcoxon signed-rank test) than the corresponding DAP amplitude (0.79, [0.52, 1.66] mV, n=25 dendrites), and significantly correlated (r=0.66, [0.36, 0.84], n=25 dendrites, $p=3.1x10^{-4}$,two-sided *t* test). **e,** DAP initiation ranges in SWS (3.67, [2.24, 6.99] mV, n=25 dendrites) and RUN (4.07, [2.51, 8.14] mV, n=25 dendrites) were positively correlated (r=0.91, [0.80, 0.96], n=25 dendrites, $p=3.4x10^{-10}$, two-sided *t* test) and not significantly different (p=0.46, Wilcoxon signed-rank test). **f,** Sample V-R curve during RUN, which was well-described (Extended Data Fig. 3-9) by a sigmoidal logistic function, as in SWS. **g,** 24 of 25 dendrites had sufficient data to compare V-R curves in SWS and RUN. Left, the dynamic voltage range during RUN (3.90, [2.98, 4.67] mV n=24 dendrites), was not significantly different (p=0.73, Wilcoxon signed-rank test) from the dynamic range in SWS (3.87, [2.74, 5.03] mV, n=24 dendrites). Right, the firing rate range in RUN (32.5, [24.6, 46.5] Hz (n=24 dendrites) was not significantly different (p=0.86, Wilcoxon signed-rank test) from the range during SWS (35.6, [21.6, 53.1] mV, n=24 dendrites). Throughout the figure,

data are reported and presented as median and 95% confidence interval of the median. * and n.s. indicates significance or lack of significance, respectively, at the $p<0.05$ level.

Extended Data Fig. 3-6d, e), DAP amplitude was smaller during RUN compared to SWS, and rise time and width were slightly longer, though the difference in width was not statistically significant (Fig. 3-5a, b). The similarity of these measures to those in SWS demonstrates the stability of the recordings even during behavior, as rats were not head-restrained or recently anesthetized during exploration.

Surprisingly, subthreshold DMP measures were also comparable in SWS and RUN. First, the magnitude of subthreshold DMP was equally large in the two conditions (Fig. 3-5a, Extended Data Fig. 3-8). This is in contrast to the pattern observed in the LFP, where fluctuations are severely diminished during exploration compared to the large fluctuations present in SWS (Extended Data Fig. 3-8)[82,83]. The subthreshold DMP magnitude during exploration was 6.3-fold larger than the corresponding DAP amplitude, and the two were highly correlated (Fig. 3-5d), as in SWS. Second, DAP had a large initiation range in RUN (Fig. 3-5e) that was 5.8-fold larger than the corresponding DAP amplitude, as in SWS (Extended Data Fig. 3-9a). DAP rate during RUN was also modulated by subthreshold DMP in a sigmoidal fashion (Fig. 3-5f, g, Extended Data Fig. 3-9b) over a wide dynamic voltage range, and spanned a large range of firing rates, both of which were as large as in SWS (Fig. 3-5f, g). As in SWS, these results were similar when performed on solitary DAP during exploration (Extended Data Fig. 3-9c-h). These results demonstrate that the high dynamic range of analog subthreshold DMP and digital supra-threshold spiking are present during both free behavior and SWS, supporting a hybrid analog-digital coding scheme under both conditions.

Modulation of DAP, DMP, and soma by behavior

In addition to sleep-run differences, do DAP and DMP contain information about instantaneous behavior? Previous studies have shown that somatic spike rates in the posterior parietal cortex (PPC) are modulated by specific types of movements, including forward running, left turns, and right turns (Fig. 3-6a)[19,84], and have an anticipatory component to their response[84]. Hence, we compared the modulation of parietal DAP, DMP, and somatic spike rates by the rats' movements in an egocentric reference frame during free locomotion in both a rest box and in a random foraging task (Fig. 3-6b, Extended Data Fig. 3-10a, see Methods). To quantify modulation by behavior, we computed the normalized dispersion of egocentric response maps (see Methods)[84]. The anticipatory component was quantified by finding the time lag corresponding to the highest depth of modulation (Extended Data Fig. 3-10b, see Methods).

These analyses revealed substantially different properties of tuning in pyramidal somata (PYR), DAP, and DMP (Fig. 3-6c). Normalized dispersion for PYR (0.26) was significantly better than that of DAP (0.32, $p=2.7\text{x}10^{-2}$, Wilcoxon rank-sum test) and DMP (0.33, $p=1.4\text{x}10^{-2}$, Wilcoxon rank-sum test), which were not significantly ($p=0.52$, Wilcoxon rank-sum test) different from each other. Interestingly, the depth of modulation of egocentric maps was comparable between all three groups (Extended Data Fig. 3-10c), with a similar percentage having a depth of modulation significantly above chance (PYR, 156/245 (64, [57, 7$\bar{0}$] %), DAP, 13/24 (54, [33, 74] %), DMP, 9/15 (6$\bar{0}$, [32, 84] %)). Coherence[85] showed a different pattern, with DMP having the highest coherence (Extended Data Fig. 3-10d), but because coherence is computed on unsmoothed rate maps, and the continuous DMP signal has more data, this is likely an artifact. Similar to dispersion, short-term stability for PYR was larger than DAP and DMP, but the differences were not statistically significant (Extended Data Fig. 3-10e). These results

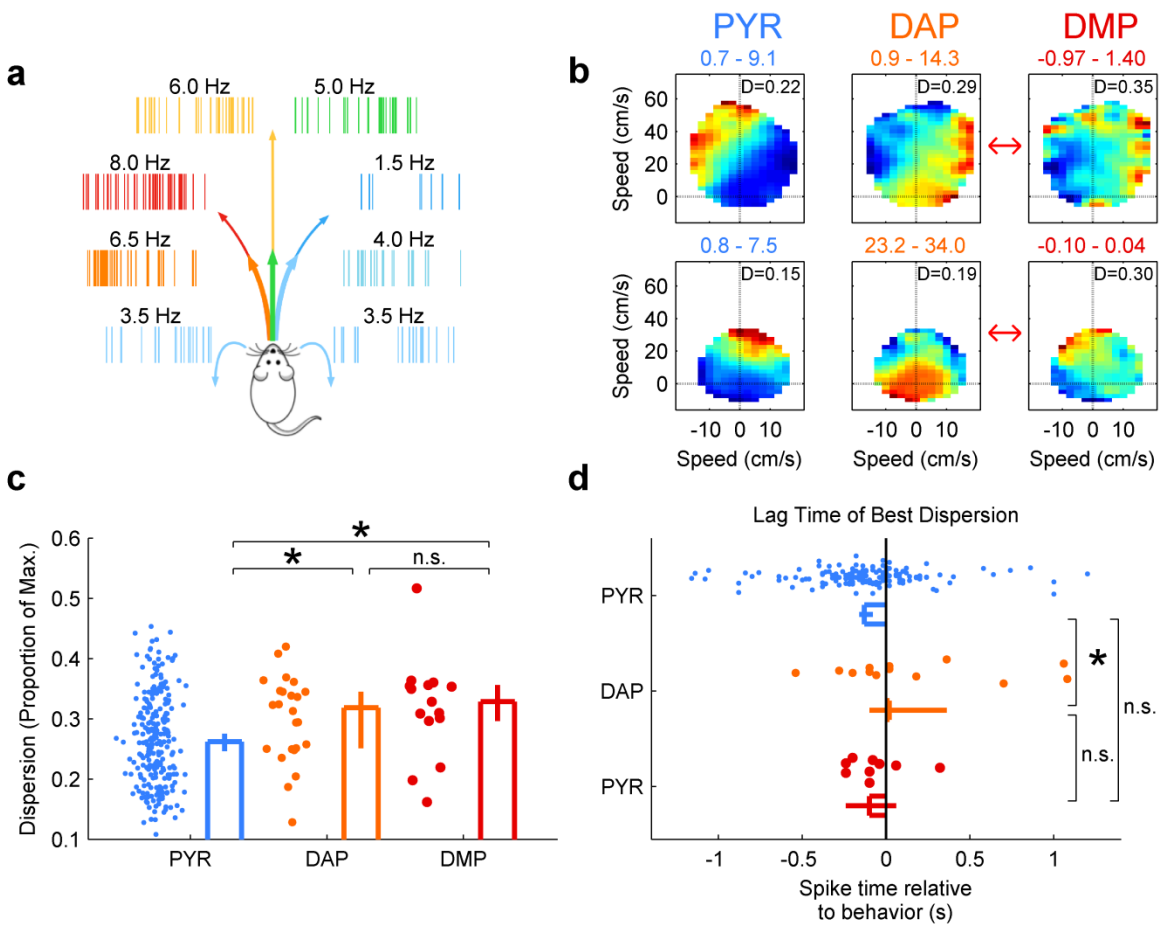

Figure 3-6 | DAP show non-anticipatory egocentric responses.
a, Schematic of egocentric map computation. In this example, the neuron fires maximally (8 Hz, red) during a left hand turn at high velocity, and minimally (1.5 Hz, blue) during a right hand turn at high velocity. **b,** Two sample pyramidal (PYR, left), DAP (middle), and DMP (right) egocentric rate maps. The minimum and maximum firing rates (mean voltages for DMP) for each map are displayed in the title, and the normalized dispersion D (see Methods, Extended Data Fig. 3-10a, b) is displayed in the upper-right corner. Red arrows indicate DAP and DMP from the same recording sessions. **c,** The normalized dispersion of pyramidal somata (0.26, [0.25, 0.28] , n=245 maps) was significantly smaller than that of DAP (0.32, [0.25, 0.34], n=24 maps, $p=2.7x10^{-2}$, Wilcoxon rank-sum test) and DMP (0.33, [0.30, 0.36], n=15 maps, $p=1.4x10^{-2}$, Wilcoxon rank-sum test), indicating better tuning for PYR. DAP and DMP dispersions were not significantly different from each other (p=0.52, Wilcoxon rank-sum test). **d,** The time lag corresponding to the optimal tuning for pyramidal somata with significant tuning (−130 [−160, −80] ms, n=156 maps with significant tuning) was significantly different from 0 ($p=7.8x10^{-8}$, Wilcoxon signed-rank test), indicating significant predictive coding. The same measure for DAP (20, [−100, 360] ms, n=13 maps with significant tuning) was not different from 0 (p=0.58, Wilcoxon signed-rank test) and significantly more positive than PYR ($p=4.4x10^{-2}$, Wilcoxon rank-sum test). DMP (-100, [-240, 60] ms, n=9 maps with significant tuning) was also not significantly different from 0 (p=0.19; Wilcoxon signed-rank test), but not significantly different from either PYR (p=0.62, Wilcoxon rank-sum test) or DAP (p=0.3, Wilcoxon rank-sum test). Throughout the figure, data are reported and presented as median and 95% confidence interval of the median. * indicates significance at the p<0.05 level, and n.s. indicates lack of significance at the p<0.05 level.

demonstrate that there is significant depth of modulation in both somata and dendrites, but the tuning is strengthened at the soma through a reduction in dispersion, leading to a single "clustered" region of the egocentric space with increased firing rate.

Consistent with a previous study[84], the time lag corresponding to the optimal ΔS/S for pyramidal neurons with significant tuning was significantly negative (−130 ms, $p=7.8x10^{-8}$) (Fig. 3-6d), indicating a preference to code for movements to be made in the future. In some instances, somatic spikes were best tuned for behavior several seconds in the future or past (Extended Data Fig. 3-10f). In contrast, the optimal lag time for significantly tuned DAP (20 ms) was not significantly different from 0 ($p=0.58$) and significantly more positive than PYR lag ($p=4.4x10^{-2}$). DMP lag (-100 ms) was also not significantly different from 0 ($p=0.19$), but not significantly different from either PYR ($p=0.62$) or DAP ($p=0.3$). This indicates that in addition to an improvement in coding quality, egocentric responses also become more anticipatory in the soma compared to the dendrite[17,24,86–88].

We then investigated the plasticity of egocentric responses. First, we computed the correlation between the maps computed from data in the first and second halves of a session[36]. These correlations for pyramidal somatic spikes (0.33) were greater than that for DAP (0.21, $p=3.8x10^{-2}$) but not DMP (0.27, $p=0.38$) (Extended Data Fig. 3-10g). The plasticity of the anticipatory component of neural responses was evaluated by computing the difference in optimal lag times between the first and second halves (see Methods). There were small but non-significant shifts for PYR (-40 ms, $p=0.88$), DAP (-40 ms, $p=0.75$), and DMP (+140 ms, $p=0.48$) (Extended Data Fig. 3-10h).

Hence, pyramidal neuron somata and dendrites both code for egocentric movement, but with important differences that illustrate potential computational principles within a neuron. First, pyramidal somatic responses are less diffuse than DAP and DMP responses, even though equivalent percentages of PYR, DAP, and DMP are significantly tuned. Second, the optimal coding occurs at negative time lags, or prospectively, for pyramidal somatic spikes but not for DAP or DMP. These results could be explained by a multi-stage model of information processing within individual PPC neurons, where dendrites integrate initial inputs into diffuse, high firing rate responses representing the current behavioral state of the animal, which are integrated again at the soma into concentrated, low firing rate responses with an added anticipatory component. An alternate possibility is that the anticipatory responses in the soma arise from other, more proximal dendritic branches, which we may not be measuring.

Conclusions

This is the first time that the membrane potential and sodium spikes of putative neocortical distal dendrites have been directly recorded during natural behavior, long removed from anesthesia or any drugs. Further, these measurements were done at sub-millisecond temporal resolution and were remarkably stable for at least one hour and up to four days, which is unprecedented compared to patch clamp techniques, even *in vitro*[41,42,53,55–59,73,74]. DAP kinetics were similar to those seen *in vitro* and in anesthetized animals[40–46]. Analysis of these recordings revealed a number of surprising results. First, DAP fired at very high rates *in vivo*, far greater than somatic rates. Additionally, DAP were accompanied by large subthreshold DMP fluctuations, the magnitudes of which were always larger than the DAP amplitude; this was present not only during SWS but also during active exploration. Further, DAP rates varied by an order of

magnitude as a function of the subthreshold DMP in a graded fashion during both SWS and active exploration, suggesting a large dynamic range. Finally, unlike previous reports from primary sensory-motor neocortical areas showing dendritic responses similar to those at the soma[58,59], our measurements from PPC showed substantial differences between DAP, DMP and somatic spikes in both quality and temporal dynamics.

Discussion

DAP have long been hypothesized to endow neurons with greater computational power by turning dendritic branches into computational subunits with branch-specific plasticity[21–25]. In support of this, dendrites have been shown to support initiation and propagation of action potentials *in vitro* via voltage-gated sodium, potassium, and calcium channels[40–46] which are critical for the induction of some forms of long-term plasticity[49]. What has been unclear is if the conditions for generating DAP exist *in vivo* during natural behavior. Recent experiments with patch-clamp recordings in head fixed mice suggest that proximal dendrites in visual cortex support spikes, though a majority of them were back propagating action potentials while some were DAP[59]. In contrast, we present recordings that are putatively from electrotonically distal dendrites which generate dendritic spikes locally, and where somatically generated bAP are mostly absent[39,43,44,46,52]. Importantly, these recordings were stable for hours or days at a time during free locomotion with no obvious damage to the dendrite.

How is it possible to record intracellular dendritic voltages using an extracellular tetrode, a bundle of 4 electrodes each 12µm in diameter and separated by about 4µm? We hypothesize that our tetrodes are in a "glial-assisted" configuration similar to in-cell or quasi-intracellular recordings[60,61,65,66]. Because we did not apply any suction as done with patch-clamp

recordings[55,56], in this model the requisite high seal resistance would come from glial encapsulation[62,63] trapping a segment of a thin dendrite between the four electrode tips and the glial cells, forming a stable configuration providing high quality, positive polarity sub- and supra-threshold signals. Our *in-vivo* impedance spectroscopy measurements are in strong support of such a model, and the negative correlation between the subthreshold DMP and LFP is consistent with a measure of intracellular voltage. The engulfment process might be facilitated by the fine-scale geometry of our gold-plated tetrode tips, but this is not sufficient to guarantee dendritic recordings since the tetrodes have to be positioned close enough to a neuron to trap the dendrite without puncturing it. Indeed, our current success rate of dendritic recordings is quite low (25 DAP over 194 total tetrodes across 9 rats, 13%; obtained over 847 total recording days), but comparable to the success rate of somatic whole cell recordings during natural behavior[74,89,90]. Further refinements of the technique are needed to make these recordings more frequent.

While chronic, *in-vivo* measurements with tetrodes currently precludes direct identification of the neural processes we record from, several signal properties are consistent with the hypothesis that our measurements are from electrotonically distal dendrites of pyramidal neurons and the dendritic spikes are generated locally in the dendrites, not back-propagated from the soma. First, the high dynamic range of the subthreshold DMP, reaching up to 30mV and dwarfing the spike amplitude, is similar to *in vitro* dendritic recordings and unlike somatic recordings. DAP also have a very fast rise time, consistent across different recordings, but a much longer and more variable decay time, again quite similar to DAP properties *in vitro*[40,44–46] and *in vivo* in anesthetized or head fixed animals[41,58,59]. The strong activity-dependent attenuation of DAP indicates that they belong to pyramidal neurons rather than interneurons[75,76]. Finally, another

striking feature of DAP is their high rates, which are unlikely to come from damage to the neuron due to stable DAP properties over hours. The fact that these rates greatly exceed those of pyramidal units in the same brain region implies that a large amount of activity and information processing in a neuron may be occurring in the dendrites without being read out in the soma, consistent with *in vitro* studies showing decoupling of somatic and dendritic compartments[39,43,44,46,49,52]. Further, if dendrites are operating semi-independently, and not globally governed by bAP from the soma, then NMDA-dependent plasticity could be induced in only a specific dendritic branch, allowing for more input-specific plasticity and clustering of synapses with similar information[21–25,49].

We also see a strong, graded modulation of DAP firing rate by subthreshold DMP. This endows the dendrites with a rate code defined by the depolarization level of the dendrite, and one reminiscent of the sigmoidal response profile of the hidden layer of artificial neural networks[22,23]. This large subthreshold modulation range (~5mV average, ~20mV max) is consistent with but greater than the recent results from the somata of hippocampal CA1 neurons' activity within place fields[73,74,90], entorhinal stellate cells' activity within grid fields[91], and barrel cortex neurons during social interaction[88]. The true subthreshold voltage range in our case is likely even greater, as the magnitude of signals obtained through our measurement technique would be influenced by the quality of the glial seal.

Consistent with previous studies, somatic spikes in PPC were modulated by movement in an egocentric reference frame[19] in an anticipatory fashion during free behavior[84]. We further found that DAP and DMP also exhibit egocentric modulation, but are more disperse and do not show significant anticipatory behavior. The anticipatory nature of somatic, but not dendritic activity, is

reminiscent of similar results in feed-forward networks[17,24] which rely on spike-timing dependent plasticity between many inputs and a single output; analogous mechanisms may be at work between DAP from many branches and somatic spiking within a single neuron. Similar anticipatory shifts are seen in many neural circuits, including hippocampal place fields[17], predictive responses in visual areas[86,87], and anticipatory membrane potential dynamics in barrel cortex[88]. Our findings suggest a computational framework in which individual cortical neurons take information about the current state of the world, present in the dendrites, and form an anticipatory, predictive response at the soma, a computation similar to that performed by a Kalman Filter[92] or Hidden Markov Model[93]. Thus, unlike network models of sequence learning, each individual neuron may behave like a feed-forward circuit that performs predictive coding based on non-predictive inputs arriving from many dendritic branches[17,24]. Further, the intermediate integration step performed by the dendrites is likely a crucial one in neurons with extensive dendritic trees, to allow inputs at distal tufts to be integrated in the somatic response[43].

Our results paint a bold new picture of dendritic activity in the awake, unanesthetized animal. Dendrites are not just passively ferrying subthreshold EPSPs to the soma, but are very active, initiating DAP at rates far exceeding somatic firing rates. High DAP rates can greatly enhance dendritic branch specific plasticity and computation, largely independent of somatic spiking, thereby enhancing network capacity. These results demonstrate that dendritic signaling *in vivo* is indeed varied and colorful[21], and offers a unique view into the computations performed within a single neuron.

Methods

Recording Procedure

Subjects: Data were obtained from 9 singly housed adult male Long-Evans rats (350-425g at the time of surgery). Animals were trained to perform spatial exploration tasks non-central to the present study and described previously[34,36]. The animals were water restricted (minimum of 30mL/day) in order to increase motivation to perform tasks, and received sugar water or solid cereal rewards during spatial exploration tasks. Further, they were food restricted (minimum of 15g/day) to maintain a stable body-weight and increase motivation to perform in the random foraging task (see below). All experimental procedures were approved by the UCLA Chancellor's Animal Research Committee and in accordance with NIH-approved protocols.

Surgery and in vivo electrophysiology: All methods were analogous to procedures described previously[34,36]. Rats with satisfactory behavioral performance on spatial exploration tasks were anesthetized using isoflurane and implanted with custom-made hyperdrives with 22 independently adjustable tetrodes. All implanted tetrodes were constructed in-house from 13 µm-diameter NiChrome wire coated with 2 µm-thick polyimide insulation, according to previously-reported techniques[34,36]. After the tetrodes were cut, the tips were electroplated with a gold particle solution containing 75% gold plating solution and 25% multi-walled carbon nanotube solution. A current of 1 µA was passed for 2 seconds with the electrode tip as the anode. This was repeated until the impedance at 1 kHz decreased below 250 kΩ for each electrode of every tetrode. Additional checks ensured that the four channels of a tetrode were not shorted.

Four rats were implanted with drives targeting right prefrontal cortex and right posterior parietal cortex. Four additional rats were implanted with drives targeting both left and right parietal

cortex. After recovery from surgery, all tetrodes were slowly lowered through cortex over a span of several days to months. Subsets of tetrodes were advanced daily, typically ~70µm and rarely more than 140µm in one day. Before tetrodes were adjusted each day, all continuous signals were visually and aurally screened for intracellular-like signatures, consisting of large-amplitude fluctuations and broad, large amplitude spikes of reverse polarity compared to normal extracellular units. While a tetrode recorded a dendritic signal, no other tetrodes in the same hemisphere were adjusted. DAP signals always manifested overnight while all tetrodes were stationary.

Signals were recorded using a Neuralynx data acquisition system at a sampling rate of 32 kHz from 7 rats and 40 kHz from 1 rat; all signals were initially digitally filtered through a 32 tap low-pass FIR filter with a cutoff frequency of 9000 Hz and a high-pass DC offset filter with a cutoff frequency of 0.1 Hz. Data from both brain regions and both hemispheres were pooled together for Figures 3-1 through 3-5 and Extended Data Figures 3-1, 3-2 and 3-4 through 3-9, as no systematic differences existed between any of these regions. Data from both parietal hemispheres from one rat performing the random foraging task (see below) were pooled together for Figure 3-6 and Extended Data Figure 3-10.

Behavior

Position tracking: For 5 rats, the animal's position was measured using an overhead camera that detected the position of colored LEDs (0.5 cm x 0.5 cm each) placed on top of the electrode assembly on the head, and sampled at an average of 55 Hz at a resolution of 640x480 pixels. This data was used to compute instantaneous position, running speed and movement direction.

Rest box: The majority of data were recorded when rats were left to freely behave in a "rest box" made of plastic with an open top (60x40 cm, 103 cm high). A small cloth was placed in the box for rats to rest on, but no other salient cues were present on any surface of the box, and the box was cleaned between recording sessions to eliminate odors. During recording, rats were totally unrestrained and free to groom, sleep, and move around; hence we refer to behavior in this condition and random foraging (see below) as "free locomotion". This configuration allowed us to characterize the properties of the same DMP during SWS and RUN. Recording sessions lasted approximately one hour, and between one and three recording sessions were performed per day, interspersed with task sessions referenced above. Position data was recorded for 5 rats in this condition, yielding a total of 8 DAP across a total of 18 recording sessions.

Random foraging: Data from one rat was also obtained during a task where the rat foraged for randomly dispersed food rewards in an open field 100x100 cm with 50 cm high walls, each with a distinct visual cue. Each session lasted approximately 20 minutes. 4 DAP were recorded across a total of 8 recording sessions in this condition. There were no notable differences between data from the Rest Box and Random Foraging conditions, and so were combined for analysis for Figures 3-5, 3-6, and Extended Data Figures 3-8, 3-9, and 3-10.

Behavioral state identification: Spectral features of the LFP were used to estimate behavioral state. The 32 (40) kHz continuous traces were downsampled by a factor of 8 to 4 (5) kHz and digitally filtered with a zero-phase second order Butterworth bandpass filter with cutoff frequencies of 0.5 and 500 Hz. Using the built-in MATLAB function spectrogram( ), the power spectral density of the LFP was estimated using five-second periods shifted by one second,

yielding a spectrogram with a frequency resolution of 0.4 Hz and a temporal resolution of 1 second. This spectrogram was smoothed by 2-dimensional convolution with a Gaussian kernel of standard deviation 0.4 Hz and 1 second.

Using the resulting spectrogram, rat behavior was manually classified into two categories: slow wave sleep (SWS) and running (RUN). Time periods corresponding to whisker twitching, sleep spindles, handling by experimenters, or other movement artifacts were discarded. SWS was defined as time periods with elevated power in the 1.5-5 Hz (delta) band, reflecting large amplitude cortical up and down states (UDS). Remaining time periods were defined as RUN, long segments at least 20 s long, typically lasting several minutes. These segments included fast movements, slow movements and brief periods of relative quiescence. When available, these classifications were confirmed by tetrodes located in the CA1 region of the hippocampus showing elevated power in the 6-12 Hz theta band, a typical signature of movement, or directly with video recording.

Extracellular electrophysiology and spike sorting

Extracellular unit classification: Spike extraction, spike sorting and single unit classification were done offline using custom software and according to methods described previously[34,36]. Extracellular waveforms were extracted from the LFP filtered between 300 and 9000 Hz with a zero-phase second order Butterworth bandpass filter. Peaks with values above an adaptive threshold based on the magnitude of the noise in the signal (typically >40 μV) were identified as putative somatic action potentials.

Because we compare firing rate properties between extracellular units and DAP, we used the spike waveform to classify the putative neuron type of extracellular units. After manual spike sorting to assign spikes to isolated units, the average spike waveform was estimated as the mean across all spikes within a cluster. The width at half-maximum and time from spike peak to trough were then computed for each cluster. Only units from neocortex with a mean firing rate above 0.05 Hz in either SWS or RUN, as well as a half-width below 0.45 ms were included in all analyses. Units were classified as either pyramidal neurons or interneurons based on a combination of these measures. Units satisfying 1.6*W + P > 0.95 were identified as putative pyramidal neurons, and units satisfying 1.6*W + P <= 0.95 were identified as putative interneurons, where W is the width at half-maximum and P is the time from spike peak to the trough immediately after the peak. The parameters defining this equation were chosen to achieve maximal separation between two clusters in the width vs peak-to-trough space, and are consistent with previous studies[37].

Complex spike index (CSI): All CSI data presented were computed only using spikes in SWS to eliminate potential behavioral bias. For all pairs of adjacent spikes with spike time T_n and amplitude A_n and belonging to a single unit, the inter-spike-interval (ISI) was defined as

$$ISI = T_n - T_{n-1}$$

and the adaptation index (ADI) was defined as the ratio

$$ADI = \frac{A_n - A_{n-1}}{A_n + A_{n-1}}$$

The CSI was then computed as

$$CSI = 100 * \frac{S-L}{S+L}$$

where S is the number of spike pairs with ISI < 20 ms and ADI < 0, and L is the number of spike pairs with ISI < 20 ms and ADI >=0. Any other spike property can be substituted for amplitude to quantify the degree of change with repeated activation. Since the rising phase of the derivative of intracellular somatic spikes corresponds to the rising phase of extracellular spikes[69], the DAP CSI reported in Figure 3-3e is computed for the peak value of the first temporal derivative. CSI computed for DAP rise time and width are reported as the negative of the above formula, as rise time and width were observed to increase with repeated activation, rather than decrease.

MUA estimation: All MUA data presented were computed only using spikes in SWS. For a given tetrode, only detected spikes with a half-width between 0.05 and 0.45 ms and a peak-to-trough time between 0.3 and 1.2 ms were included in MUA calculations. This eliminates contamination by spurious events. The MUA amplitude for a given tetrode was computed as the mean of all spike amplitudes across all four tetrode channels, and the rate was computed as the number of spikes divided by the amount of time spent in SWS. MUA rate estimated thusly is not independent of MUA amplitude, as spikes with an amplitude below the adaptive detection threshold will not contribute to the MUA rate.

Amplitude Variation: Given the amplitude of a spike (Extracellular or DAP) on all four channels of a tetrode A_1, A_2, A_3, A_4, and the mean amplitude

$$\bar{A} = \frac{\sum_{i=1}^{4} A_i}{4}$$

the amplitude variation is defined as

$$\text{Amplitude Variation} = \sqrt{\frac{\sum_{i=1}^{4} (A_i - \bar{A})^2}{4}}$$

For recording sessions prior to (PRE) and following (POST) dendritic recording, amplitude variation was computed over the amplitude of all spikes from a single extracellularly-measured unit. During dendritic recording, amplitude RMS was computed over the amplitude of all spikes from a single DAP.

Dendritic detection and quantification

DAP Detection: Detection of putative DAP was performed on the individual tetrode channel with the largest amplitude-fluctuations. The continuous trace was filtered below 1500 Hz with a zero-phase second order Butterworth lowpass filter. Positive peaks in the first temporal derivative were identified as putative DAP, and the peak value of the second derivative immediately before the first derivative was recorded for each. Using these times, analogous values were obtained on each of the other tetrode channels. DAP were manually separated from noise offline using custom MATLAB scripts based on the first and second derivative peaks on all four channels (Extended Data Fig. 3-1).

DAP Quantification: The initiation time of a DAP was defined as the time of the peak of the third derivative immediately preceding the peak in the first derivative (Fig. 3-1d). The end of the rising phase of the DAP was defined as the time of the peak of the third derivative immediately following the first derivative peak. DAP rise time and amplitude were defined as the time difference and voltage difference, respectively, between these two points. Due to the large range of signal amplitudes across recordings, we did not establish a static threshold of dV/dt to detect DAP in order to eliminate biases. To calculate DAP width, the voltage trace was additionally

filtered above 15 Hz with a zero-phase second order Butterworth highpass filter. Half-amplitude crossing points were identified up to 3 ms before DAP peak and 30 ms after DAP peak (Fig. 3-1d). If no such points were identified for a particular DAP (<5% of all spikes), the width was excluded from further analysis.

Duration of Recording: The duration of each DMP recording was defined as the time difference between the end of the last session and the beginning of the first session containing intracellular signatures on a given tetrode. Hence, the reported hold times are likely underestimates of the true DMP hold time. A signal recorded on the same tetrode on consecutive days was designated to be the same DMP based on the similarities of DAP waveform and firing rate, and unchanged tetrode depth.

Peak Rate and Inter-spike Interval Calculations: The shortest ISI reported in Extended Data Figure 3-5 was calculated as the lowest 5% of the ISI histogram. The peak rate reported in Extended Data Figure 3-6 was defined as the reciprocal of the lowest 5% of the ISI histogram.

Impedance Spectroscopy: As a confirmation of the glial sheath hypothesis described in Extended Data Figure 3-3a-c, we measured the impedance of electrodes *in vivo* during dendritic recording and compared that to electrodes that were recording local field potential (Extended Data Fig. 3-3d, e).While the rat rested in the sleep box, the impedance of all channels on 7 tetrodes was measured at 20, 50, 100, 200, 500, 1000 and 2000 Hz, using the same Neuralynx hardware used to monitor impedance during electroplating (see above).

The impedance thus measured is typically modeled as a combination of several components. First, the electrode-electrolyte interface is modeled as a constant phase element (CPE), which has its impedance in the form:

$$Z_{CPE} = \frac{K}{(j\omega)^{\alpha}}$$

Here K represents the overall magnitude of the impedance, j is the imaginary number $\sqrt{-1}$, ω is the frequency, and α is constrained between 0 and 1. As α approaches 0, the behavior of the CPE approaches that of a pure resistor. As α approaches 1, the behavior approaches that of a pure capacitor.

The second component of the modeled impedance is the impedance of the surrounding glial tissue between the electrode and ground. There are two such pathways, one directly through the surrounding glial cells, which is modeled as a second CPE, and one through the space between glial cells, modeled as a frequency-independent resistor.

For each electrode, the 5 parameters ($K_{electrode}$, $\alpha_{electrode}$, K_{glia}, α_{glia}, R_{glia}) were estimated by minimizing the following function:

$$J = \sum_{i=1}^{N} \left(\frac{(Z'_i - \dot{Z}'_i)^2}{(\dot{Z}'_i)^2} + \frac{(Z''_i - \dot{Z}''_i)^2}{(\dot{Z}''_i)^2} \right)$$

where i indicates the different frequencies, N represents the total number of frequencies, Z'_i represents the real part of the measured impedance at the specific frequency, $\dot{Z}'_i$ represents the corresponding model estimate, and Z''_i and $\dot{Z}''_i$ represent similar values for the imaginary part of the measured impedance. Parameters were estimated using the built-in patternsearch( ) function

in MATLAB. Different sets of initial values were tested and the results producing the minimum error were selected, thus improving the chances of obtaining the global minimum.

All 5 parameters were unconstrained during fitting, but a systematic relationship emerged between the pairs of parameters specifying the CPE elements (K and α). A thorough investigation of this relationship is beyond the scope of the current study, so only the K values for each CPE are reported.

Subthreshold Responses

Subthreshold Magnitude Estimation: To eliminate the possible influence of long timescale fluctuations in signal properties, all subthreshold analyses were performed on segments of data approximately 5 minutes in duration. To eliminate possible influences of refractoriness or biasing of the voltage due to the large DAP amplitude, the subthreshold trace was constructed by eliminating all data in the original voltage trace 4 ms after each DAP initiation point. The membrane potential range reported in Figures 3-4b-c, 3-5d, and Extended Data Figure 3-8d was defined as the difference between the 5^{th} and 95^{th} percentile of the distribution of voltages in the subthreshold trace.

Initiation Range: The DAP initiation voltage reported in Figures 3-4d, 3-5e, and Extended Data Figures 3-7d and 3-9a, c, e was defined as the subthreshold voltage at the time of DAP initiation. The initiation range for a given DAP was computed as the difference between the 5^{th} and 95^{th} percentile of the distribution of DAP initiation voltages.

Voltage-Rate (V-R) Curve: For each trace, the subthreshold voltage was split into 100 equally-spaced bins. The firing rate in each voltage bin was computed by dividing the number of DAP initiated in each voltage bin by the amount of time the DMP sampled the corresponding voltage bin. Voltage bins with less than 300 ms of data were excluded from analysis to eliminate artifacts. Using the built-in MATLAB function nlinfit( ), a logistic function of the form

$$R(V) = \frac{a}{1 + e^{-b*(V-c)}}$$

was then fit to the resulting data points, where a, b, and c are estimated constants.

The "dynamic voltage range" reported in Figures 3-4f, 3-5g, and Extended Data Figures 3-7e and 3-9f was defined as the difference between the voltages at which the V-R curve crossed 5% and 95% of the maximum firing rate of the V-R curve. The "firing rate range" reported in Figures 3-4f, 3-5g, and Extended Data Figures 3-7f and 3-9g was defined as the difference in firing rate between these two points. Two DAP sources did not have enough spikes in RUN to generate a V-R curve, and these were excluded from analysis in Figure 3-5g and Extended Data Figure 3-9f-h.

Goodness of Fit: The goodness of fit for fitted V-R curves in Figures 3-4f, and 3-5f, as well as Extended Data Figures 3-7c, d, h, and 3-9b, d, h was evaluated as the R-squared value of the estimated rates at each voltage compared to the observed rates. This value is scale-invariant, allowing comparison across DAP with disparate firing rates.

Solitary DAP Analysis: To isolate the influence of a DAP on subsequent DAP and DMP via adaptation or short-term plasticity, a second subthreshold trace was constructed as above but with 50 ms of data excluded after each DAP initiation point. All subthreshold analyses above were repeated on these DAP isolated data for Extended Data Figures 3-7 and 3-9.

Egocentric Responses

Position Tracking: Position originally sampled at an average of 55 Hz was interpolated to a uniform 50 Hz. To eliminate abrupt position changes due to transient LED occlusion, position was first smoothed using a median filter of 250 ms width. Position was then further smoothed using a 15-point moving mean filter, and then up-sampled by linear interpolation at all data points including the occluded data to 100 Hz. Instantaneous heading direction H(t) was calculated as done previously[84]:

$$\mathrm{H(t)} = \tan^{-1}\frac{dy(t)}{dx(t)}$$
$$dx(t) = x(t + 50ms) - x(t - 50ms)$$
$$dy(t) = y(t + 50ms) - y(t - 50ms)$$

Construction of Egocentric Rate Maps: Movement in an egocentric reference frame[45] was computed frame-by-frame by calculating the difference in position and heading direction between the start and end of a moving 100 ms time window.

$$r(t) = \sqrt{dx(t)^2 + dy(t)^2}$$
$$dH(t) = H(t + 50ms) - H(t - 50ms)$$

$$DX_{ego}(t) = r(t) * \cos(dH(t))$$
$$DY_{ego}(t) = r(t) * \sin(dH(t))$$

Two-dimensional egocentric movement ($DX_{ego}(t)$ and $DY_{ego}(t)$) were then down-sampled to 50 Hz, binned using 0.25 cm bins in egocentric space, and smoothed by 2-dimensional convolution with a Gaussian kernel of standard deviation 0.25 cm in each dimension. Egocentric firing rate maps were generated by dividing the number of spikes occurring in each egocentric bin by the total time spent in the corresponding bin. Bins occupied less than 250 ms for every 20 minutes of recording were discarded. Maps constructed with 0.25 cm bins were used for all figures, and all statistics (below) were calculated from maps constructed with 0.15 cm bins as done previously[84]. For figures, displacement (cm) was converted to speed (cm/s) by dividing by 100 ms.

Information Content: Selectivity of egocentric rate maps was quantified by information content, as described previously for two-dimensional place fields[36]. To evaluate the anticipatory properties of rate maps, information content was evaluated for maps constructed using a time-shifting procedure. For a given unit or DAP, the time of all spikes were circularly shifted by an amount between ±1 second, with a resolution of 20 ms, while preserving the temporal structure of spikes. Information content was evaluated for each of these time lags, and the largest information content and the time lag it occurred at were recorded. Information content was calculated from smoothed rate maps with 0.15 cm bins.

Statistical significance was assessed by using a boot-strapping procedure, using a similar time-shifting method as above, but with larger shift amounts, between 200 and 1000 seconds. This was repeated 1000 times with different shift amounts to construct a null distribution. The

percentage of null data that was greater than the maximum information content of the original rate map was evaluated as the p-value for the null hypothesis that the information content came from the null distribution. Significance was only assessed for the maximal information content of each rate map.

Coherence: Egocentric rate map coherence was calculated by evaluating the correlation coefficient between each pixel of a rate map and the mean of all surrounding pixels[45]. Pixels with undefined firing rate were excluded from this analysis. Coherence was evaluated at the time lag of maximal information content, and was computed on un-smoothed rate maps with 0.15 cm bins.

Number of Dendrites: Multiple recording sessions for a dendrite were kept separate for egocentric analyses. Thus the dendritic sample size for egocentric comparisons is the number of sessions across all dendrites recorded with position data. The 22 recording sessions were divided between 7 independent dendritic sources.

Statistics

Significance Tests: All analyses were done offline using custom-written codes in MATLAB. Due to the relatively small dendritic sample size and potential non-Gaussian distribution of measures, we employed non-parametric tests and resampling statistics to assess statistical significance. Significance between unpaired data was assessed using the Wilcoxon rank-sum test. Significance between paired data was assessed using the Wilcoxon signed-rank test. These tests make few assumptions about the distributions of data being tested and are robust to non-equal sample sizes or non-Gaussian nature of data. Correlation coefficients and their related

significance were calculated using the built-in corrcoef( ) function in MATLAB, which calculates a two-sided *t* statistic to assess significance.

Confidence Intervals: Unless otherwise stated, all values are reported as median [95% confidence interval], in the form M [L, U], with M representing the median and L and U representing the lower and upper bounds, respectively, of the 95% confidence interval. Confidence intervals were estimated using resampling statistics to allow analysis of non-Gaussian distributions. Briefly, a surrogate population was constructed by drawing with replacement from the original distribution and the median of the resulting distribution recorded. This was repeated 100,000 times to form a distribution of the estimated median. The cutoff values of the 2.5^{th} and 97.5^{th} percentile of the estimated distribution were designated as the 95% confidence interval of the original population.

Validation of Detection Algorithm and Generation of Surrogate High Rate Data: The fidelity of the detection algorithm was validated by constructing surrogate data sets with known spike times. A typical DAP waveform normalized to an amplitude of 1 mV was convolved with impulses spaced at varying distances, and Gaussian noise with standard deviation of 0.1 mV was added. The detection algorithm was run on the resulting trace. The minimal interval between spikes the algorithm could detect was 0.4 ms. The noise level plotted in Extended Data Figure 3-5e was computed as the 99.99^{th} percentile of the distribution of peaks in the derivative of the surrogate signal, and serves as a visual guide.

To verify that the high DAP firing rates were not a product of multiple, independent sources being pooled together, surrogate data was simulated and quantified in Extended Data Figure 3-5e-g. Inter-spike intervals (ISI) were generated from a gamma distribution with shape parameter

1.75 and an appropriate scale parameter to generate a mean ISI of *1/f*, where *f* is the desired firing rate. The shape parameter of 1.75 was chosen to eliminate the majority of ISI less than 2 ms and to fit the observed ISI distributions of DAP. Few remaining ISI <3 ms (<1% of all data) were discarded. Spike times were then generated by taking the cumulative sum of the intervals. Impulses were scaled by a random amplitude drawn from the distribution of amplitudes from a sample DAP (mean 1.5 mV), and then convolved with a canonical DAP waveform with peak value 1. Finally, Gaussian noise with standard deviation of 0.05 mV was added. The detection method described above was then applied to the resulting traces to compute the histograms shown in Extended Data Figure 3-5f and 3-g.

Extended Data Figures and Figure Legends

Extended Data Table 3-1 | Comparison of Spike Types.

Type of Spike	Amplitude (mV)	Rise Time (ms)	Width* (ms)
Putative DAP in our data	**0.15 to 20**	**0.6 to 0.9**	**1 to 9**
Local DAP *in vitro* and *in vivo* (sodium) [40,42,44,45,53,59]	10 to 80	0.25 to 1.8	0.6 to 12
bAP *in vitro* and *in vivo* (sodium) [40,42,44–46,53,58,59]	10 to 80	0.72 to 1.8	1 to 12
Quasi-intracellular somatic sodium spike [64–68]	2 to 40	0.25 to 1	0.5 to 2
Somatic sodium spike [40,44–46,58]	60 to 110	0.3 to 0.7	0.55 to 1
Calcium spike [40,45,46,58]	10 to 65	3 to 9	10 to 56

Characterization of the amplitude, rise time, and width for putative DAP from the current study compared to the same measures for different types of intracellularly-recorded spikes. Note that our data have widths approximately an order of magnitude larger than somatic sodium spikes but an order of magnitude smaller than calcium spikes, making these unlikely explanations for our data, but match dendritic sodium spike properties.
**: "Width" refers to width at the base for calcium spikes, and width at half maximum for all others.*

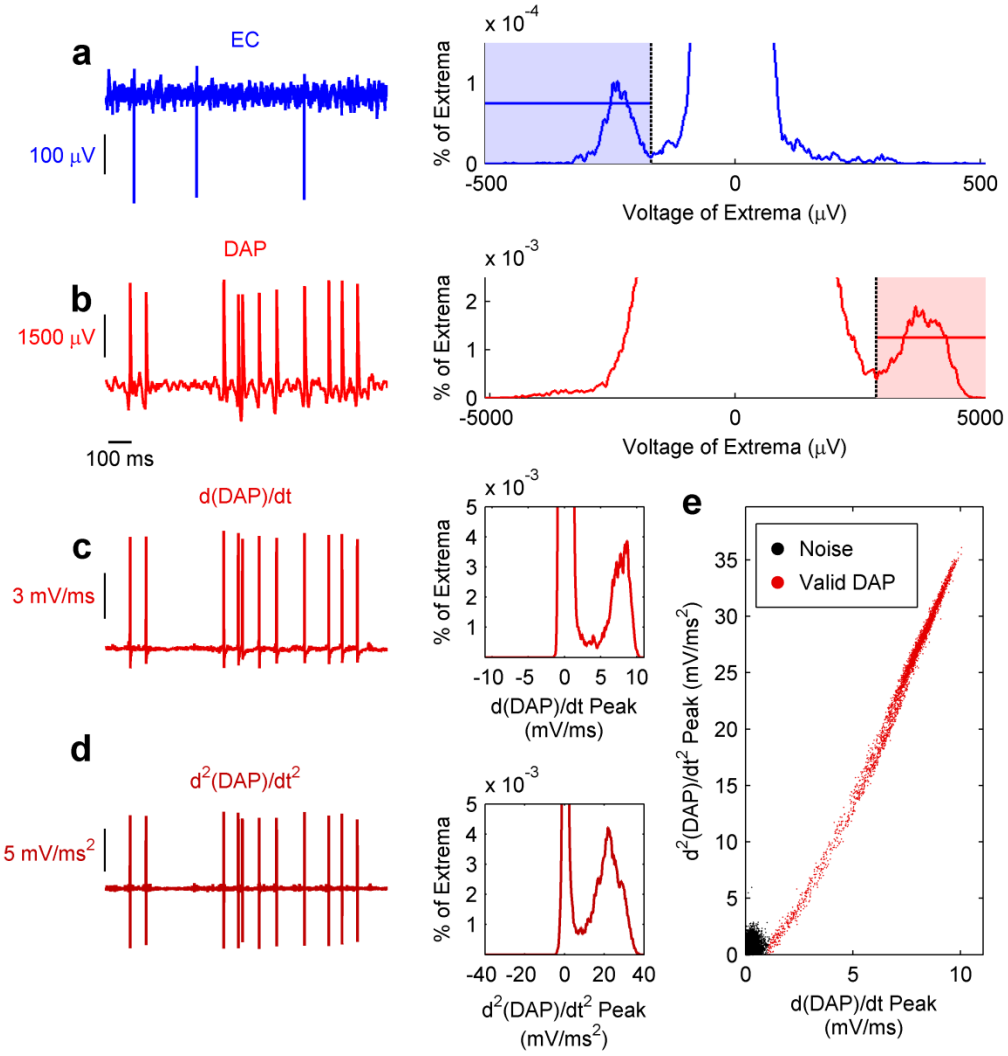

Extended Data Figure 3-1 | Distributions of somatic spikes, DAP and its derivatives.
a, Left, example segment of an LFP trace filtered between 20 and 9000 Hz showing negative-polarity spikes. Right, histogram of all extrema (maxima and minima) detected in the entire LFP trace, showing a prominent cluster of peaks around −240 μV (shaded) and no prominent cluster of positive extrema. The y-axis is limited to cut off the large number of peaks in the noise cloud. **b,** Left, example segment of an MP trace similarly filtered showing positive-polarity spikes. Right, histogram of all extrema detected in the entire MP trace, showing a prominent cluster of peaks around 3800 μV (shaded) and no prominent cluster of negative extrema. As in **a**, the y-axis is limited. **c,** Left, the first temporal derivative of the MP trace in **b** shows peaks clearly separated from the noise of the rest of the trace (right). **d,** Left, the second temporal derivative of the MP trace in **b** also shows clearly separated peaks (right). **e,** For all putative DAP, identified by peaks in the first temporal derivative, the 1st derivative peak and the immediately preceding 2nd derivative peak are plotted against each other. Data points that extend beyond the noise cloud (black) are identified as DAP (red).

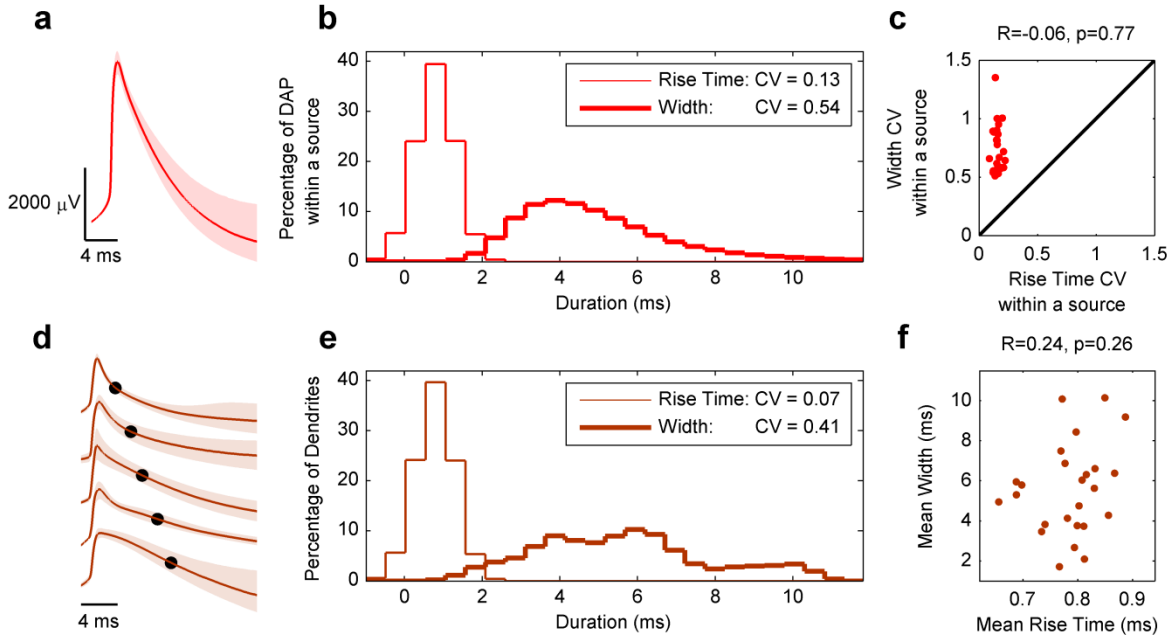

Extended Data Figure 3-2 | Variability of DAP Width and Rise Time.
a, Average waveform (median and 25th, 75th quantile, n=8917 DAP) for one DAP recording source shows less variation on the rising phase compared to the falling phase. **b,** For a single dendrite source, the rise time (0.69, [0.60, 0.78] ms, n=67714 DAP, CV=0.13) was smaller (p=0, Wilcoxon signed-rank test) and less variable than the half-width (5.30, [2.42, 8.18] ms, n=67714 DAP, CV = 0.54). **c,** Across the population of DAP, width CV (0.67, [0.58, 0.87], n=25 dendrites) was always greater ($p=1.2x10^{-5}$, Wilcoxon signed-rank test) than the CV of rise time (0.15, [0.14, 0.17], n=25 dendrites). Width CV and rise time CV were not significantly correlated (r = -0.06, [-0.45, 0.34], n=25 dendrites, p=0.77, two-sided *t* test). **d,** Average waveforms for five different DAP show a large range of half-widths, marked by black dots. **e,** Across the population of DAP, rise time (0.78, [0.73, 0.84] ms, n=25 dendrites) was significantly shorter ($p=1.4x10^{-9}$, Wilcoxon signed-rank test) than half width (5.58, [3.30, 7.86] ms, n=25 dendrites), and half-width (CV=0.41) was more variable than rise time (CV=0.07). **f,** Across the population of DAP, rise time was not significantly correlated with half-width (r=0.24, [−0.18, 0.58], n=25 dendrites; p=0.26, two-sided *t* test). Throughout the figure, data are reported as median and 95% confidence interval of the median unless otherwise noted.

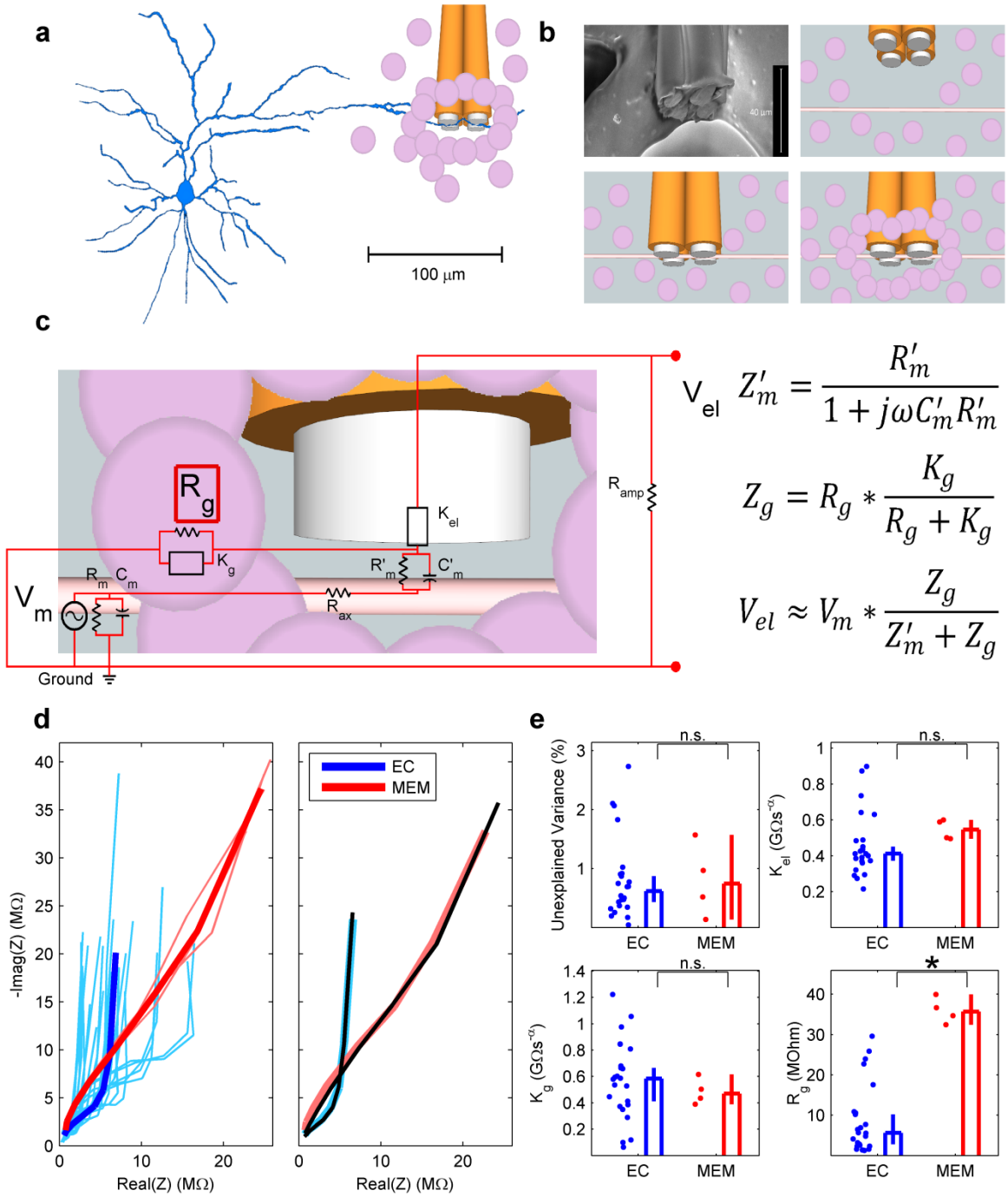

Extended Data Figure 3-3 | Proposed schematic of glial sheath mechanism of DAP recordings. **a,** Proposed spatial arrangement of a model, drawn to scale, of a tetrode and a model neuron with morphology characteristic of neocortical pyramidal neurons. The tetrode has cradled a thin dendrite several hundred µm from the cell soma. **b,** Panel 1 shows a scanning-electron microscope image of a typical tetrode used for implantation. The following panels show a model tetrode (gray and orange) advancing down into the brain (Panel 2) and coming in to close apposition to a dendrite (red, Panel 3). The glial sheath gradually encapsulates the tetrode and dendrite (purple, Panel 4). **c,** Electrical circuit equivalent. The voltage difference between the electrode tip and ground will be proportional to the

voltage difference between the inside of the dendrite and ground, and the overall magnitude will depend on the relative values of the membrane impedance Z_m and glial seal impedance Z_g. In typical extracellular recordings, Z_g is negligible compared to Z_m, so no intracellular signal is recorded. Not depicted, impedance of the electrode-electrolyte interface, axial resistance of the electrode wire, and leak capacitance of the wire, all of which are typically orders of magnitude smaller than the impedances shown. R_{amp} represents the resistance across the amplifier used to record signals and is typically several orders of magnitude larger than the impedances shown and so can safely be ignored, as can R_{ax}, the axial resistance within the dendrite, which is typically several orders of magnitude smaller. **d,** Left, impedance spectra for normal extracellular (light blue) and DAP-recording (light red) electrodes shows increased impedance for the DAP-recording electrodes. Right, an electric circuit equivalent of glial encapsulation of a tetrode well approximates sample impedances for both extracellular and DAP-recording electrodes. **e,** The percentage variance unexplained (top left) for extracellular electrodes (0.62, [0.43, 0.87] %, n=24 electrodes) was very low, and not significantly different (p=0.87, Wilcoxon rank-sum test) from that for DAP-recording electrodes (0.74, [0.14, 1.57] %, n=4 electrodes). The fitted model parameters for K_{el} (top right, EC, 0.41, [0.37, 0.46] $G\Omega*s^{-\alpha}$; MEM, 0.55, [0.50, 0.60] $G\Omega*s^{-\alpha}$) and K_g (bottom left, EC, 0.58, [0.41, 0.67] $G\Omega*s^{-\alpha}$; MEM, 0.47, [0.39, 0.62] $G\Omega*s^{-\alpha}$) were not significantly different from each other (K_{el}, $p=7.1x10^{-2}$, Wilcoxon rank-sum test; K_g, p=0.58, Wilcoxon rank-sum test). In contrast, R_g for MEM (bottom right, 35.7, [32.5, 40.0] MΩ) was significantly ($p=1.8x10^{-3}$, Wilcoxon rank-sum test) larger than R_g for EC (5.61, [2.80, 10.2] MΩ), supportive of our hypothesis that dendritic membrane potential recordings result from an increase in the seal of glia around the tetrode.

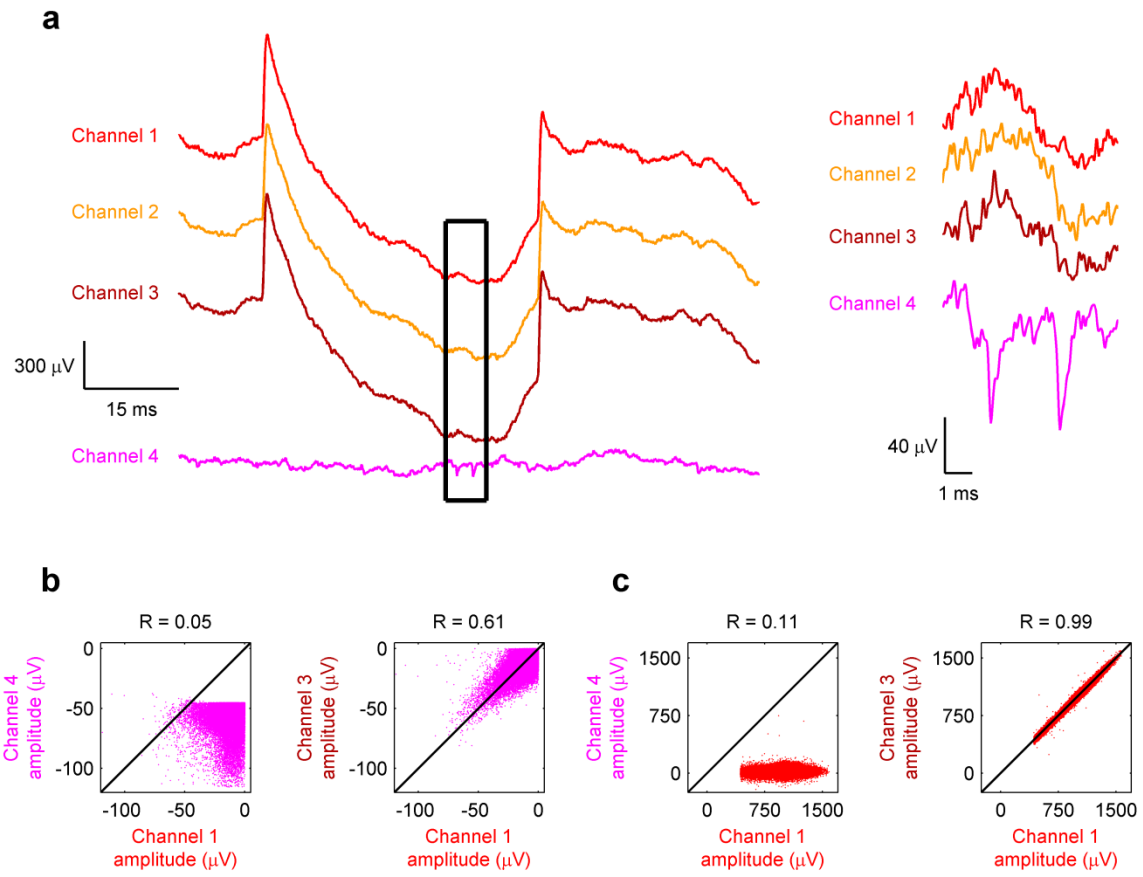

Extended Data Figure 3-4 | Reduction of MUA on tetrode channels with DMP signal.
a, Sample trace from a tetrode in which 3 channels recorded DMP (red, orange, brown) but one channel (magenta) did not. No signature of DAP, which are clearly visible on channels 1-3, are visible on channel 4, and no signature of extracellular spikes, which are clearly visible on channel 4 (inset), are visible on channels 1-3. **b,** Extracellular spikes were detected and triggered on channel 4, and the corresponding amplitude recorded on all 4 channels, 2 (out of six possible) combinations of which are shown in scatterplots. Left, channel 4 typically records higher amplitude (more negative) extracellular spikes that are uncorrelated with the amplitude on channels 1-3 (only channels 1 and 4 are shown). Right, extracellular spike amplitude is weakly correlated between channels 1-3 (only channels 1 and 3 are shown). **c,** DAP were detected on channels 1-3, and their amplitude recorded on all 4 channels, 2 combinations of which are shown in scatterplots. Left, channel 4 typically records much smaller amplitude DAP compared to channels 1-3 (only channels 1 and 4 are shown). Right, DAP amplitude on channels 1-3 are highly correlated (only channels 1 and 3 are shown). This shows that the tetrode channel that did not have DAP signal had greater amount of MUA activity, further supporting the glial sheath hypothesis of DAP measurement.

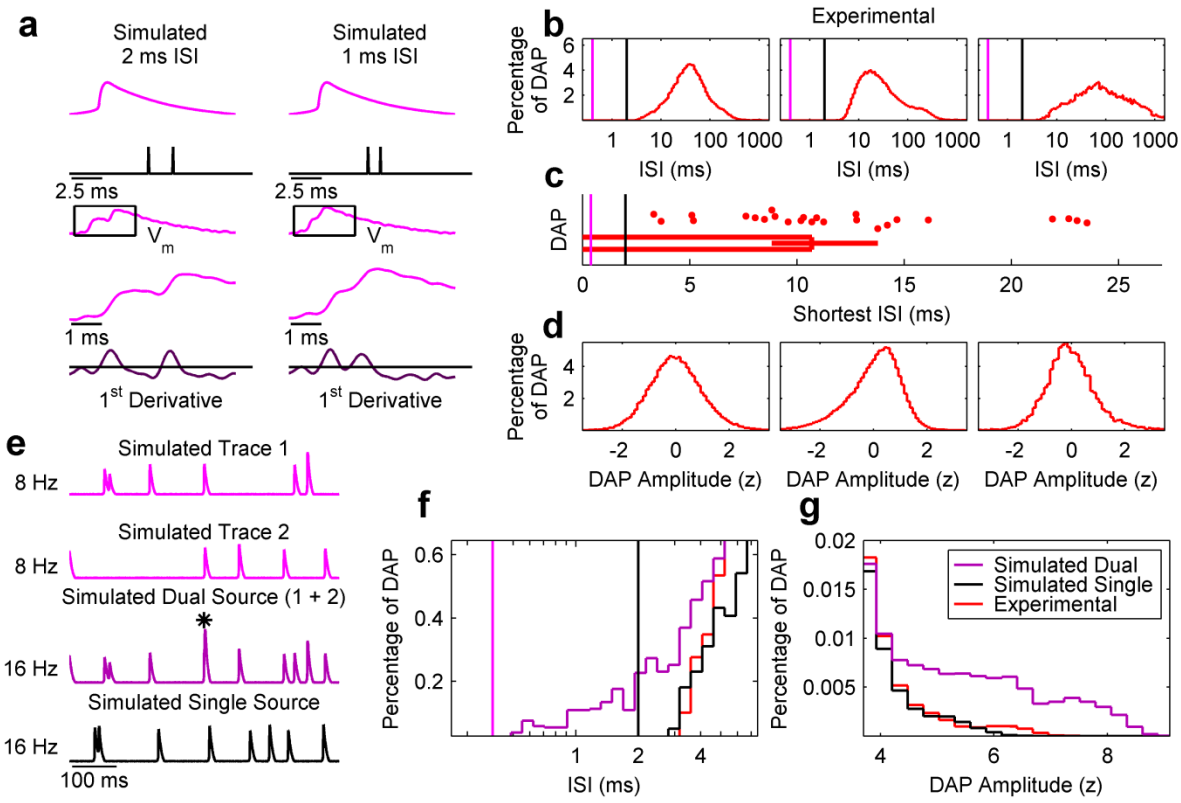

Extended Data Figure 3-5 | Validation of DAP detection algorithm and separated nature of measured DAP.

a, Convolution of a typical DAP waveform (top row) with impulses spaced 2 (left), and 1 (right) ms apart. In each row, the y-axis has arbitrary units but identical for the left and right plots. First temporal derivatives of the above traces are plotted in dark purple. In both examples, two peaks above the noise level (see Methods) are clearly distinguishable. **b,** Inter-spike-interval (ISI) histograms of 3 separate experimentally recorded DAP. The black and magenta lines mark the 2 ms interval designating a typical neuronal refractory period and the shortest ISI (0.4 ms) our detection method can distinguish, respectively. **c,** Across the population of DAP, the minimum ISI (10.7, [8.82, 13.8] ms, n=25 dendrites) was significantly longer than the 2 ms refractory period ($p=1.2x10^{-5}$, Wilcoxon signed-rank test), as well as the 0.4 ms resolution limit of our detection method. Data are reported and presented as median and 95% confidence interval of the median. **d,** Unimodal distributions of DAP amplitude are further evidence that each DAP is from a single source. **e,** Two surrogate 8 Hz DAP traces were generated from a gamma process (see Methods) (top two rows, magenta). These were summed together to generate a "Dual Source" 16 Hz DAP trace (third row, purple). The black asterisk indicates an inter-spike interval less than 2 ms. An additional "Single Source" 16 Hz DAP trace was generated from a single 16 Hz gamma distribution (bottom row, black). **f,** Zoomed-in region of the ISI histogram for the simulated dual source16 Hz trace (purple), the simulated single source 16 Hz trace (black), and data from the experimentally recorded DAP represented in the first panel of **b** (red). The dual source trace has several ISI <2 ms but these are absent in both the single source trace and the experimental DAP trace. **g,** Zoomed-in region of the amplitude histogram for the simulated dual source 16 Hz trace, the simulated single source trace, and the experimental DAP from the first panel of **d**. The dual source trace has several detected amplitudes greater than 5 standard deviations from the mean of the distribution, but these are absent in both the single source trace and the experimentally observed DAP. These large amplitude events

come from the summation of two spikes from two independent simulated 8 Hz sources that occur within 0.4 ms and cannot be resolved; these are not found in experimental data.

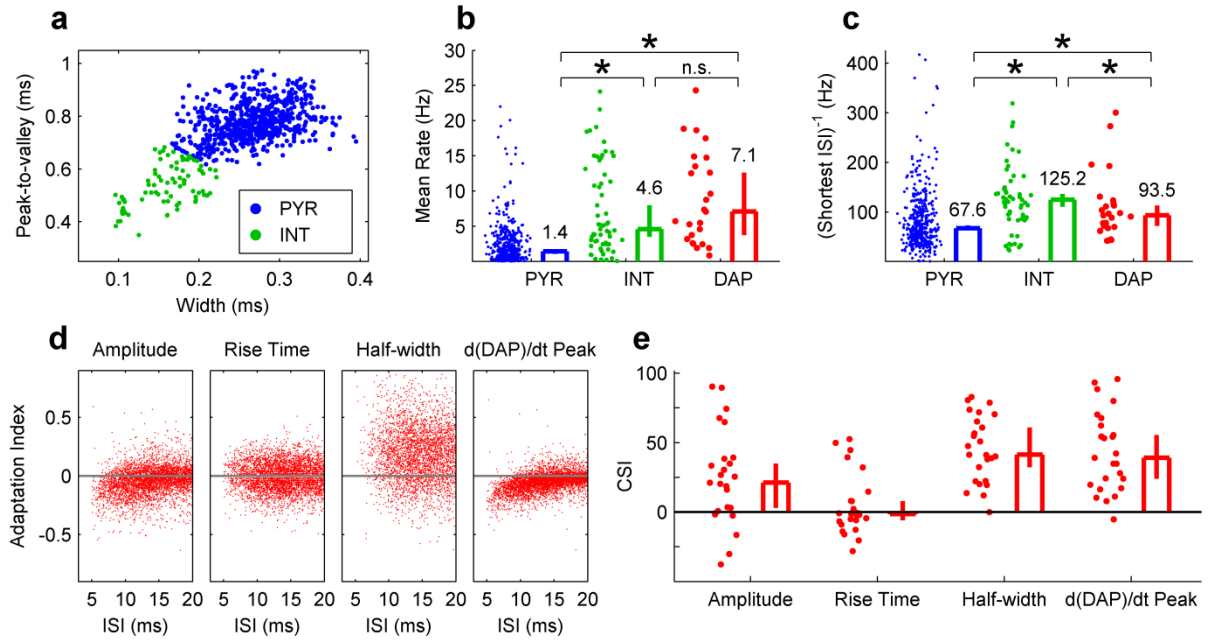

Extended Data Figure 3-6 | Spiking properties and short term plasticity of pyramidal neurons, interneurons, and DAP.

a, Pyramidal neurons and interneurons were identified based on their half-width and the time from the peak of the action potential to the trough after the peak (Peak-to-valley). 87% of extracellularly recorded neurons were classified as pyramidal neurons (657 units), and 13% were classified as interneurons (97 units). **b,** The mean firing rate of pyramidal neurons (1.41, [1.08, 1.65] Hz, n=657 units) was significantly smaller than both that of interneurons (4.59, [3.51, 7.96] Hz, n=97 units, $p=7.9x10^{-13}$, Wilcoxon rank-sum test), and that of DAP (7.07, [3.76, 12.6] Hz, n=25 dendrites, $p=1.3x10^{-9}$, Wilcoxon rank-sum test). DAP mean firing rate was not significantly different from that of interneurons (p=0.31, Wilcoxon rank-sum test). **c,** The peak firing rate of pyramidal neurons (defined as the inverse of lowest 5% of all ISI) (67.6, [63.5, 73.7] Hz, n=657 units) was significantly less than that of both interneurons (125, [111, 137] Hz, n=97 units, $p=5.2x10^{-9}$, Wilcoxon rank-sum test) and DAP (93.5, [72.7, 113] Hz, n=25 dendrites, $p=1.0x10^{-2}$, Wilcoxon rank-sum test). Interneurons also had significantly higher peak firing rates than DAP ($p=4.5x10^{-2}$, Wilcoxon rank-sum test). **d,** Example scatterplots of ISI versus amplitude, rise time, width, and 1st derivative peak demonstrate activity-dependent adaptation. **e,** For the population of DAP, CSI was significantly greater than 0 for measures of amplitude (21.1, [3.11, 34.8], n=25 dendrites, $p=2.3x10^{-3}$, Wilcoxon signed-rank test), , half-width (41.4, [32.4,60.9], n=25 dendrites, $p=1.8x10^{-5}$, Wilcoxon signed-rank test) and 1st derivative peak (39.1, [24.1,55.6], n=25 dendrites, $p=1.4x10^{-5}$, Wilcoxon signed-rank test), but not for rise time (−1.54, [−5.88, 7.87], n=25 dendrites, p=0.99, Wilcoxon signed-rank test). Throughout the figure, data are reported and presented as median and 95% confidence interval of the median. * indicates significance at the p<0.05 level, and n.s. indicates lack of significance at the p<0.05 level.

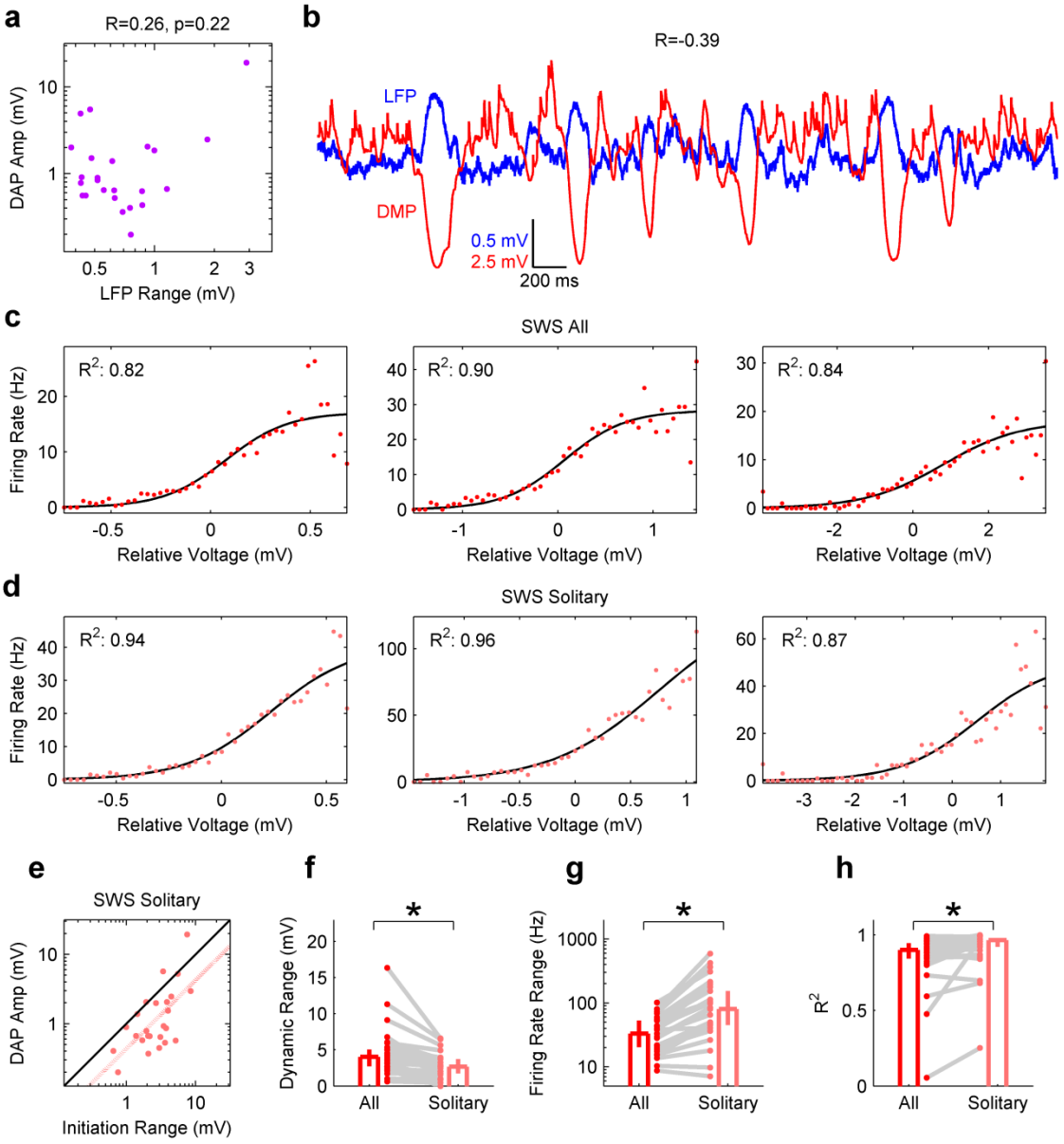

Extended Data Figure 3-7 | Modulation of DAP by subthreshold membrane potentials.
a, DAP amplitude was not significantly correlated (r=0.26, [−0.15, 0.59], n=25 dendrites; p=0.22, two-sided *t* test) with the range of LFP recorded simultaneously from a nearby tetrode, ruling out spurious noise artifacts. **b,** During SWS, simultaneously recorded LFP (blue) and DMP (red) show up-down states with reversed polarity with respect to each other. **c,** Sample Voltage-Rate (V-R) curves computed using all DAP within a session during SWS. **d,** Sample V-R curves for the same DAP in **c**, but for only those DAP and times separated from other DAP by at least 50 ms (Solitary). **e,** For solitary DAP in SWS, initiation range (2.99, [1.94, 3.73] mV, n=25 dendrites) was larger ($p=1.7\times10^{-4}$, Wilcoxon signed-rank test) than the corresponding DAP amplitude (0.86, [0.64, 1.98] mV, n=25 dendrites), and positively correlated (r=0.64, [0.32, 0.82], $p=6.3\times10^{-4}$, two-sided *t* test). **f,** The dynamic voltage range for solitary DAP (2.66 [1.75, 3.71], n=25 dendrites) was smaller ($p=1.7\times10^{-2}$, Wilcoxon signed-rank test) than for all

DAP (4.03, [2.74, 5.07], n=25 dendrites). **g,** The V-R firing rate range was significantly higher ($p=5.9x10^{-3}$, Wilcoxon signed-rank test) for solitary DAP (79.8, [45.5, 154] Hz, n=25 dendrites) compared to all DAP (33.1, [20.3, 53.1] Hz, n=25 dendrites). **h,** The goodness of the logistic fit of the VR-curve when calculated for solitary DAP (0.97, [0.92, 0.97], n=25 dendrites), was slightly larger ($p=2.0x10^{-2}$, Wilcoxon signed-rank test) compared to all DAP (0.90, [0.84, 0.95], n=25 dendrites). Throughout the figure, data are reported and presented as median and 95% confidence interval of the median, and * indicates significance at the $p<0.05$ level.

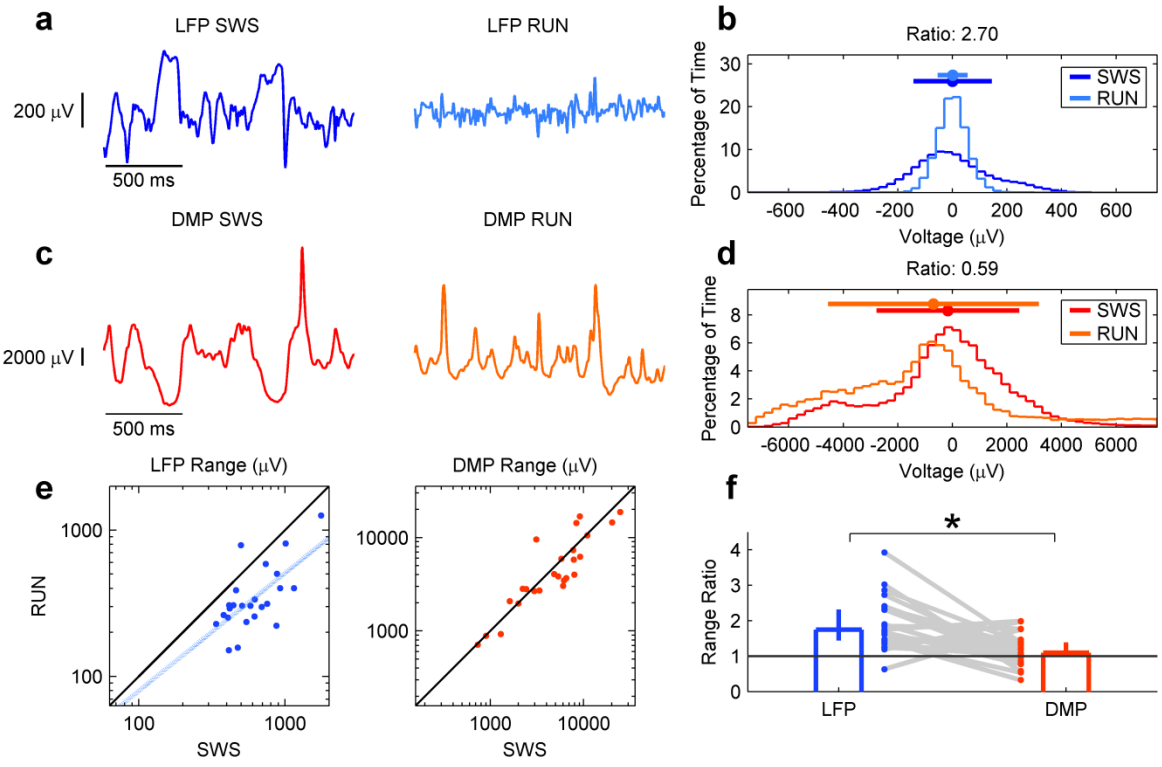

Extended Data Figure 3-8 | Comparison of LFP and subthreshold DMP modulation during SWS and RUN.

a, Sample segments of a spike-clipped LFP trace during SWS (left, blue) and RUN (right, light blue), showing smaller amplitude fluctuations during RUN. **b,** Histograms of the LFP voltage for the traces in **a**, showing a much wider range of variation in SWS (−265 to 215 μV, range of 480 μV) than during RUN (−89.7 to 87.9 μV, range of 178 μV). The ratio of SWS range to RUN range in this example is 2.70, indicating a much larger range in SWS. **c,** Sample segments of a spike-clipped MP trace during SWS (left, red) and RUN (right, orange), showing large amplitude fluctuations in both SWS and RUN. **d,** Histograms of the MP voltage for the traces in **c**, showing a similar range of variation in SWS (−4690to 3560 μV, range of 8250 μV) and RUN (−6080 to 7980 μV, range of 14100 μV). The ratio of SWS range to RUN range in this example is 0.59, indicating a comparable range in SWS and RUN. **e,** Left, spike-clipped local field potential range during RUN (306, [263, 401] μV, n=25 recording segments) was smaller ($p=4.1x10^{-5}$, Wilcoxon signed-rank test) than the local field potential range during SWS (578, [463, 755] μV, n=25 recording segments here and throughout the figure); the two ranges were also significantly correlated (r=0.74, [0.49, 0.88], $p=2.4x10^{-5}$, two-sided *t* test). Right, spike-clipped DMP range during RUN (3840, [2820, 6240] μV, n=25 recording segments) was not significantly different ($p=9.8x10^{-2}$, Wilcoxon signed-rank test) than that during SWS (5770, [2950, 7850] μV), and the two measures were significantly correlated (r=0.89, [0.76, 0.95], $p=2.710^{-9}$, two-sided *t* test). **f,** The ratio of SWS range to RUN range in the LFP (1.75, [1.45, 2.32], n=25 recording segments) was significantly greater than 1 ($p=2.3x10^{-5}$, Wilcoxon signed-rank test) and significantly greater ($p=4.6x10^{-5}$, Wilcoxon signed-rank test) than that of DAP (1.10, [1.01, 1.39]), which was not significantly different from 1 ($p=5.4x10^{-2}$, Wilcoxon signed-rank test).

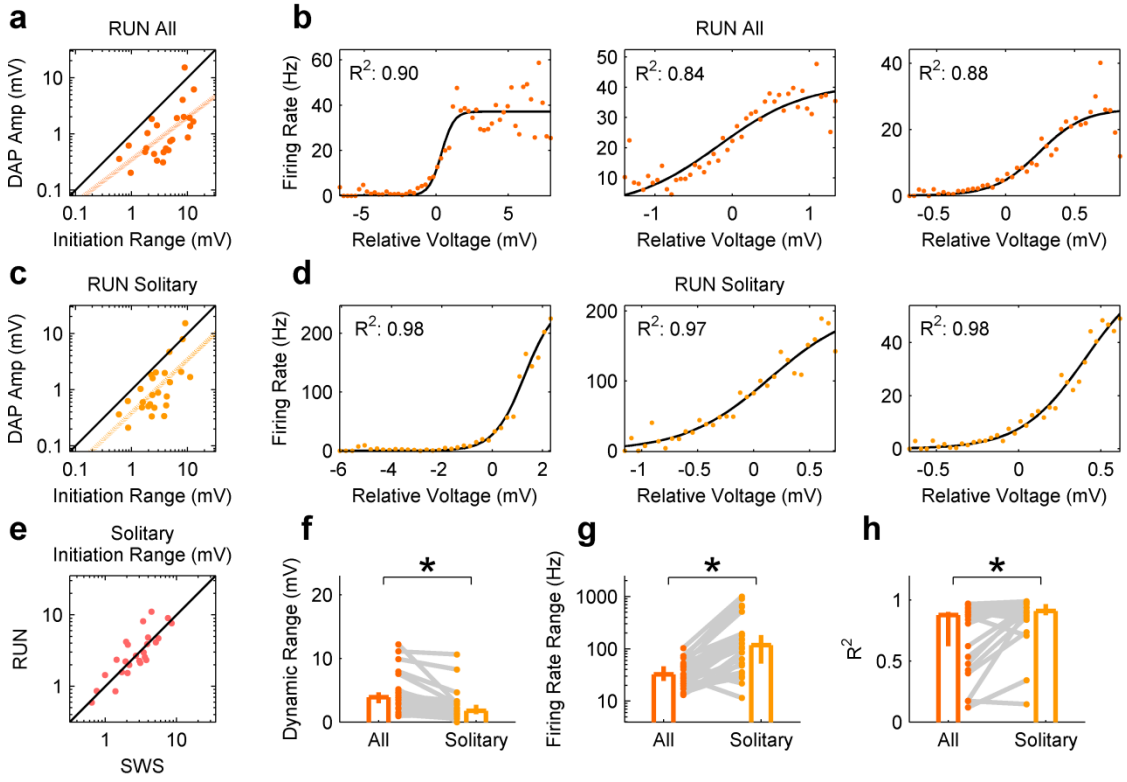

Extended Data Figure 3-9 | Properties of solitary DAP in SWS and RUN.
a, DAP initiation range in RUN (4.07, [2.51, 8.14] mV, n=25 dendrites) was larger ($p=2.0x10^{-5}$, Wilcoxon signed-rank test) than the corresponding DAP amplitude (0.79, [0.52, 1.66] mV, n=25 dendrites), and positively correlated (r=0.65, [0.35, 0.83], n=25 dendrites; $p=3.9x10^{-4}$, two-sided *t* test) **b,** Sample Voltage-Rate (V-R) curves for all DAP during RUN. **c,** For solitary DAP in RUN, initiation range (2.56, [2.14, 4.13] mV, n=25 dendrites) was larger ($p=4.1x10^{-5}$, Wilcoxon signed-rank test) than the corresponding DAP amplitude (0.80, [0.52, 1.68] mV, n=25 dendrites), and positively correlated (r=0.68, [0.40, 0.85]; $p=1.7x10^{-4}$, two-sided *t* test). **d,** Sample V-R curves for the same DAP in (b), but for only those DAP and times separated from other DAP by at least 50 ms. **e,** For solitary DAP, initiation range in SWS (2.99, [1.94, 3.73] mV, n=25 dendrites) and RUN (2.56, [2.14, 4.13] mV, n=25 dendrites) were correlated (r=0.84, [0.66, 0.93], n=25 dendrites, $p=1.7x10^{-7}$, two-sided *t* test) and not significantly different (p=0.74, Wilcoxon signed-rank test). **f,** The dynamic range for solitary DAP in RUN (1.80, [1.25, 2.69] mV, n=24 dendrites) was slightly reduced ($p=1.8x10^{-3}$, Wilcoxon signed-rank test), compared to all DAP in RUN (3.90, [2.98, 4.67] mV, n=24 dendrites). **g,** The V-R firing rate range was significantly higher ($p=2.3x10^{-4}$, Wilcoxon signed-rank test) for solitary DAP in RUN (117, [52.6, 183] Hz, n=24 dendrites) compared to all DAP in RUN (32.5, [24.6, 46.5] Hz, n=24 dendrites). **h,** The V-R curve in RUN was better approximated by the logistic fit ($p=3.8x10^{-2}$, Wilcoxon signed-rank test) when calculated for solitary DAP (0.91, [0.88, 0.97], n=24 dendrites) compared to all DAP (0.88, [0.62, 0.90], n=24 dendrites).

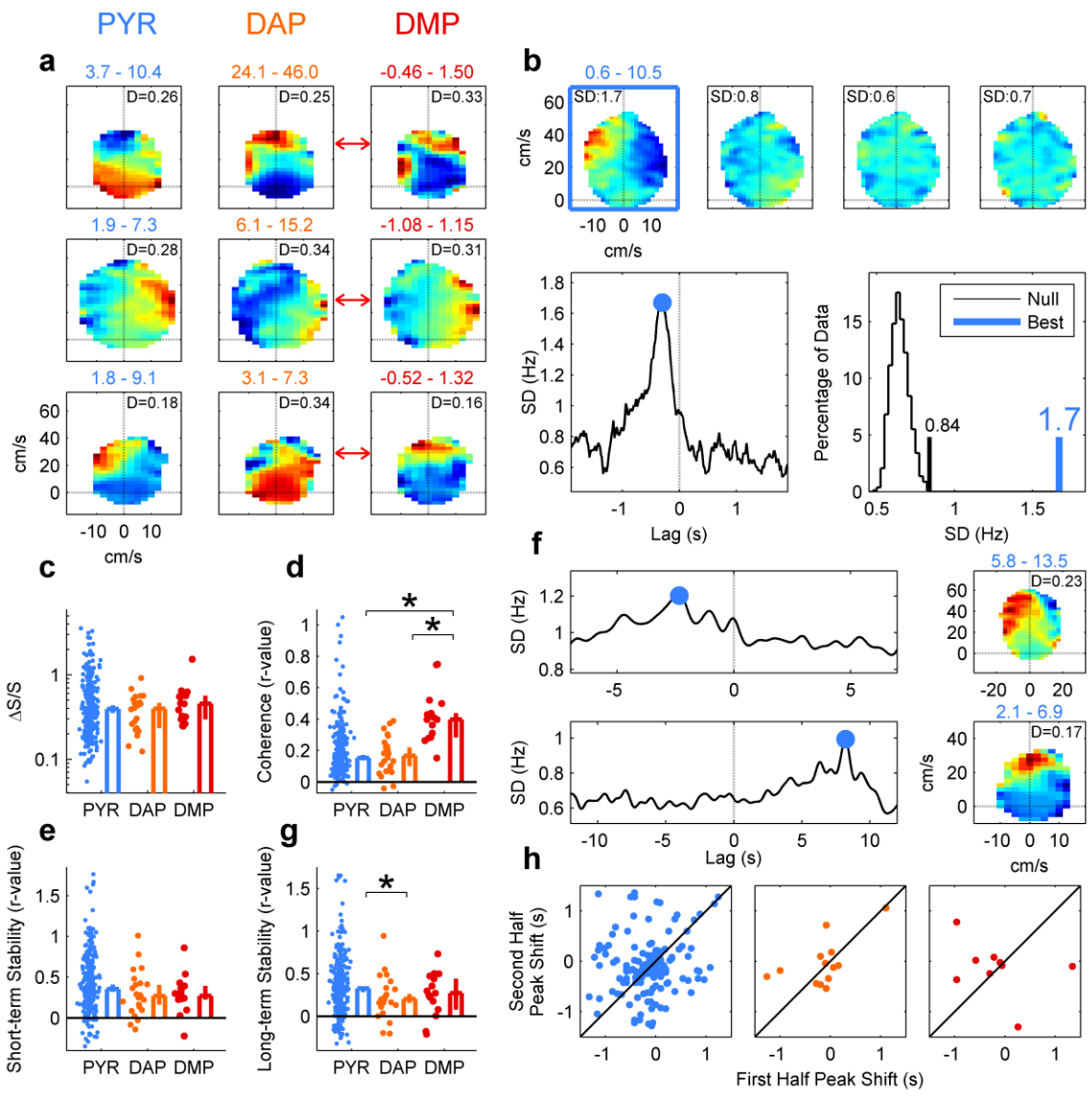

Extended Data Figure 3-10 | Sample egocentric rate maps, evaluation of significance, additional measures, and long-term stability.

a, Three sample pyramidal (left), DAP (middle), and DMP (right) egocentric maps. **b,** Illustration of shuffling method used to determine significance and optimal lag (see Methods). Neural data is shifted with respect to behavioral data by large amounts (up to ±20 seconds), and the standard deviation of the resulting maps (top) is plotted as a function of lag (bottom-left). To determine significance, the peak standard deviation (blue mark) is then compared to distribution of standard deviations at long time-lags (bottom-right). The black mark at 0.84 indicates the highest value at long time lags. Since the peak standard deviation (blue mark, 1.7) is larger than the entire null distribution, this unit is significantly tuned. **c,** Normalized standard deviation (ΔS/S), a measure of the depth of modulation of a map, was comparable between PYR (0.39, [0.35, 0.43], n=245 maps), DAP (0.40, [0.23, 0.46], n=24 maps), and DMP (0.46, [0.30, 0.57], n=15 maps), with no significant differences (PYR vs DAP, p=0.29; PYR vs DMP, p=0.68; DAP vs DMP, p=0.19, Wilcoxon rank-sum test for all). **d,** Coherence for both pyramidal soma (0.15, [0.14, 0.17, n=245 maps) and DAP (0.17, [0.10, 0.22], n=24 maps) was significantly smaller

than coherence of DMP (0.40, [0.31, 0.50], n=15 maps; PYR vs. DMP, $p=4.6x10^{-6}$, Wilcoxon rank-sum test; DAP vs DMP, $p=2.3x10^{-5}$, Wilcoxon rank-sum test), but DAP and pyramidal map coherence were not different from each other (p=0.6, Wilcoxon rank-sum test). **e,** Short-term stability for pyramidal neurons (0.35, [0.32, 0.41], n=245 maps) was higher than DAP (0.27, [0.17, 0.41], n=24 maps) and DMP (0.27, [0.24, 0.39], n=15 maps), but these differences were not statistically significant (PYR vs DAP, p=0.12, Wilcoxon rank-sum test; PYR vs DMP, p=0.25, Wilcoxon rank-sum test). DAP and DMP short-term stability were not significantly different from each other (DAP vs DMP, p=0.87, Wilcoxon rank-sum test). **f,** Two sample pyramidal neurons with an extremely large lag time of maximal standard deviation, at −2.22 s (top) and −8.22 s (bottom) respectively. **g,** Long-term stability (see Methods) for pyramidal soma (0.33, [0.29, 0.35], n=245 maps) was significantly larger ($p=3.8x10^{-2}$, Wilcoxon rank-sum test) than that of DAP (0.21, [0.16, 0.26], n=24 maps), and larger, but not significantly so (p=0.39, Wilcoxon rank-sum test) than that of DMP (0.27, [0.08, 0.48], n=15 maps). DAP and DMP long-term stability were not significantly different (p=0.38, Wilcoxon rank-sum test). **h,** The lag time of optimal tuning for pyramidal units was not significantly different (p=0.88, Wilcoxon signed-rank test) between the first half (-100, [-150, -60] ms, n=156 maps with significant tuning) and second half (-140, [-180, -80] ms) of recording sessions. There was also no significant changes between session halves for DAP (first half, -80, [-200, 20] ms, n=13 maps with significant tuning; second half, -120, [-340, 100] ms; p=0.75, Wilcoxon signed-rank test) or DMP (first half, -220, [-960, 260] ms, n=9 maps with significant tuning; second half, -80, [-360, 80] ms; p=0.48,Wilcoxon signed-rank test).

4. Hardware Development

To ask new questions, new hardware must sometimes be developed. The following projects are works in progress, functioning as either pilot tests of theories, or preparations for future studies.

Low-cost, Simple, Circuit Board for In-Vivo Stimulation

Motivation

Despite thorough and rigorous analyses, there is inevitably some doubt about the dendritic nature of the results described in Chapter 3 without more direct tests. While the signal analysis is fairly convincing, there are some tests that can be done with future dendritic recordings, given the proper equipment. One such method is to stimulate the dendrite, or otherwise pass current through the dendrite to perform such classical electrophysiological tests as measuring the membrane time constant, evaluating the relationship between injected current and firing rate (I-R relationship), and searching for any tell-tale signs of ion channels that are differentially expressed in the soma and dendrites.

In vitro work suggests that dendrites have a faster time constant than their corresponding somata. Stimulation would be able to reveal what the time constant is of the membrane we are recording from. Such experiments may also give us a better idea of the true resting membrane potential of the dendrite, a value unknown to us due to using AC-coupled amplifiers. Tonic depolarizations could also shed light on whether the observed spikes are dependent on sodium channels, as raising the resting membrane potential should inactivate such channels.

Measuring the I-R curve would serve two purposes. First, it may be expected that the I-R relationship would be different between dendrites and soma, due to the different diameters and local axial resistances of the two elements. Second, showing that the firing rate of DAP is manipulable be passing current would confirm that these spikes are indeed reflective of biological processes, and not simply recording artifacts due to faulty electronics.

Finally, certain types of ion channels are often expressed differentially in dendrites and soma, particularly ion channels mediating the "sag potential." These potentials are only seen in dendrites, and are mediated by HCN channels, which tend to be more strongly expressed in dendrites[94].

All of the above measures would provide more direct evidence that we are recording from dendritic processes, and not some warped record of somatic potential or electrical noise. Unfortunately, the current high-density recording set-up used in the lab is not conducive to such stimulation experiments; thus, new hardware must be introduced to make these experiments possible.

Physical Constraints

All tetrodes implanted into our rats come through an electrode interface board (EIB). Each wire is pinned to the EIB, which has a printed circuit-board designed to route signals to 3 large headers, or headstages. Each headstage contains all of the channels for 8 tetrodes, as well as ground and reference channels. These headstages are 36-pin male Omnetics connectors, sourced from Neuralynx, which interface through 36-pin female Omnetics connectors on a circuit board with pre-amplifiers, also sourced from Neuralynx. These headers are very dense, with adjacent pins separated by only 0.025 inches. The headers are also sheathed and polarized such that they

can only interface in an all-or-none fashion; electrical access to individual channels is practically impossible.

The pre-amplifiers are unity gain operational amplifiers (op-amps) from Texas Instruments that provide a high impedance (~1TΩ) buffer between the brain and the Neuralynx recording system. This effectively shields the recording system's electronics from any currents that might arise in the brain or at the tetrode tips. This is an important safety feature, but precludes our stimulating individual channels via software; any current directly passed through the op-amp would generate a massive voltage difference and likely cause damage to the circuitry.

A suitable workaround might be to discard the entire pre-amplifier for a given headstage, and interface with single pins on the headstage. While this would allow the connection between a current source and individual channels, such stimulation would be performed blindly. Real-time evaluation of the membrane voltage response to injected current would be unavailable, making the above-mentioned experiments unfeasible. Ideally, one would like to pass current between on one channel of a tetrode and ground, or between two channels of a tetrode, and simultaneously record the voltage response on the non-stimulated channels.

The solution to this problem came in the form of an intermediate circuit board, between the headstage and the pre-amp. The design allows the experimenter to interrupt the current path of certain tetrodes, connecting them to the stimulator, while leaving the other channels directly connected to the pre-amp. By injecting current between the op-amp and the electrode tips, all injected current will flow into the brain due to the op-amp's high resistance.

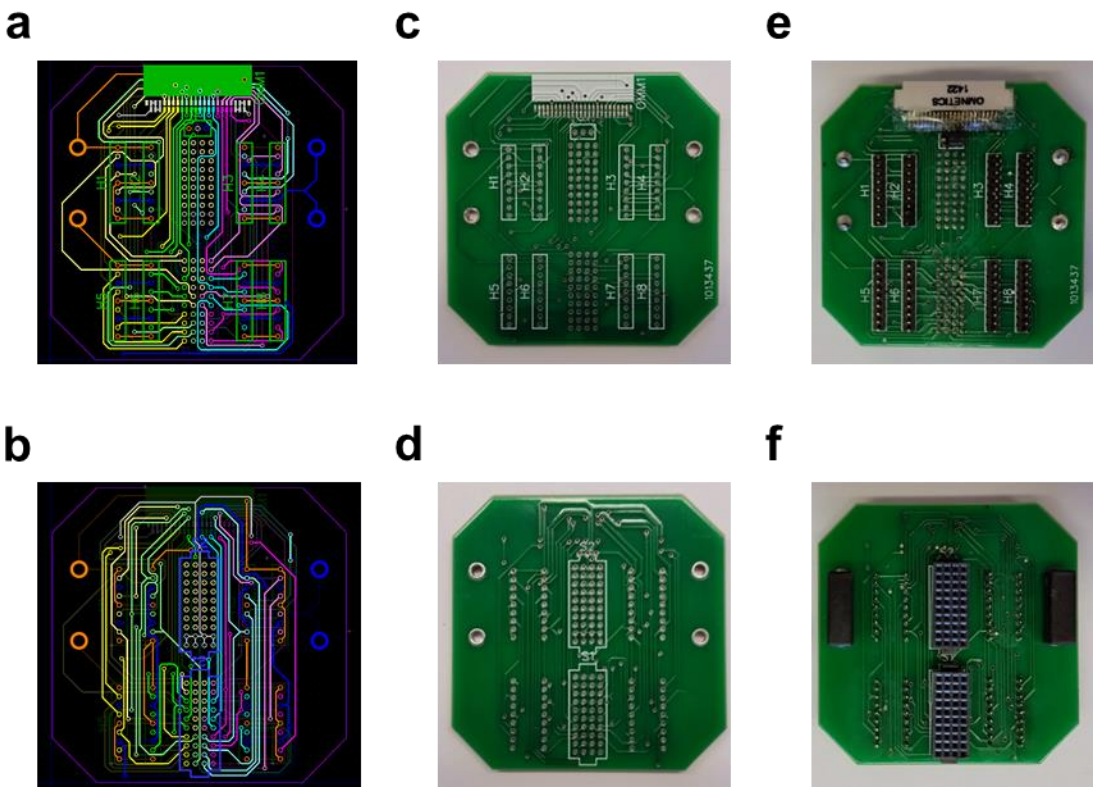

Figure 4-1 | Design and Assembly of Stimulator Board.
a-b, Schematic of the front and back of the stimulator board, prepared in DipTrace. Groups of colored wires indicate electrodes belonging to the same tetrode. The orange holes represent the contact points for one pole of the stimulator input, and the blue holes the contact points for the other pole. **c-d,** The front and back of the printed circuit board, before populating with components. **e-d,** The fully assembled circuit board, populated with the Omnetics connector on top, breakout headers on the front side, and interfacing headers and stimulator jacks on the back side.

Stimulator Design

All circuit design was performed in DipTrace, a free software suite for printed circuit board (PCB) design. A major design constraint was the overall size of the PCB; too large a board would add undue weight to the rat, as well make it more difficult to balance. Counteracting this design constraint is the need for all traces to be well separated and mapped in a way that is logical to the user.

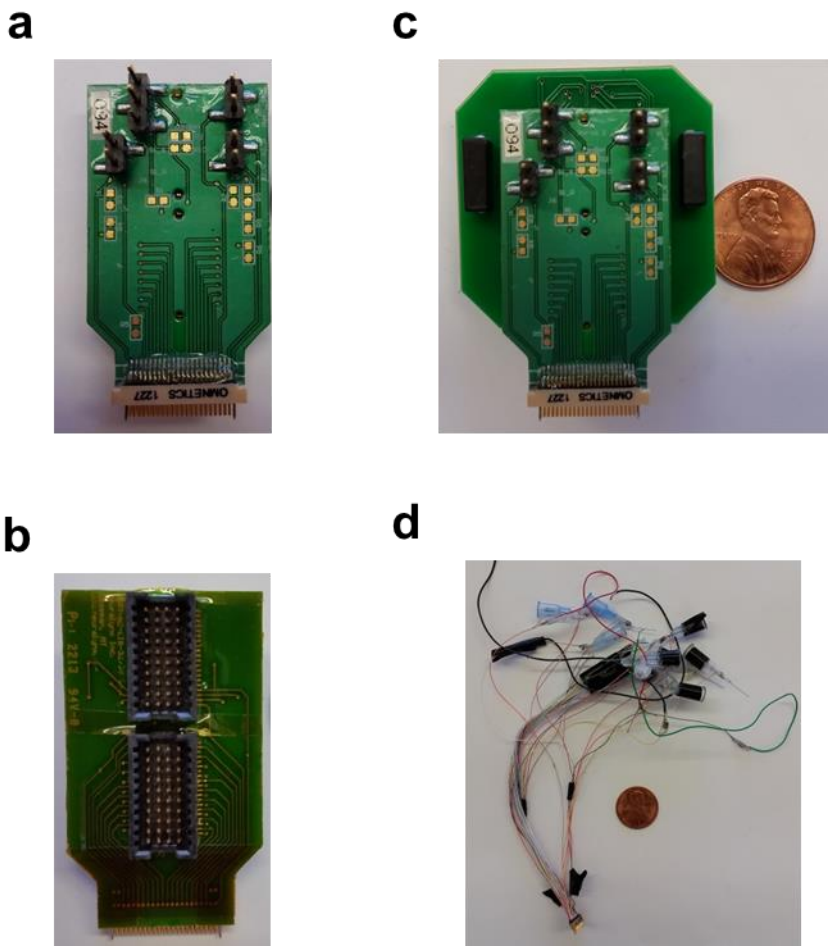

Figure 4-2 | Interfacing with the NanoZ Connector.
a-b, The front and back of the NanoZ connector, which interfaces directly with the headstage through the Omnetics connector on the bottom, and interfaces with the stimulator through the headers on the back. **c,** The fully assembled stimulator, with the NanoZ connector attached to the back of the stimulator board. Penny for scale. **d,** A previous, less streamlined, less modifiable iteration of the stimulator. Only pre-specified channels can be used for stimulation and recording, and several pins must be individually connected. This demonstrates the comparative ease of use of the stimulator board.

A schematic of the PCB is shown in Figure 4-1. The electrodes initially come through the Neuralynx adapter used for electroplating (Fig. 4-2). This connector has a standard header design, removing the need to procure a female Omnetics connector. Signals leave the PCB through a male Omnetics connector surface-mounted onto the PCB. The pre-amp plugs in to this connector just as if it were the original connector on the headstage.

Each channel is connected to its corresponding channel on the output end, as well as to a specific pin of a "breakout header." For ease of experimenter use, each tetrode has its own breakout header, consisting of 9 pins. Pins 2, 4, 6, and 8 are connected to channels 1, 2, 3, and 4, respectively, of the tetrode. Pins 1, 5, and 9 are connected to the positive pole of the stimulator input; pins 3 and 7 are connected to the negative pole of the stimulator input. Using 0.05" shunts, or "jumpers," an experimenter can thus connect any channel to either the positive or negative pole of the stimulator, leaving all other channels unaltered. A 3-pin header allows similar connectivity for the ground signal. The positive and negative poles of the simulator enter the PCB through jacks on each side of the PCB (Fig. 4-3).

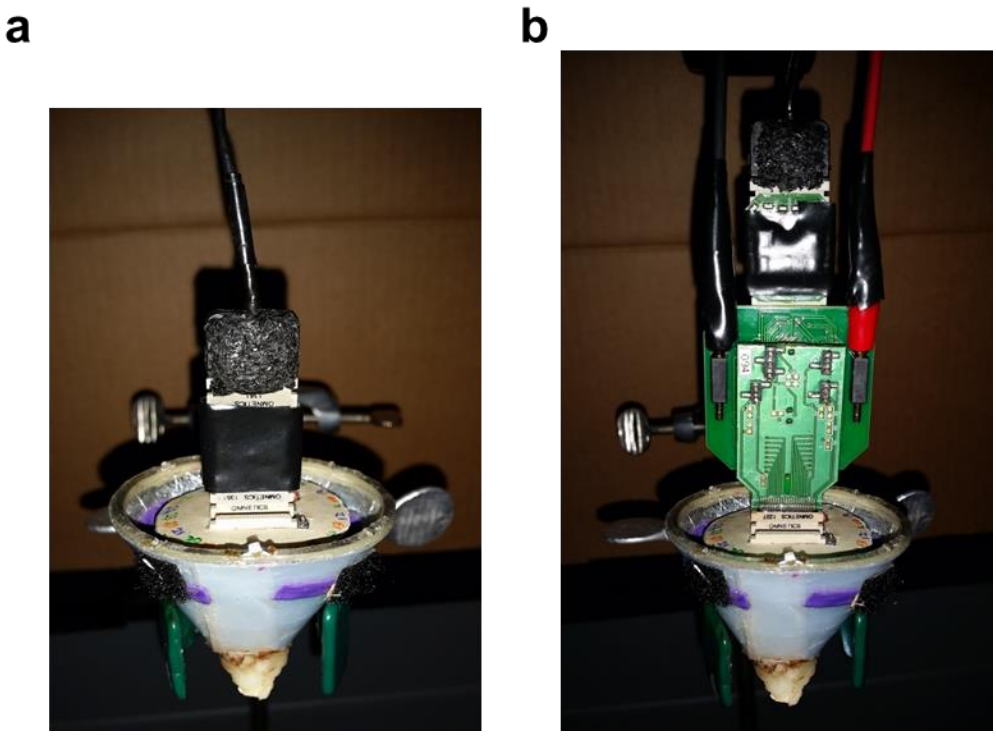

Figure 4-3 | Interface with the EIB and Pre-Amplifier.
a, The entire implanted cone-shaped drive typically interfaces through the headstage (middle, white) connection with the pre-amplifier (top, black). **b,** The stimulator board occupies a position between the headstage and pre-amplifier. The red and black wires are connected to the positive and negative poles, respectively, of the current source used for stimulation.

Thus, a current source can be connected to any two arbitrary channels. Current may be passed with positive or negative polarity from ground to any single channel, or current may be passed between two channels. This circuit has no complex circuit elements, active or passive. The only added resistance to the original connectivity is the resistance of the wire traces and of the contact points, a negligible amount that is not expected to interfere with signal properties in any substantial way. This also reduces the cost and labor necessary to produce the circuit. The final dimensions of the stimulator are 1.65 by 1.65 inches, with 210 holes and 77.54 inches of wiring. Printed on standard material, the PCB has a mass of 8.5 g. When coupled to the NanoZ connector the assembly has a total mass of 14.5 g. This is a substantial addition to the ~30 grams of the existing implant, but can be largely offset by the tension of the wires connecting to the stimulator.

Assembly and Cost

The board itself is cheap to manufacture. Five boards were ordered from Bay Area Circuits for a total of $30. Headers must be purchased and soldered to the through-holes on the PCB. The most expensive element is the male Omnetics connector, which must be custom-ordered from Omnetics or Neuralynx. This component can cost ~$100 and have a several week turnaround time. For the purposes of this prototype, we salvaged a connector from an old Neuralynx pre-amp. The Omnetics connector must be surface-mount soldered to the board. Due to the close spacing of the surface-mount pads, this requires a skilled and patient hand. In total, 10 hours of labor and ~$150 of materials are needed for a single stimulator circuit.

In comparison, Neuralynx sells a stimulator pre-amp. This product handles the switching of stimulator channels through software, allowing for more dynamic switching of the channels to be

stimulated. Undoubtedly this allows greater temporal control over stimulation protocols, but the functionality comes at a high price of $2000. For simple in-vivo stimulation experiments, the stimulator circuit described above is quite adequate, at a fraction of the cost.

Proof of Concept

Since the stimulator was manufactured, we have not had the opportunity to interact with any putative dendritic signals. As proof of concept, we have tested the circuit to ensure 1) Use of the stimulator does not alter signal properties; 2) That there is no cross-talk between channels; and 3) Current passed through the stimulator has an effect on neural activity.

To test that routing the signals through the stimulator does not have any effect on signal properties, we compared neural signals recorded with and without the stimulator (Fig. 4-4a). Signals were qualitatively the same, with extracellular spiking and lower-frequency fluctuations clearly visible. This was confirmed quantitatively by computing the power spectra of these signals (Fig. 4-4b), using identical methods as those described in Chapter 3. The power was nearly identical with or without the stimulator for all frequencies above 2 Hz. When recording with the stimulator extra power below 2 Hz was introduced, which may be due to amplification of movement artefacts. This is not anticipated to be a problem, as most oscillations of interest during movement are high frequency, the lowest being theta oscillations of 6-12 Hz. The biggest concern would be during slow-wave sleep, which has prominent oscillations in the 0.5-2 Hz range. But this is not a problem if the excess low frequency power comes from movement, as the rat will not be moving during sleep.

Next we tested if there was any evidence of cross-talk between channels of a tetrode introduced by the stimulator. As above, we recorded signals from all channels of a headstage with and

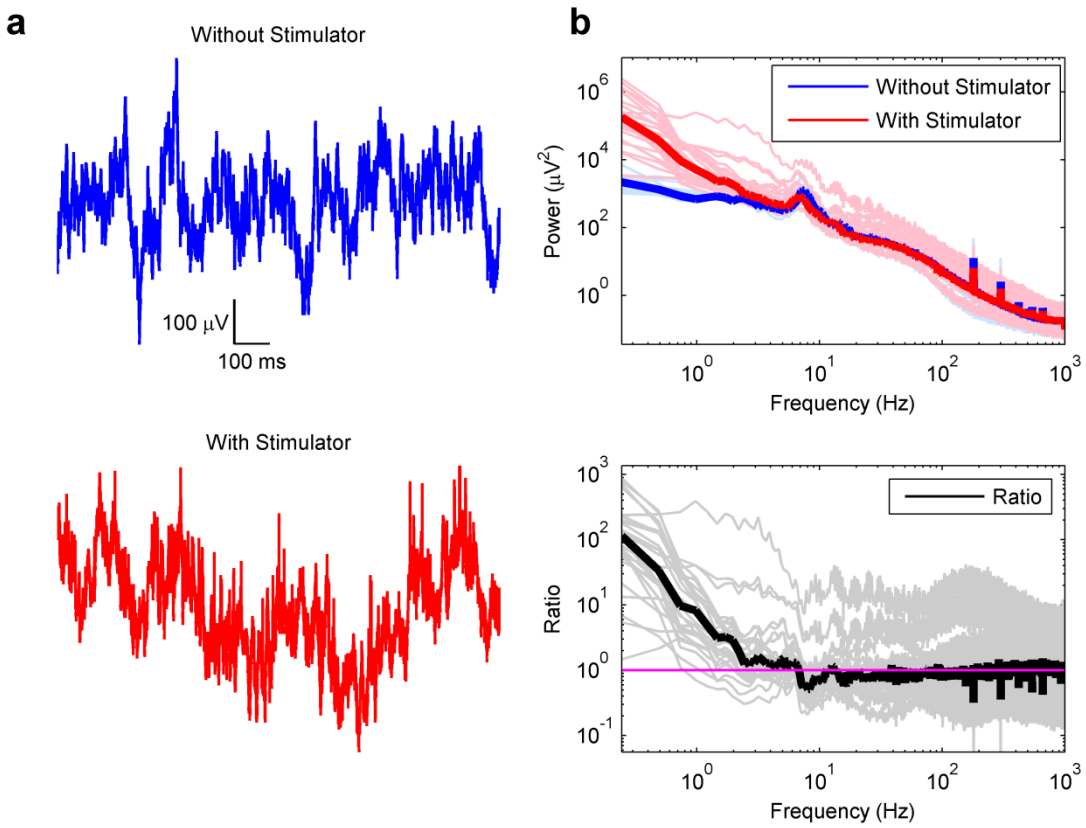

Figure 4-4 | Electrode Signals above 3 Hz are Unaffected by the Presence of the Stimulator
a, Top, sample 1.25 second-long LFP recording, obtained with the normal recording configuration (see Fig. 4-3a). Bottom, sample 1.25 second-long LFP recording from the same tetrode as above, but in the recording configuration with the stimulator between the headstage and the pre-amp (see Fig. 4-3b). No current was being passed through the stimulator during these measurements. **b,** Top, power spectra of individual channels (thin light traces) and the median power spectrum (thick dark traces). At frequencies above ~3 Hz, the power spectrum is nearly identical with or without the stimulator board in the circuit. Signals tend to have excess power in frequencies below 3 Hz in the presence of the stimulator board. This may be attributable to slow movement artefacts, as the board adds two more contact points to the circuit that could introduce noise from movement. Bottom, the ratio of the power spectra $P_{With}/P_{Without}$ further illustrates the above point. As above, thin light traces represent individual channels and the thick dark trace represents the median.

without the stimulator. For all 7 working tetrodes on the headstage, we computed the mean correlation coefficient of all 6 pairs of channels (1 vs 2, 1 vs 3, 1 vs 4, 2 vs 3, 3 vs 4). Without the stimulator, the correlation was high (0.96), as is expected for the 4 channels of a tetrode (Fig.

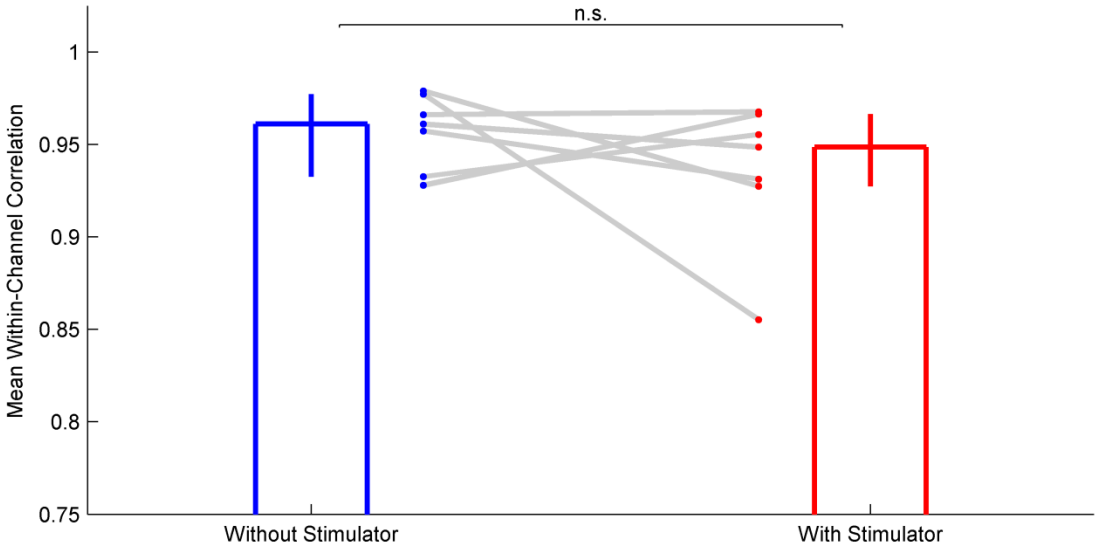

Figure 4-5 | No evidence of Cross-talk between Channels due to Stimulator
The within-channel correlation was computed by taking the mean of the correlation coefficients of all 6 possible pairs of channels on a tetrode. This correlation was not significantly different (p=0.26, Wilcoxon signed-rank test), without the stimulator in the circuit (0.96, [0.93, 0.98], n=7 tetrodes) or with the stimulator (0.95, [0.93, 0.97], n=7 tetrodes). No current was being passed through the stimulator during these measurements. These measurements were done on signals filtered above 10 Hz (4 pole Butterworth filter) to minimize movement artifacts.

4-5). The correlation was not significantly different (p=0.26) when recorded through the stimulator (0.95), thus demonstrating that the stimulator does not introduce cross-talk between the channels.

Finally, we demonstrated that current passed through the stimulator affects local neural activity. We passed current between one channel of a tetrode and animal ground, with positive polarity indicating current flow towards animal ground. We tested three different levels of current, +200 nA, -200 nA, and -1000 nA (Fig. 4-6). The stimulation protocol was 10 pulses of approximately 200 ms, delivered at a rate of 1.1 Hz. We quantified the spontaneous multiunit firing rate in the 200 ms before stimulation and compared it to the firing rate during the 200 ms of stimulation.

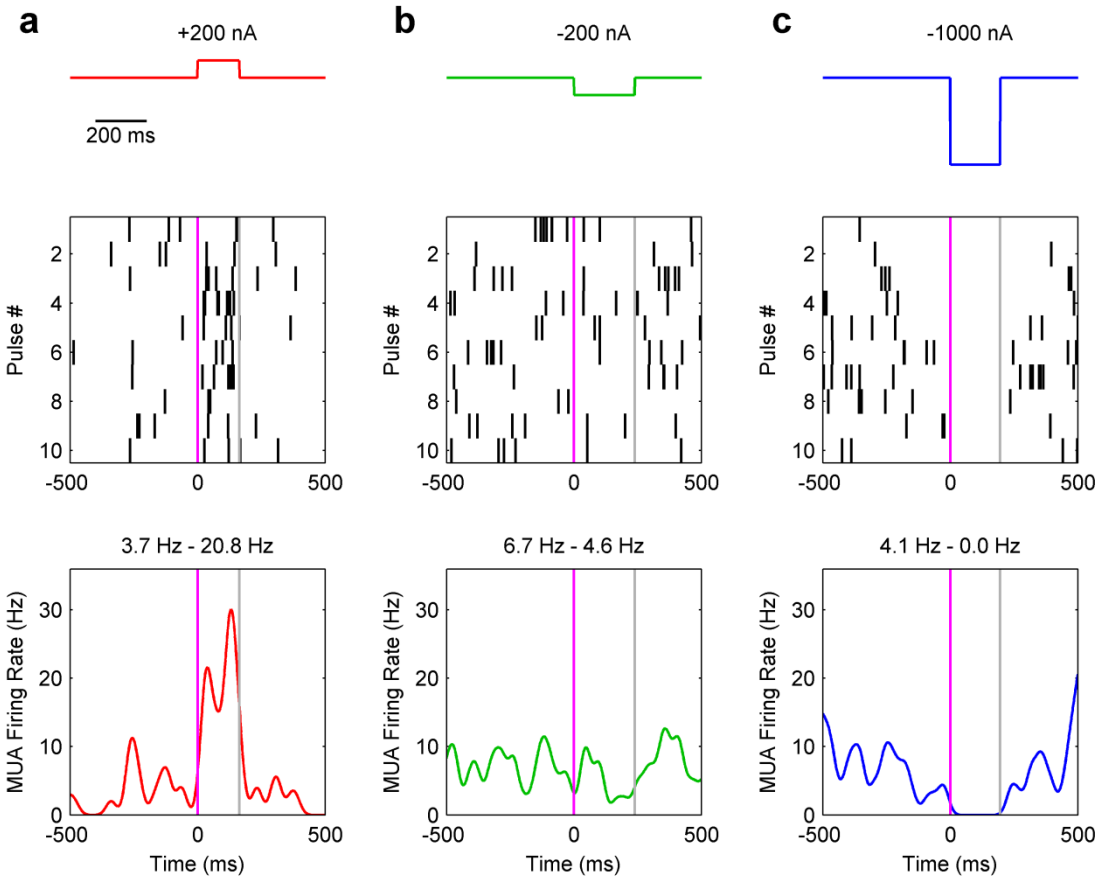

Figure 4-6 | Stimulation Modulates Multiunit Firing Rate
a, Top, stimulation protocol. Current was passed between one channel of a tetrode and animal ground, and multiunit spiking was recorded on that tetrode. A ~200ms pulse was delivered 10 times at a frequency of ~1.1 Hz. Current in this experiment was +200 nA when the stimulator was on, and 0 at all other times. Middle, raster plot of multiunit spiking. The time of stimulation onset is marked by the magenta line at 0 ms. The offset of stimulation is marked by the gray line. Each row represents one stimulation pulse, and each tick mark represents a single action potential. +200 nA reliably elicited spiking, with little effect after stimulation. Bottom, firing rate plot of the raster plot above. The firing rate in the 200 ms before stimulation was 3.7 Hz, and the firing rate during the 200 ms of stimulation was substantially increased to 20.8 Hz. **b,** Same as in **a**, but with a stimulation current of -200 nA. Multiunit firing is only mildly affected by this stimulation protocol, reducing to 4.6 Hz from 6.7 Hz. **c,** Same as in **a** and **b**, but with a stimulation current of -1000 nA. This protocol completely shuts down all spiking on this tetrode.

A stimulation current of +200 nA had a large effect on firing, increasing the local firing rate from 3.7 Hz to 20.8 Hz, more than five-fold higher (Fig. 4-6, left). This was not simply a response to current being passed through the brain, as a stimulation current of -200 nA did not have an

appreciable effect on firing rate, decreasing it from 6.7 Hz to 4.6 Hz (Fig. 4-6, middle). Finally, we were able to temporarily silence local spiking completely by stimulating with a current of -1000 nA. Multiunit activity dropped from 4.1 Hz to 0 Hz during this stimulation, and resumed as soon as the current pulse ended (Fig. 4-6, right). These experiments demonstrate that passing current through a single tetrode with this stimulation board can affect local spiking activity in a reliable, predictable, and graded manner. This will be an invaluable tool in the future, allowing us to obtain more direct verification of the dendritic nature of our recordings.

Tetrode Plating Protocols

A natural question that may arise from our dendritic recordings is why we see these recordings and no other lab has reported them. In light of our glial sheath hypothesis, we suspected that there may be something peculiar about the way our tetrodes are prepared that makes them more likely to elicit the specific type of immune response that we believe facilitates recording of dendritic membrane potentials. Our tetrodes are made of a widely used standard Nickel-Chromium alloy, so the type of electrode is unlikely to be a determining factor. The final step in preparing tetrodes before implantation is electroplating the wire tips to decrease impedance. Electroplating has many variables that can differ from lab to lab, so we made some systematic manipulations of these parameters and observed the morphology of the plating structure. The structure of plating may be important because certain sizes of protrusions may appear more or less attractive to glia.

We tested two main plating procedures. The first was a slow plating, with 150 nA of current passed for 2 seconds, repeated until the impedance at 1 kHz was below 130 kΩ. The second

procedure was a fast plating, with 1000 nA of current passed for 2 seconds, repeated until the impedance at 1 kHz was below 250 kΩ.

In both protocols, one cycle was defined as one plating duration of each channel of a tetrode, followed by an impedance check. During plating, gold particles are attracted to the electrode being plated from any source. Most of this comes from the surrounding plating solution, but some may also come from gold already plated onto neighboring electrodes. Thus, if one electrode is plated down to threshold before another starts plating, the second channel may "steal" some gold from the first channel, effectively de-plating the first channel. Cycling through channels is done to mitigate this phenomenon.

Tip morphology was qualitatively different when using the different plating procedures. Under 1000x optical magnification, electrodes plated with the low-current method had smooth, orderly, conical plating (Fig. 4-7a). Electrodes plated with the high-current method had tips that looked more chaotic and spindly, with large coral-like structures of gold plating extending away from the electrode tip (Fig. 4-7b). This is likely due to the propensity of electroplated material to aggregate near corners. Because fewer plating steps are needed to complete this process, any imperfections would not have time to be smoothed over.

Additional magnification through use of a scanning electron microscope (SEM) corroborated these findings. Electrode tips plated with the low-current method showed small spheres of gold, with a fine cauliflower-like texture (Fig. 4-8a, b). In contrast, electrodes plated with the high-current method contained much larger spheres of gold particles (Fig. 4-8c, d) as well as a certain degree of scale-like regions of plating, absent in the low-current samples.

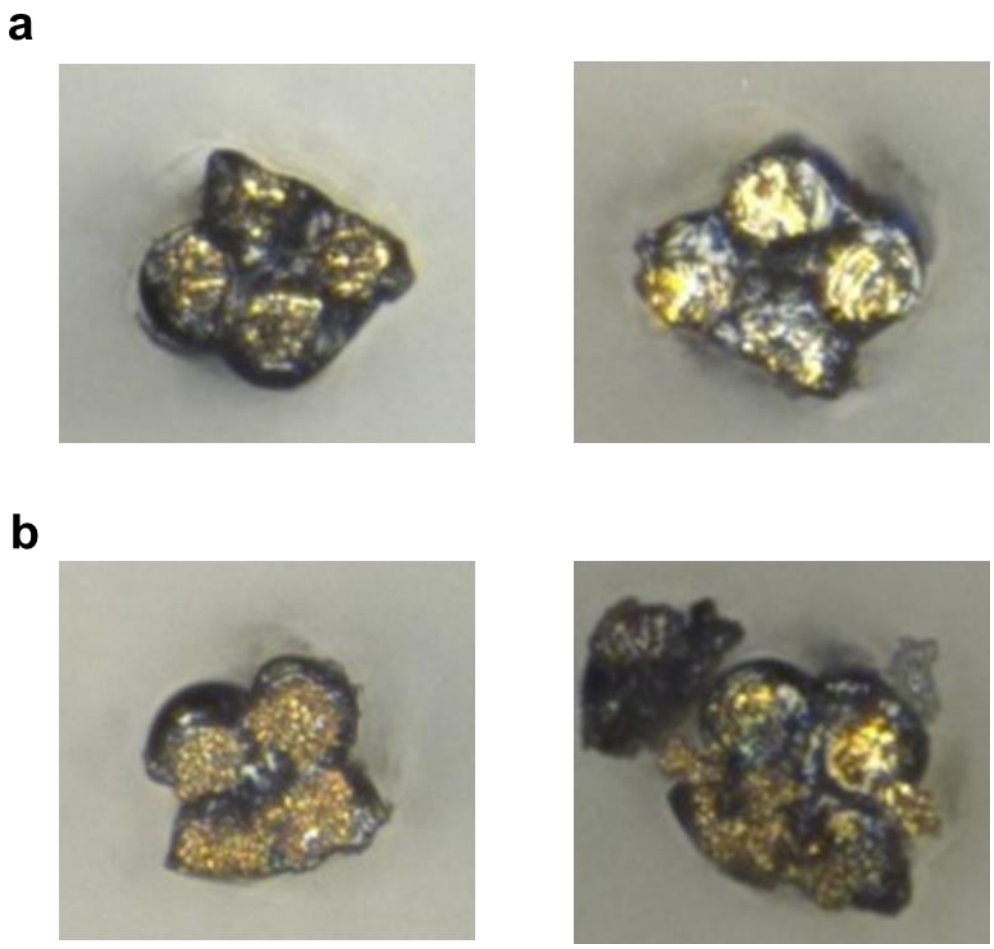

Figure 4-7 | Optical Characterization of Tetrodes with Different Plating Procedures
a, Two examples of tetrodes plated using the low-current method, under 1000x optical magnification. Entire view window is ~80 µm square. 4 individual tetrode tips are visible with smooth, cone-like gold tips. **b,** Same as in **a** but for two tetrodes plated using the high current method. The gold-covered tips are more corrugated (left) and occasionally form plumes of coral-like structures (right). Entire view window is ~80 µm square.

During the time period over which these manipulations were made, very few dendritic membrane potentials were recorded. It is therefore impossible to make a conclusive statement about which plating method is best for achieving dendritic recordings. Both methods result in usable extracellular recordings, though the stability and useful lifetime may differ between the two.

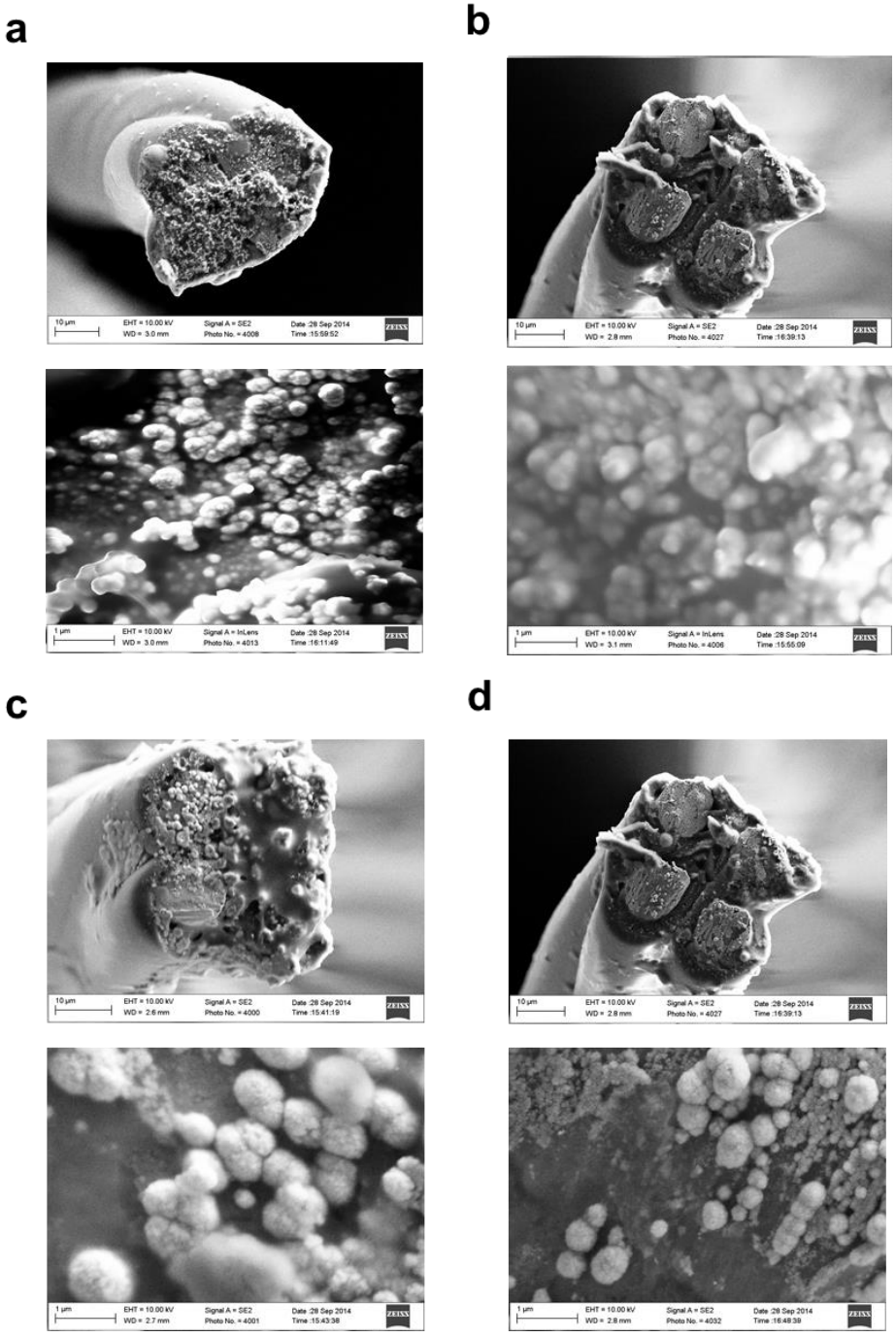

Figure 4-8 | SEM Characterization of Tetrodes with Different Plating Procedures
a-b, Two examples of tetrodes plated using the low-current method, under 1000x magnification (top) and 10,000x magnification (bottom) in a Zeiss Scanning Electron Microscope. Tetrode tips are covered with small (100-400 nm diameter) spheres of gold particles. **c-d,** Same as in **a-b** but for two tetrodes plated using the high current method. The gold-covered tips have large (~1 µm diameter) spheres of gold particles, in contrast to the tetrodes prepared with the low-current procedure.

It is possible that different plating procedures would yield more extreme modifications in the electrode tip geometry that could facilitate more dendritic recordings. Unfortunately, the parameter space is very large and multidimensional. Such parameters include, but are certainly not limited to, total impedance, plating time, plating current, composition of the plating solution, and relative positioning of the plating cathode to the electrode tips. These implants are also very time-consuming to make and implant, and the typical time period in which dendritic recordings are achieved is 1 month after implantation, slowing down the time between manipulations and observations of results. Finally, even a doubling of the "hit rate" of these tetrodes would be difficult to detect without a large sample size. If, on average, 2 of every 24 tetrodes records a membrane potential signal, and only one manipulation is done per rat, then it is possible that tens of rats must be used to observe statistically significant effects. A more fundamental understanding of the process that leads to the glial encapsulation will be needed before the high-dimensional parameter space of electroplating is explored for the purposes of in-vivo dendritic membrane potential recording. The potential insights gained from such recordings, however, certainly justify such an effort.

5. Hippocampal somatic activity during random exploration in virtual reality

Generalized Linear Model to Separate Multiple Determinants of Firing

Typically, neuronal responses are characterized by their modulation by a single parameter, be it orientation tuning in visual cortex[95], frequency tuning in auditory cortex[96], or spatial tuning in CA1[4–6]. If one is to look for additional parameters that modulate these neurons, in independent or joint ways, great care must be given to identify and eliminate the effect of one variable on the other one, particularly if the entire joint stimulus space is not adequately sampled.

This line of analysis is especially relevant for analyzing hippocampal pyramidal cells, which typically are active in only one particular region of an environment[4–6]. Because hippocampal cells are heavily modulated by visual cues, it is desirable to investigate the modulation of hippocampal activity by head angle; this directional tuning is traditionally thought to only be present in 1-dimensional tracks and not 2 dimensional tracks[6,26], though "place-by-direction" cells have been reported in nearby presubiculum and parasubiculum[97]. This is a non-trivial task, as these cells are already heavily modulated by position; hence estimates of angular tuning may be incorrect or biased[14,26,27]. Recording sessions are also of finite duration, so it is an unreasonable expectation to have equivalent behavioral coverage of every head angle at every position. This is particularly true at the edge of the recording environment, where the rat cannot physically move through certain positions at certain heading angles. This leads to a certain degree of "behavioral bias," which can interfere with measures of selectivity using traditional binning methods[26,28].

The use of a Generalized Linear Model (GLM)[98–101] offers an attractive alternative to traditional binning methods, though this method has not yet enjoyed widespread adoption by the neuroscience field. Briefly, given a temporal profile of the spike train of a given neuron and specified basis functions for the parameters of interest, coefficients to these basis functions are fit to produce a time-varying firing rate that best explains the data. The weighted basis vectors can then be used to reconstruct a selectivity map for their respective parameters, ideally identifying the most likely modulation of the spike train by each of the parameters. By using this method, we were able to show that a substantial percentage of hippocampal neurons are modulated by head angle, not just in RW environments but also in VR[37].

With the power of new techniques comes the burden of proving their effectiveness, that they do what they are supposed to do and do not introduce spurious correlations or other artifacts. This chapter describes the efforts to validate the GLM framework for our hippocampal data, as well as identifying unexpected parameters that can affect measures of spatial and angular selectivity.

Generation of surrogate data to validate the GLM method

Non-parametric generation of simulated place fields

To estimate the amount of angular modulation behavioral biases introduce into purely spatially modulated neurons, we generated surrogate data based on the firing rate maps of recorded neurons. Given a behavioral profile $B(t) = \left(B_X(t), B_Y(t)\right)$ and spatial firing rate map $F(X, Y)$, spike times were generated according to an inhomogeneous Poisson process with $F\left(B(t)\right)$ as the rate parameter. Data generated in this manner were used in Fig. 5-3.

Parametric generation of simulated place fields

The methods were identical to those described previously[37]. To verify the GLM framework accurately estimated the independent contribution of spatial and angular factors in determining spiking, we generated surrogate data with predetermined and variable degrees of spatial and angular modulation. For a surrogate place field centered at $(\bar{x}, \bar{y})$, with spatial variance σ_{XY} , preferred angular orientation $\bar{\varphi}$ and angular variance σ_{φ}, the relative probability of firing for any (X, Y, φ) combination was defined as:

$$p(X, Y, \varphi) = P_{XY}(X, Y) \times P_{\varphi}(\varphi) \quad (12)$$

$$P_{XY}(X, Y) = p_{XY}(X, Y) - min\big(p_{XY}(X, Y)\big) \quad (13)$$

$$p_{XY}(X, Y) = e^{-\frac{D_{XY}}{\sigma_{XY}}} \qquad D_{XY} = \sqrt{(X - \bar{x})^2 + (Y - \bar{y})^2} \quad (14)$$

$$P_{\varphi}(\varphi) = p_{\varphi}(\varphi) - min\left(p_{\varphi}(\varphi)\right) \quad (15)$$

$$p_{\varphi}(\varphi) = e^{-\frac{D_{\varphi}}{\sigma_{\varphi}}} \qquad D_{\varphi} = angle\big(e^{i(\varphi - \bar{\varphi})}\big)^2 \quad (16)$$

Where i is the imaginary number $\sqrt{-1}$.

Given a behavioral profile $B(t) = (B_X(t), B_Y(t), B_{\varphi}(t))$ and desired mean firing rate μ, the absolute probability of firing is obtained by scaling the relative probability of firing (equation 12) by a constant factor k:

$$P(X, Y, \varphi) = k * p(X, Y, \varphi) \quad (17)$$

$$k = \frac{\mu}{E}, \qquad E = \int_{t=t_0}^{T} p(B(t))\, dt \quad (18)$$

Where t_0 indicates the start time of the session, and T indicates the end time of the session.

Spike times are then generated according to an inhomogeneous Poisson process with $P\big(B(t)\big)$ as the rate parameter. Surrogate data generated in this manner were used in Extended Data Fig. 5-3a–h.

GLM Specifics

Two specifics about the output of the GLM are worth describing in detail, one a potential problem and one a helpful feature.

Spuriously High Pixels

First, although the GLM is more robust to behavioral undersampling than binning methods[37], it still requires an adequate amount of data to arrive at interpretable results. In several sample cells, the GLM arrives at a spatial map with a few bins on the periphery of the table with large values. These bins may have values several orders of magnitude larger than the rest of the otherwise orderly map (Fig. 5-1). This often arises due to over-fitting of a burst of spikes that occurred during a single visit to that bin or to adjacent bins. Because the GLM includes an exponentiation in its calculation, spuriously high bins can be amplified to extremely high values. In our dataset approximately 20% of cells encounter this problem.

This over-fitting can come about from using too high a spatial order when fitting. In our hands, we allow the number of basis functions to vary and choose the "best model" using Bayes' Information Criterion (BIC)[102], which attempts to balance the number of parameters of the model with the goodness of fit. When there are large bins, the GLM tends to use a large number of

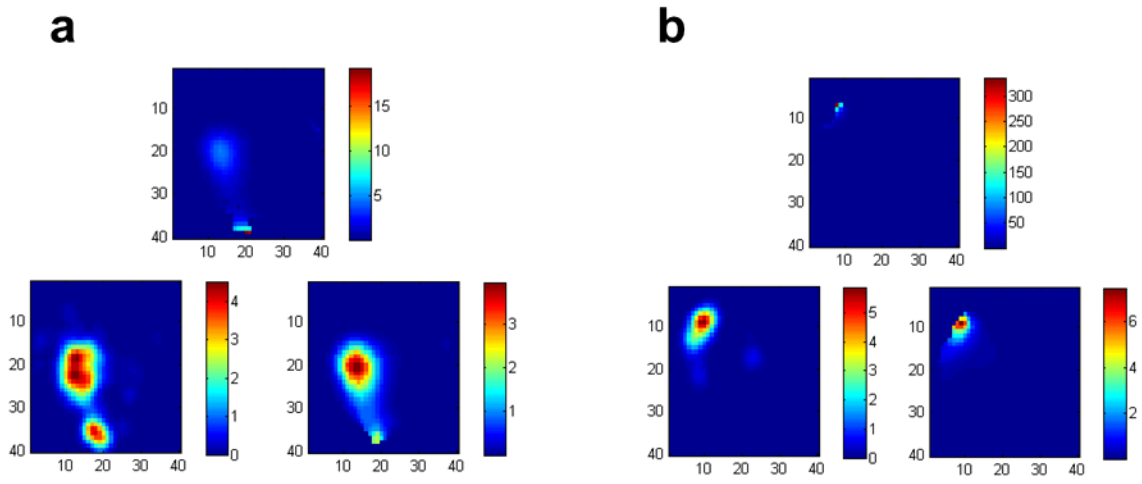

Figure 5-1 | Fixing Spuriously High Pixels in the GLM Output.
a, Top, example spatial rate map produced by the GLM. Note that only a restricted set of pixels near the bottom of the map have high values above 15 Hz, whereas the rest of the map has low values. Bottom left, the same unit's spatial firing rate when computed with the binned method, which in this case is likely closer to the "true" rate map. Bottom right, the original GLM rate map (top) passed through a 2-dimensional median filter. Note the spurious high pixels are gone, and the rate map has a more natural-looking topography. **b,** Same as **a** but for a different unit. Note that the original map has a peak firing rate of 300 Hz, where the corrected maps have a peak rate around 6 Hz.

spatial orders. Evidently in these cases with spuriously high bins, the goodness of fit gained by introducing more parameters exceeds the punishment of having a more complex model. A simple solution might be to limit the number of allowed spatial basis functions, but this could negatively impact cells with bona fide sharp spatial tuning. A combination of 4 other solutions serves as an effective check against this phenomenon.

First, bins with very limited spiking can be excluded from the final map. This fixes matters cosmetically, but the underlying fit would still be influenced by those bins and may not ultimately be useful. Second, single spurious bins can be removed by passing the map through a 2-dimensional median filter (Fig. 5-1). Isolated bins on the edge of the map are removed through this method, but several maps contain small groups of high bins. Third, before the GLM

computes its coefficients, spikes in regions without adequate behavioral sampling can be removed. However, not all spurious bins can be removed before spikes begin to be removed from the middle of the table where there is "good enough" sampling. Finally, a modification to the selection criteria can be used. In addition to considering the goodness of fit and number of model parameters, the dispersion of the resulting map can be factored in. This would punish maps with a few high-value bins away from the rest of the (presumably correct) high value bins, independent of the number of spatial basis functions. Thus, cells with maps that are actually sharply tuned will not be punished, as all high rate bins will be located close to each other.

Implementing the above adjustments to the algorithm reduces the number of anomalous maps to ~5%, which should be acceptable to discard without reducing the number of sample cells.

Independence of Number of Bins on Reconstruction

When using traditional binning methods, great care must be taken to choose the correct number and size of bins to ensure results are not spurious. When reporting the modulation of firing obtained by the GLM, the number and size of bins must also be chosen to reconstruct the map. Fortunately, this is less of a critical decision with the GLM, provided the bins are not so coarse as to mask important fluctuations.

Binning methods arrive at a non-parametric representation of firing rates; values are entirely empirically derived, with no governing equation or distribution. In contrast, the GLM estimate is fully parametrized. This parametrization is performed when choosing the basis functions; the results of the GLM are simply coefficients of those basis functions. Hence, the underlying "tuning curve" is a function defined in continuous parameter space. When reconstructing the map, we simply evaluate that function at specified locations to obtain values. The overall

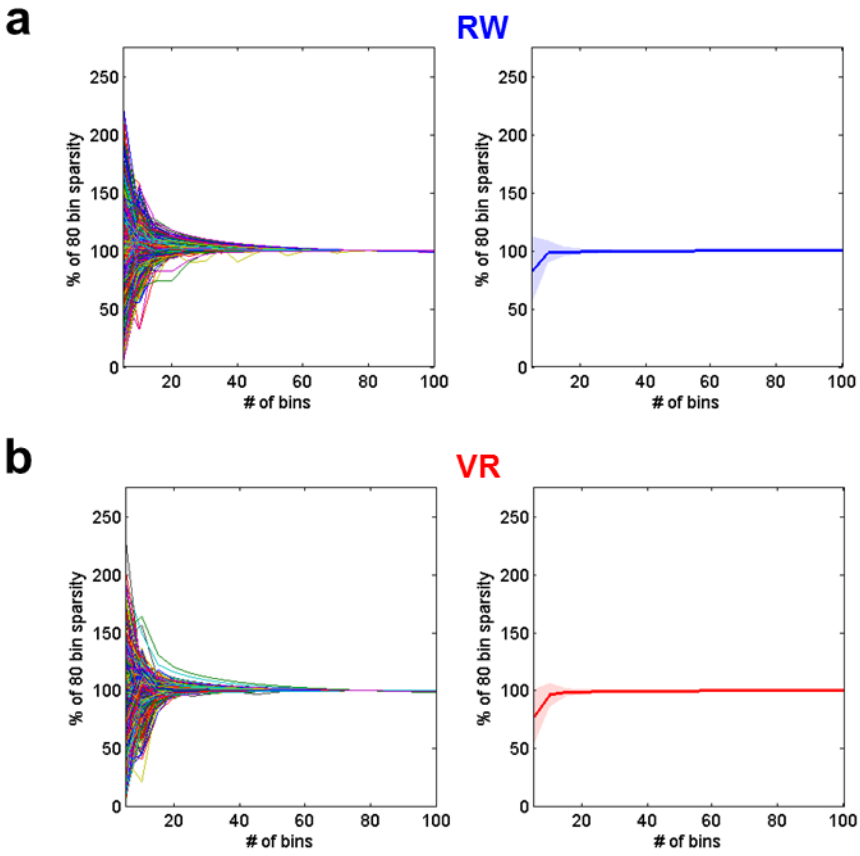

Figure 5-2 | GLM-Derived Sparsity is Unaffected by the number of Bins used for Reconstruction. **a,** Left, the angular sparsity of individual RW units as a function of the number of bins used to reconstruct the angular tuning map. Values are expressed as a percentage of the sparsity obtained with 80 bins. Each line represents a different unit. Right, the median (solid blue line) with the 25th and 75th percentile (shaded region) for the population on the left shows the sparsity converges to a stable value with approximately 20 bins. Using additional bins for reconstruction do not impact the calculated sparsity, and will only serve to present a smoother angular tuning map. **b,** Same as **a** but for individual VR units. Like the RW units, an adequate estimate of the angular sparsity can be obtained with a minimum of 20 bins.

selectivity of tuning, then, should not be influenced by the number of bins used to reconstruct the tuning curve.

These theoretical conclusions are corroborated by the following empirical demonstration. Angular modulation of cells in both RW and VR were computed using the GLM. The angular maps were then reconstructed using a variable number of bins, from 5 to 100 bins (Fig. 5-2), and

the resulting sparsity was normalized to the sparsity obtained when 80 bins are used. Reconstruction with a small number of bins (<10) revealed that some units showed large differences with the sparsity calculated from 80 bins; though on average, the difference was not large (80% of max). Once more than 20 bins were used, there was no appreciable difference in angular sparsity. This held true for cells in RW and VR. These results demonstrate one of the beautiful advantages of GLM over binning. Once the GLM arrives at an answer y = f(x), the value of y can be evaluated at any value of x, no matter how close or far away the values of x are, or even if they are non-uniformly spaced.

Surrogate Data

As an illustration of the power of the GLM method, we considered a single example cell, generated according to the non-parametric method described above (Fig. 5-3a). The spikes from this cell were purely spatially modulated, with spikes equally likely to fire in a given position at any head angle. This is represented by the light blue circle below the rate map. The angular tuning for this cell was computed using both the binning method and the GLM. Due to a significant amount of behavioral bias, the binning method incorrectly assigned a high degree of angular sparsity to this neuron. The GLM correctly concluded that no angular selectivity was present; the spatial factors were able to explain all of the spiking.

This example was then extended to multiple cells. Surrogate data was generated as described above, and the accuracy of the GLM was compared with the accuracy of the binned method in a number of situations. First, spiking data from RW were generated according to the non-parametric method described above. Angular sparsity as reported by the GLM was close to 0 and significantly less than that reported by the binning method, demonstrating the accuracy of the

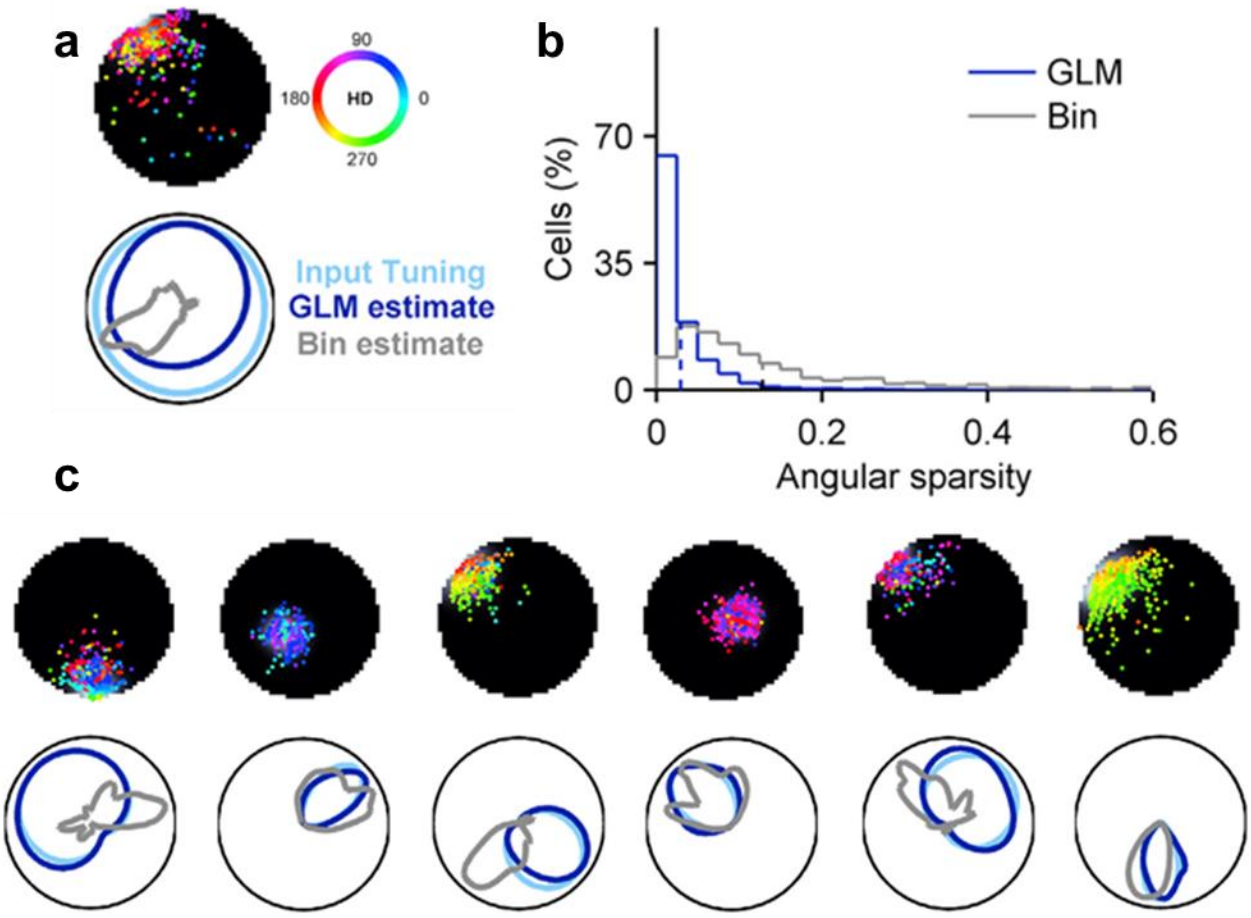

Figure 5-3 | Generation of Surrogate Data to Validate the GLM.
a, Top, Spatial firing rate of a simulated place field (grayscale) overlaid with colored dots indicating the position at which spikes occurred. Each color represents a distinct head direction as shown in the color wheel to the right. Bottom, The angular part of the input function used for generating the simulated place field was uniform and had no head-directional modulation (light blue). The head-directional firing rate obtained by using the binning method (gray) exhibited very sharp tuning, due to high behavioral bias at the edge of the platform resulting in a non-uniform sampling of the angles. In contrast, the GLM based rate (dark blue) followed the input function closely (showing no head-directional modulation). **b,** Surrogate data were generated for all place cells recorded in RW with spatial modulation similar to that in experimental data but with no angular modulation, according to the non-parametric method (see Methods). Sparsity of the angular ratemaps obtained using the GLM method was close to zero (0.03 ± 0.00, n = 1066; mean ± s.e.m.) and significantly ($p = 2.9 \times 10^{-201}$, Wilcoxon rank-sum test) smaller (4-fold) than that computed using the binning method (0.13 ± 0.00; mean ± s.e.m.). Thus, the binning method substantially overestimates the degree of angular modulation of spatially modulated cells, which the GLM method avoids. **c,** Several examples of simulated units constructed using a hybrid approach of the parametric and non-parametric methods. Spatial modulation is taken directly from RW place cells, and different widths and directions of angular tuning were put in by hand. In all cases, the GLM estimate more closely approximated the input angular tuning, unaffected by behavioral biases, unlike the binned method.

GLM under this extreme condition (Fig. 5-3b). We also used a hybrid approach of the two methods of generating surrogate data, taking the original spatial rate map of neurons and adding a parametrically generated angular modulation. In all cases, the GLM estimate of the angular tuning was more similar to the designed angular tuning than the binned estimate (Fig. 5-3c). Firstly, this demonstrates the validity of the methods used to generate surrogate data. Additionally, these experiments illustrate the advantage of the GLM method over the binning method in estimating angular modulation.

Confounding Factors

Behavioral Bias

As stated above, recording during random foraging tasks can introduce a "behavioral bias" in the joint parameter space sampled. Some of this bias is physically constrained; a rat at the north end of the recording chamber cannot move north, and so rarely faces north at that position. The bias can also arise from the behavioral idiosyncrasies of rats. In our data, we often observe that rats have a preferred direction of turning in both RW and VR, such that they prefer turning left over turning right, or vice versa. This turning preference, in combination with the unguided nature of the random foraging task, can lead rats to take a circular path around the environment, resulting in a fairly narrow distribution of head angles sampled at any given location.

Behavioral bias can be defined in two different ways, global bias and local bias. Global bias is defined as follows: For every spatial bin, the distribution of head angles is computed, and the sparsity of that angular distribution is assigned to that bin. The global behavioral bias is defined as the mean of all bins. This average may also be weighted by the total occupancy time in each

bin. The resulting measure is assigned to the entire recording session and all units recorded in that session, and serves as a general measure of how stereotyped the rat's behavior is.

Local behavioral bias is computed on a unit-by-unit basis. As before, the angular sparsity is computed for each spatial bin. The total number of spikes a given unit fired in each bin is also computed and used to weight the average of the global map. The number of spikes is used as weighting because the original map is weighted by time spent in each bin, measured in seconds. If we multiply by the firing rate, in spikes/second, the time cancels out and we are left with the number of spikes. This measure captures the behavioral bias that is most relevant for each

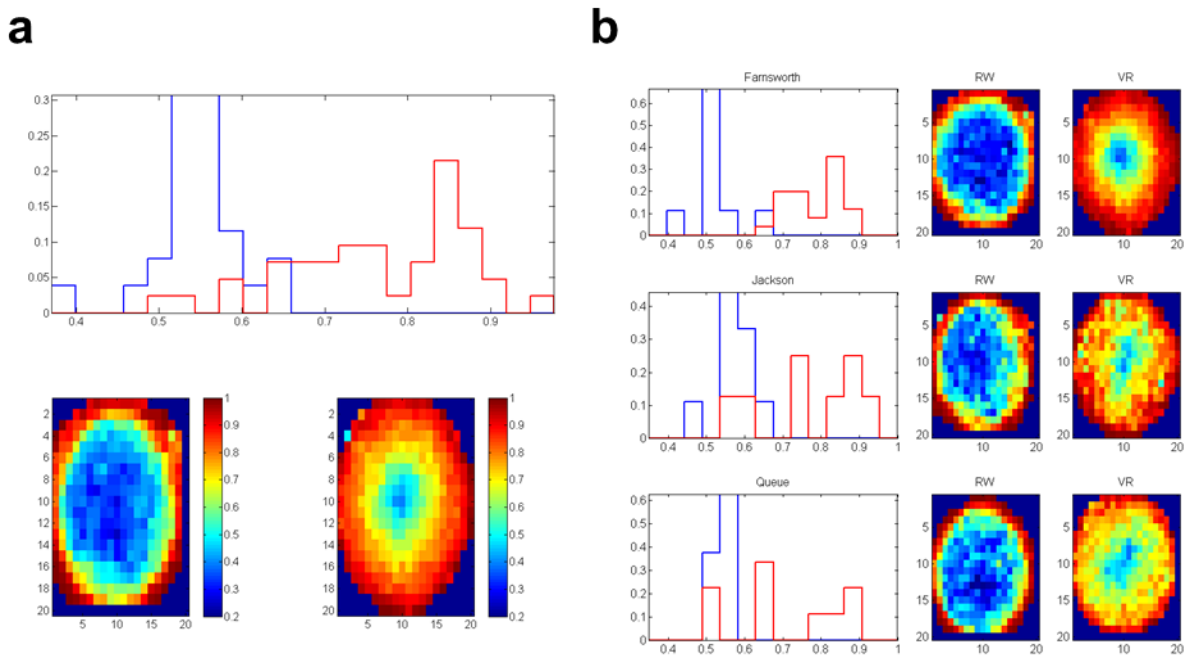

Figure 5-4 | Global Behavioral Biases.
a, Top, average behavioral bias maps for all sessions run in RW (left) and VR (right). Each pixel's value indicates the sparsity of angular occupancy in that bin. A value of 0 means that all angles were evenly sampled and a value of 1 means that only one head direction was sampled at that position. In both environments, behavioral bias is high at the edges, but this bias extends farther into the middle of the environment in VR compared to RW. Bottom, the average global behavioral bias was higher in VR sessions (red) than in RW sessions (blue). **b,** Same as in **a**, but for individual rats. All three rats show the same pattern as the aggregate data in **a**, with higher behavioral bias in VR compared to RW.

particular neuron, uninfluenced by behavior in a region of the environment that it does not fire in. Figure 5-4a shows averaged behavioral bias maps in RW and VR random foraging experiments. Rat behavioral bias was clearly more stereotyped in VR, and the global behavioral bias was significantly higher for VR sessions than RW. This was true for individual rats as well, showing that the results were not due to individual differences (Fig. 5-4b).

The fact that there exists a significant difference between behavioral bias in RW and VR means that any other statistical difference between neurons in either condition may be attributable to this difference. Indeed, plotting angular sparsity or mean vector length (MVL) against either global behavioral bias (Fig. 5-5a) or local behavioral bias (Fig. 5-5b) showed a significant correlation between the two. Thus, a potentially important difference between RW and VR, that there is better angular tuning in VR compared to RW, could potentially be explained away by differences in behavioral bias. Methods to address this confound are discussed below (Mitigation of Spurious Correlations).

Firing Rate and Number of Spikes

Two additional differences between RW and VR data present themselves as potential hurdles in data analysis. First, neurons tend to have higher mean firing rates in RW compared to VR[34,36]. Compounding this issue, VR recording sessions are often of shorter duration, and so the total number of spikes contributing to the tuning of a VR cell is smaller. Theoretically, neither of these should affect the angular sparsity, as they would both be expected to scale the rate map by a constant factor, and the sparsity measure is invariant to constant scaling. In practice, this is not the case.

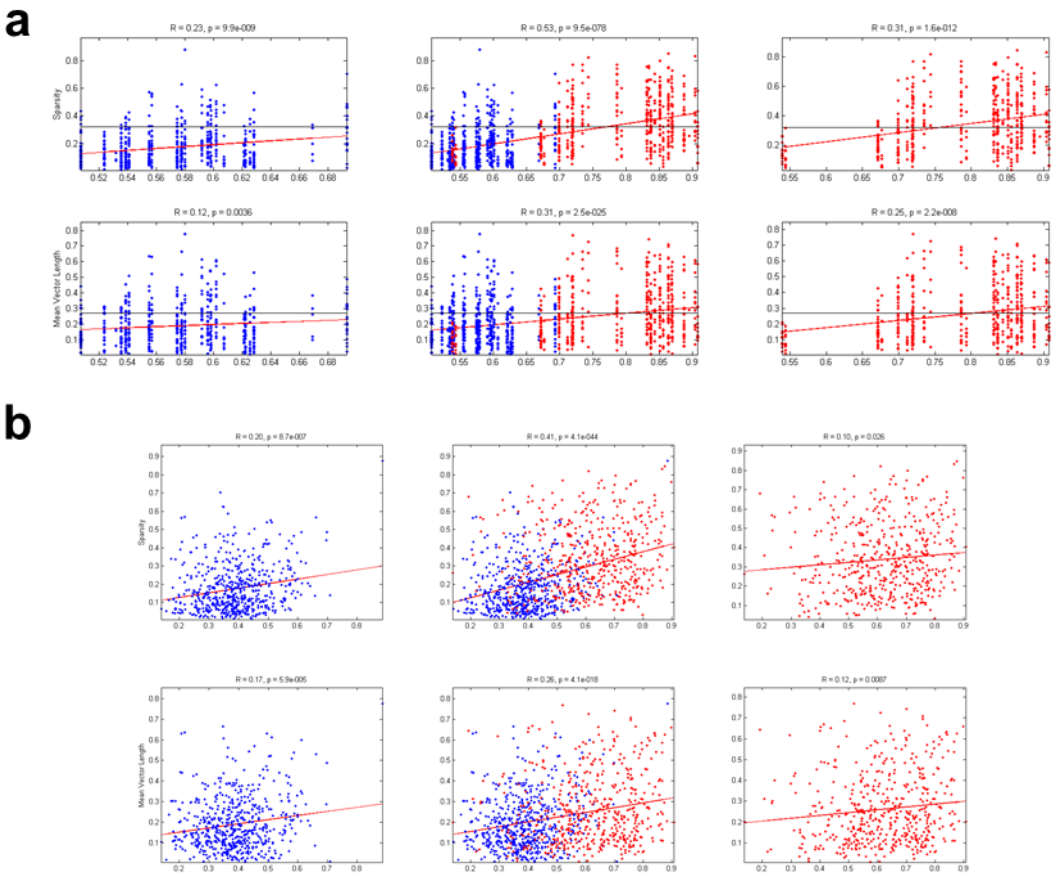

Figure 5-5 | Effect of Behavioral Bias on Tuning.
a, Top, angular sparsity plotted as a function of global behavioral bias in RW (left, blue), VR (right, red), and in both conditions (middle). Each data point is one unit, and all units from a single recording session are assigned the same global behavioral bias. Angular sparsity was significantly correlated with global behavioral bias for RW (r=0.23, p=9.9x10^{-9}), VR (r=0.31, p=1.6x10^{-12}), and the two conditions combined (r=0.53, p=9.5x10^{-78}). Bottom, same as above but for angular MVL (RW: r=0.12, p=3.6x10^{-3}; VR: r=0.25, p=2.2x10^{-8}; Combined: r= 0.31, p=2.5x10^{-25}). **b,** Top, same as **a** (top), but with angular sparsity plotted against local behavioral bias, showing a similar correlation of sparsity with behavioral bias (RW: r=0.20, p=8.7x10^{-7}; VR: r=0.10, p=2.6x10^{-2}; Combined: r= 0.41, p=4.1x10^{-44}). Bottom, same as **a** (bottom), but with MVL plotted against local behavioral bias, showing a similar correlation as above (RW: r=0.17, p=5.9x10^{-5}; VR: r=0.12, p=6.7x10^{-3}; Combined: r= 0.26, p=4.1x10^{-18}). A two-sided *t* test was used for all tests of significance in this figure.

We calculated the mean firing rate of cells in RW and VR and plotted the angular sparsity as a function of mean firing rate (Fig. 5-6a). We found a reliable negative correlation between the two variables. Interestingly, this negative correlation was present using both the binned method

and the GLM. A similar relationship was found between mean firing rate and spatial sparsity. There was also a significant negative correlation of the number of spikes with angular sparsity, angular MVL, and spatial sparsity (Fig. 5-6c).

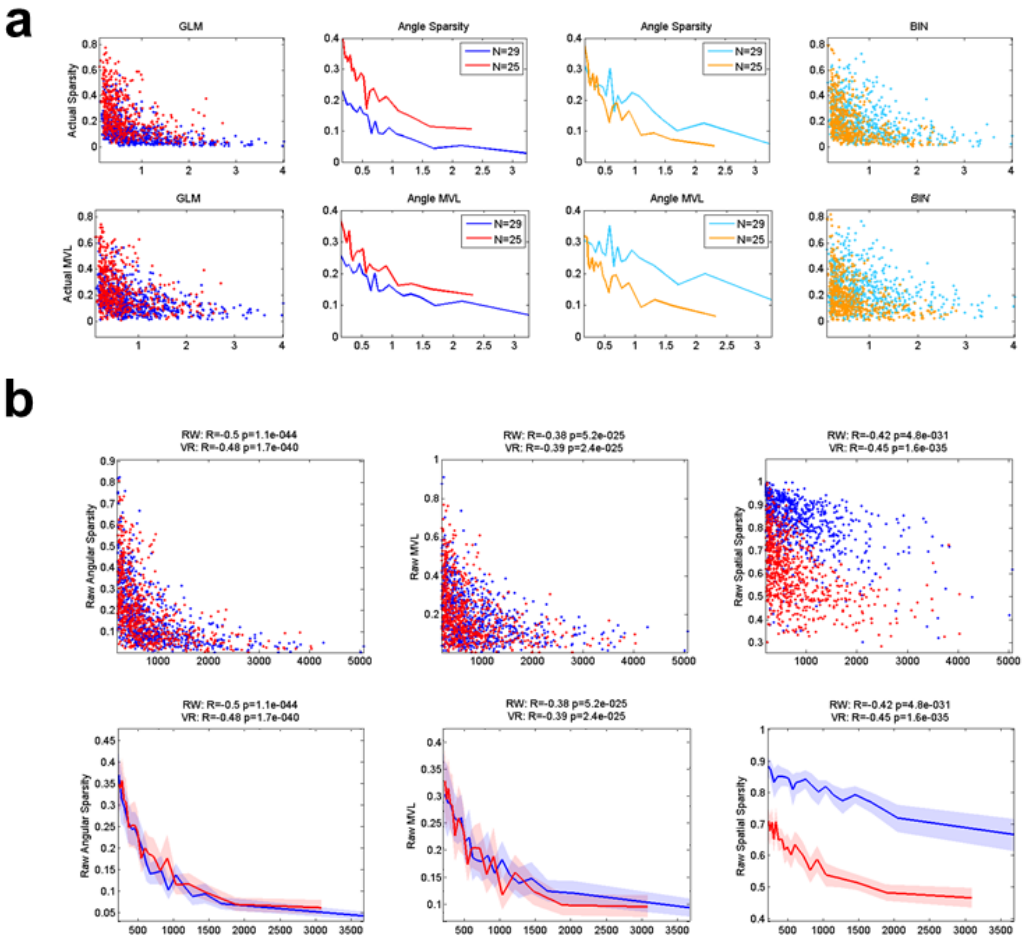

Figure 5-6 | Dependence of Tuning on the Mean Firing Rate and the Number of Spikes. **a,** Top, angular sparsity plotted against mean firing rate (in Hz), calculated using both the GLM (left plots) and the binned method (right plots). Blue and cyan points represent data recorded in RW; red and orange points represent data recorded in VR. Middle plots show the data grouped into bins of similar mean firing rate. Bottom, same as above but for MVL, which shows a similar relationship with mean firing rate. **b,** Angular sparsity (left), angular MVL (middle) and spatial sparsity (right) plotted as a function of the number of spikes a unit fires in a recording session. Blue data points represent units recorded in RW; red data points represent units recorded in VR. All three measures are significantly negatively correlated with the number of spikes in both RW (angular sparsity, r=-0.5, $p=1.1x10^{-44}$; MVL, r=-0.38, $p=5.2x10^{-25}$; spatial sparsity, r=-0.42, $p=4.8x10^{-31}$) and VR (angular sparsity, r=-0.48, $p=1.7x10^{-40}$; MVL, r=-0.39, $p=2.4x10^{-25}$; spatial sparsity, r=-0.45, $p=4.8x10^{-35}$).

Thus 3 measures that are significantly different between RW and VR – Behavioral Bias, Mean Firing Rate, and Number of Spikes – are all significantly correlated with tuning parameters. Two possibilities thus present themselves. It could be that these relationships are genuine and have a basis in biology. It could also be the case that these are artefactual, stemming from shortcomings in the analytical methods or a paucity of data. We addressed these possibilities with a number of statistical experiments based in resampling.

Mitigation of Spurious Correlations

There are a number of possible ways to mitigate these unintended correlations. The first way is to see how much of these correlations arise under a null assumption of zero angular sparsity. To test this, we generated surrogate data for each unit, using the same spatial firing map but with no angular modulation (Fig. 5-7). The angular modulation of these surrogate data also showed a slight negative correlation with firing rate, but the effect size was smaller. By subtracting the sparsity of the surrogate data from the original data, we arrived at an estimate of "excess sparsity" expressed by the neurons, which cannot be explained by the confounding variable.

Implementing this subtractive strategy on mean firing rate and number of spikes mitigated the dependence of sparsity on firing rate, but did not eliminate it completely. The largest effect was on the estimated sparsity of units in VR, demonstrating that the subtractive method is effective in eliminating spurious tuning due to the larger behavioral bias in VR. It is still unclear with this method if the relationship with sparsity and mean firing rate is a real relationship or spurious, but a similar analysis on the remaining correlation with another variable may further reduce the dependence.

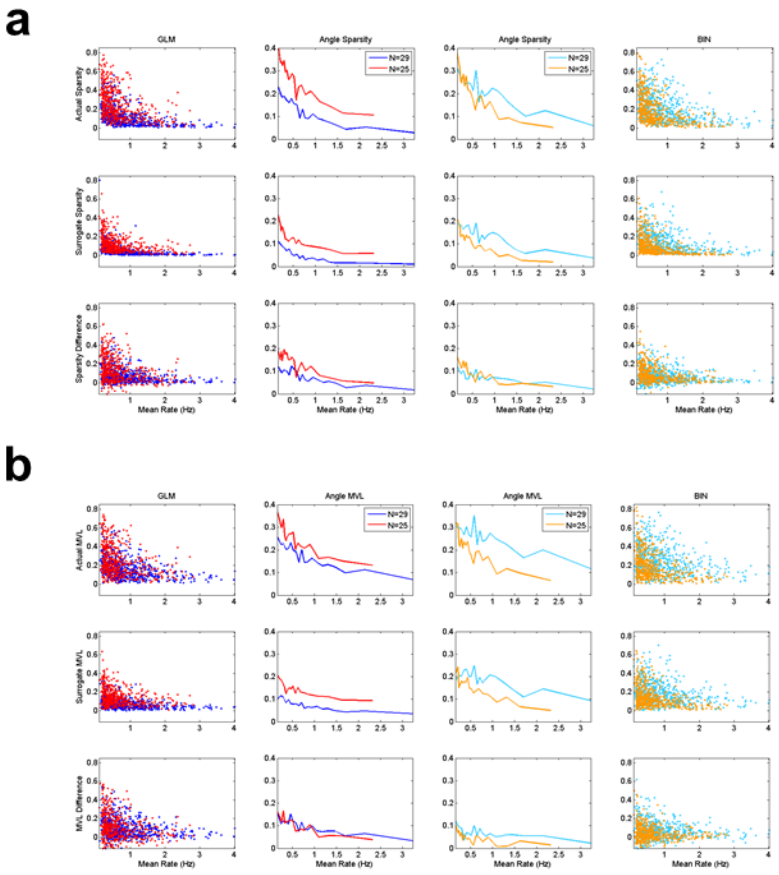

Figure 5-7 | Correcting for Latent Correlations.
a, Same color convention as in Figure 5-6a. Top, same as Figure 5-6a, top, showing a negative relationship between mean firing rate and angular sparsity. Surrogate data with no angular tuning was created for each unit using the non-parametric method of generating data. The resulting sparsity of the surrogate units is plotted against mean firing rate. Despite no angular tuning put in, both the GLM and binned methods still show a negative relationship between mean firing rate and sparsity. Bottom, the "corrected" sparsity was computed as the sparsity of the original unit less the sparsity of the matching surrogate unit. Though a relationship between mean firing rate and sparsity still exists, the effect size is much smaller in all cases. **b,** Same as **a**, but for MVL. The same effect of lessening the effect size of mean firing rate is replicated with MVL.

Another method of eliminating spurious correlations is to normalize the relevant measure to time-shifted (shuffled) data. Time-shifted data is the more accurate term, because the spike times are shifted with respect to behavior by a constant amount. This preserves the short-term dynamics of the spike trains, which is particularly relevant because hippocampal neurons tend to

fire in motifs of long bursts of spikes[36]. Thus, if a neuron fires only one motif consisting of 10 spikes within 2 seconds, most of those spikes are going to be clustered at similar head angles, resulting in high sparsity. Time-shifted control data will also show high sparsity, revealing the high sparsity of the original data to be non-significant. Shuffled data would likely show very little angular sparsity, giving the false impression that the original data was significantly tuned.

Data is circularly shifted by large amounts (±10 to 100 seconds) and the sparsity of the shifted data is computed. This is repeated multiple times for each neuron to form a null distribution for each neuron. If the null distribution is Gaussian-distributed, then the original data can be expressed in terms of Z-scores, or number of standard deviations from the mean. Measures that fall above 2 standard deviations can be said to be statistically significant at the $p<0.05$ level. If the null distribution is not Gaussian, then significance can be evaluated by calculating the percentage of data the original measure is larger (or smaller) than. The resolution of the p-value obtained this way depends on the number of values in the null distribution. With n resamples, the p-value can only take values of integer multiples of 1/n. So 20 samples are needed to claim $p<0.05$, 100 samples are needed to claim $p<0.01$, and so on. Because there is a dependence of sparsity on many other variables such as behavioral bias, mean firing rate, and the total number of spikes, it is important that each unit be compared to its own null distribution, rather than compared to distribution from the entire population.

This method of preparing data is very useful, and allows us to make claims about the percentages of units are significantly modulated in each population. When Z-scoring, it is tempting to interpret the z-scores as a measure of how well-tuned a unit is, but this is not statistically correct. The Z-score is a proxy for the p-value, and the same limitations that restrict the comparison of p-

values restrict the comparison of Z-scores. Importantly, the Z-score depends not just on the original value but the entire null distribution. Hence, the Z-scores from two units can only be compared if they come from the same null distribution, which is not the case for the majority of our data.

These issues certainly can benefit through the use of ANOVA. While ANOVA can indeed find significant differences in the presence of confounding factors, many assumptions are made that are often not true. Balanced experiments are ideal, in which sample sizes are equal for each treatment. This is difficult to fulfill using electrophysiological data in freely behaving animals without discarding large amounts of data. Further, data are often not independent, as multiple units are recorded in the same behavioral condition. Additionally, normality of the distributions of residuals is often difficult to demonstrate. Finally, the variance in the different groups is often not equal, another assumption of ANOVA. Despite these difficulties, it can be instructive to group data together to check for systematic relationships. Unfortunately, in our data, the confounding variables can be largely non-overlapping, resulting in very few bins with a good number of cells in both conditions.

Implications for Future Analyses

The above statistical experiments should be a call to diligence in data analysis. It is easy to become enamored with new techniques that promise to solve previously insurmountable problems, especially when applied to novel problem spaces. New methods must be rigorously vetted and validated using examples that are as simple and as easily interpretable as possible. Co-variation of measures of interest with “background” measures should be taken seriously, with differences between experimental conditions viewed with a suspicious eye. The question of

whether a result can be attributable to firing rate should be one of the first to be asked in any analysis of in vivo electrophysiological data. Finally, it is critically important to interpret control data the correct way. Values should only be z-scored if their null distributions are Gaussian. Even when non-parametric measures of significance are used, it is crucial to either compare each unit to its own null distribution or validate that all data come from an approximately equal null distribution. Comparing a population of neurons to the "distribution of shuffled data[84]" is a dangerous proposition if the population varies widely in firing rate and the relevant variable is dependent on firing rate. In our case, this would bias more cells with low firing rates to be significant, as their sparsity values are generally higher than shifted data from high-rate cells. New statistical methods hold the promise of being able to interrogate data deeper than before, and it is incumbent upon the data analyst to use these methods carefully, clearly, and properly.

6. Hippocampal neural dynamics in a virtual water maze

Introduction

The Morris Water Maze[2,29,30,103] (MWM) has become the gold standard behavioral experiment for spatial navigation and spatial memory[20]. The effects of LTP[104,105], NMDA antagonists[106–108], psychoactive drugs[109–111], and other molecular or genetic modifications are often evaluated by performance in the hippocampus-dependent MWM[3,30,112]. However, beyond the necessity of long-term potentiation for this task, the neural mechanisms underlying this behavior are not well-characterized.

Morris stated that the ability to perform this task "[provides] support for the cognitive mapping theory of spatial localization," which states that to solve the task, the rats must form an allocentric mental representation of the area they are moving in[29]. The possible neural basis of such a cognitive map of space had been discovered more than a decade prior, in the form of "place cells" in the dorsal hippocampus[4,5]. Different cells are active in different regions of the environment, and enough cells can cover and represent an entire environment. It seems natural to conclude that these place cells form the cognitive map necessary for MWM performance. Multiple questions arise from this theory: What do place cells do in the water maze? Are they necessary for MWM performance? Do place cell responses change as the subject's performance gets better? These questions have not been directly addressed using *in vivo* electrophysiology.

This gap in knowledge is largely attributable to the immersion of the subject in water in the task; the presence of water eliminates any local cues, such that the goal object is invisible, inaudible,

and undetectable by smell[29]. Thus all navigation must be landmark-based, and the subjects must learn the spatial location of the goal relative to distal cues, rather than forming simple stimulus-response associations[29]. Although there is always the risk of incomplete elimination of non-specific cues in RW, this task minimizes the possibility that the subjects might form alternate strategies to solve the task. But this environment provides several hindrances to electrophysiological interrogation. First, the water environment is stressful for rodents. As stress can alter neural responses and interfere with mechanisms of plasticity[113–117], this represents a difficulty in interpreting any neural data in this version of the task. Second, every trial begins with the experimenter releasing the rat from a start location, and the experimenter can serve as a very salient cue for the rat or mouse. Third, the nature of the task limits the number of trials the rat can perform, typically to 4 or 8 trials per day, limiting the data available for analysis. This is a major hurdle for characterizing putative place cells, as a region must be visited several times to form a good estimate of a place cell's receptive field. Finally, water is a physical hazard to *in-vivo* electrophysiology. Splashing or dunking the head underwater can easily damage expensive electrophysiology systems. Customized, state-of-the-art waterproof electrode housings are necessary to obtain valid recordings, and these are only recently available and limit the number of implantable electrodes[31–33].

To overcome these difficulties, we utilized a body-fixed virtual reality (VR) system[34,36,37] which was previously shown to support virtual water maze learning in rats[35]. This virtual adaptation has several advantages over the traditional MWM: stress is reduced in this appetitive task, as the rats are comfortable and relaxed in the VR; after the rat is harnessed into the VR, there is absolutely no experimenter-rat interaction, eliminating possible complications introduced by the presence of the experimenter; this version of the task allows rats to perform more than 100 trials in a single

day, yielding much more data and denser coverage of the environment than before; finally, there is no water involved, but proximal cues still provide no information about the location of the reward zone. This preserves the landmark-based nature of the water maze task while permitting electrophysiological recordings to be performed simultaneously. This allowed us to investigate the firing patterns in the hippocampus during this spatial navigation task.

Previous studies have explored the responses of CA1 pyramidal cells when the rats explore this virtual environment. In the simplest task, in which the rats travel back and forth on a linear track, we observe place fields similar to those seen in real world one-dimensional tracks[34]. However, when the rats are free to do random foraging across the 2-D environment, spatial selectivity is severely diminished[36]. This reduced selectivity could be due to a number of reasons. We previously concluded that distal visual cues are not enough to generate spatial selectivity; multiple cues (visual olfactory, self-motion, tactile, auditory, etc.) must be repeatedly paired with each other to form stable place fields. Some may also argue that the task of random foraging is not demanding enough, that the task does not require attention to be paid to the visual cues; in essence, because a map is not needed, a map does not form. Successful navigation in the virtual water maze task would dispel such an argument based on task demand, so we demonstrated the ability of rats to perform this task and then characterized the neural responses

The Virtual Water Maze

The virtual reality system used was identical to that described previously[35]. In the majority of data, the virtual environment consists of a table 2m in diameter placed in the center of a square room 450 x 450cm (Fig. 6-1a). The visual texture on the table is patterned to provide optic flow but provide no local cues about position. Each wall has a different, salient visual cue; for the

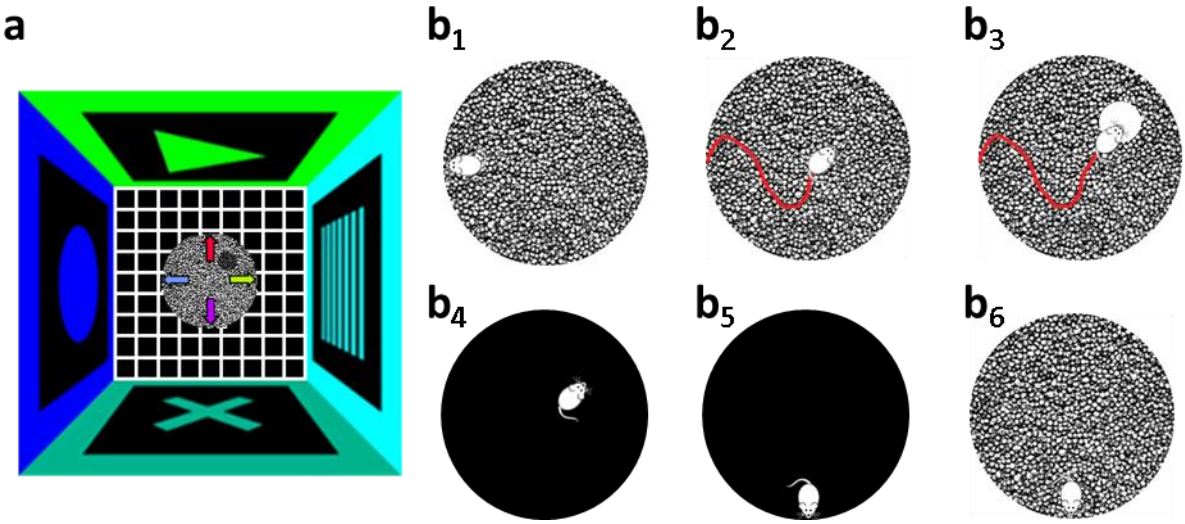

Figure 6-1 | The Virtual Water Maze Task.
a, Overhead view of the virtual environment. The central table is 2 m in diameter, and is placed 75 cm above the floor. The walls define a square room 4.5x4.5 m and provide distal visual cues. See methods for additional information. **b,** Schematic diagram defining one trial. **b_1,** The rat begins a trial in one of 4 (or 8) start locations on the edge of the table, facing radially outward. **b_2,** The rat explores the environment. **b_3,** Upon entry into the reward zone, a white dot appears, and sugar water reward is dispensed for 2.7 seconds. **b_4,** The entire environment is blacked out, and the ball is decoupled from movement in virtual space. **b_5,** During the blackout, the rat is "teleported" to a new, randomly chosen start position. **b_6,** After a 2.5 second wait period, the ball is re-activated, the lights turn on, and the next trial begins. During training, this is repeated until 45 minutes have elapsed or 40 trials are completed. During testing, sessions last as long as the rat shows motivation to perform the task.

majority of data the reward zone was in the north-east quadrant of the table. During training, the reward zone was 30 cm in radius. After 6 days of training, the reward zone was shrank to 25 cm and then 20 cm on the 7^{th} and 8^{th} days, respectively.

One trial is defined as follows. The rat starts in of the 4 (or 8) start locations, facing radially outward (Fig. 6-1b_1). The reward zone is completely hidden from sight. The rats explore the environment in an unguided fashion until they enter the reward zone (Fig. 6-1b_2). Once they enter, the reward zone appears as a white dot, and a sugar-water reward is dispensed to the rats, available for 2.7 seconds, or until the rat leaves the reward zone (Fig. 6-1b_3). At that point, the virtual world is "blacked out" and the ball is decoupled, such that the rat's movements do not

induce a change in virtual position (Fig. 6-1b$_4$). During this blackout period, the rat is teleported to a new random start location (Fig. 6-1b$_5$). After a delay of 2.5 seconds, the ball is activated and the visual scene returns, beginning the next trial (Fig. 6-1b$_6$). During training, this is repeated until 45 minutes have elapsed or 40 trials are completed. All data presented are from rats that have completed the 8-day training.

Behavioral Results

We previously reported that rats learned the task well and showed behavioral measures comparable to RW water mazes, including latency and distance to reward and time spent in the target quadrant during a probe test[35]. Further analysis of behavior trajectories showed that rats took near-optimal paths from any start location to the reward. Both individual paths (Fig. 6-2a, light colored traces) and average paths (Fig. 6-2a, thick black traces) showed direct routes from any start position to the goal, with little indication of random circling, or attraction to the edge of the virtual table (thigmotaxis in RW environments).

We also considered the possibility that the rats might have learned to execute a particular series of motions from any start position which would guarantee reward. To rule this out, we took the average path from each start location and rotated them so they are starting from the same position (Fig. 6-2b). The mean paths diverged as the rat traveled greater distances, demonstrating start position-specific trajectories. To quantify this divergence, we computed the correlation between environmental occupancy for paths taken across several start locations and for paths taken within a single start location (Fig. 6-2c). Occupancy correlation taken from different start locations (0.55) was significantly smaller ($p=1.4x10^{-17}$) than the correlation taken from within the same start location (0.77). This demonstrates that paths taken from different start locations

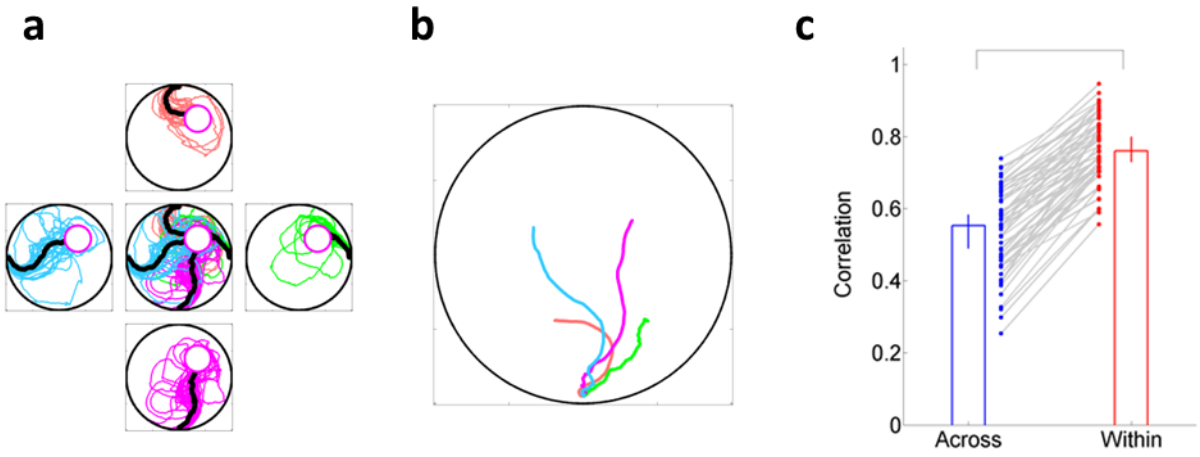

Figure 6-2 | Trajectories are Efficient, Repeated, and Differ between Start Locations.
a, Behavioral data from an example recording session. Light traces show the rat's trajectory, color coded by start position (red, top; green, right; magenta, bottom; blue, left). Thick black traces show the mean trajectory from each start location. The magenta circle denotes the boundary of the reward location. Rats take near-optimal paths from any start location to the goal location. **b,** The mean trajectories shown in **a** are rotated such that they all start from the south position, and color coded by original start position. The mean paths are initially similar, but diverge as trials progress, indicating the rat is not executing a single stereotyped trajectory from all start locations. **c,** The correlation between environmental occupancy (see Methods) taking paths across start positions (0.55, [0.49, 0.58], n=60 recording sessions) was significantly smaller ($p=1.4x10^{-17}$, Wilcoxon signed-rank test) than that defined within start positions (0.77, [0.74, 0.81], n=60 recording sessions), demonstrating both similar trajectories from a given start location and differing trajectories from different start locations.

are indeed different, and that paths taken from the same start location are largely the same. This, combined with a previous study showing that rats cannot perform this task in the absence of visual cues[35], shows that rats are using the distal visual cues to solve the task, and do not rely on alternate strategies.

Allocentric Spatial Responses

We computed the allocentric spatial responses of 523 putative pyramidal neurons from dorsal CA1 as described before (see Methods)[36]. If place cells support the cognitive map proposed to be

necessary for the MWM, neurons should show robust place fields during the task. Surprisingly, we found very little allocentric spatial selectivity in CA1 pyramidal units, the classic "place cells" (Fig. 6-3a). Very few cells have an elevated firing rate in only one region of space and

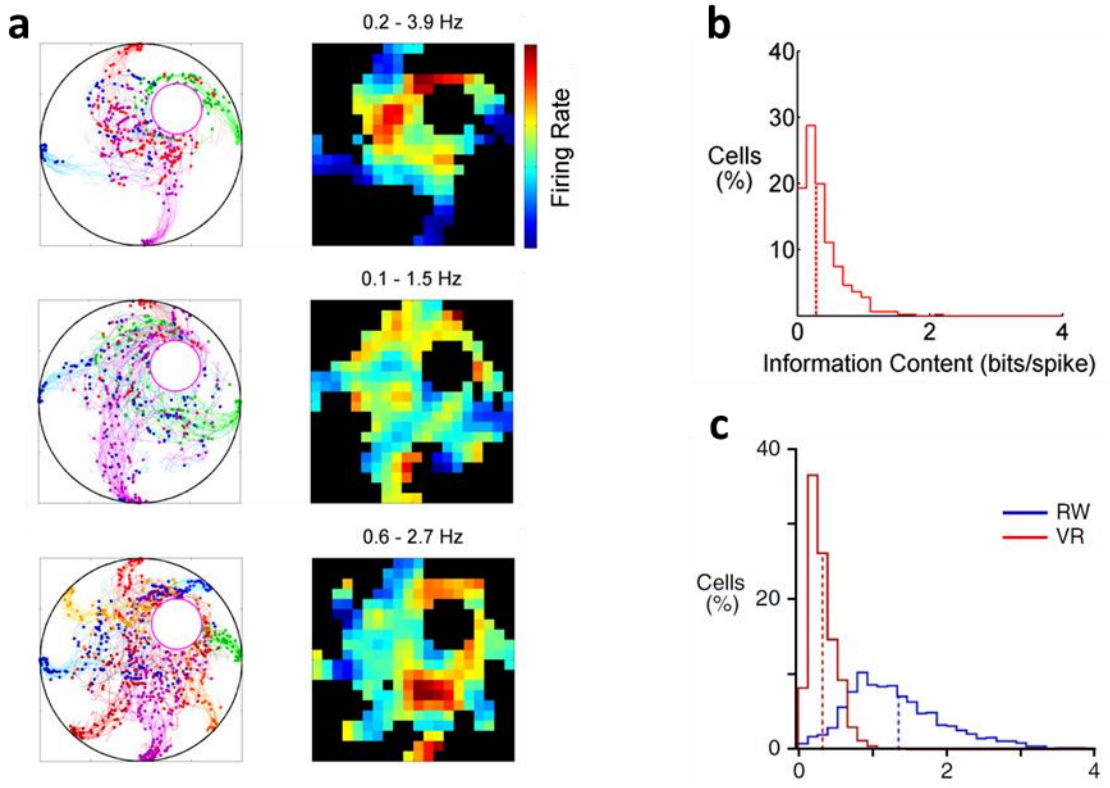

Figure 6-3 | CA1 Pyramidal Neurons Lack Allocentric Spatial Selectivity in the Virtual Water Maze.
a, Example trajectory-spike (left) and rate-map (right) plots from three putative pyramidal cells in dorsal CA1. Light traces indicate the rat's trajectory, and dark dots mark the position of spikes from a single neuron; both paths and spikes are color coded according to start position. The rate maps are scaled such that the lowest firing rate is deep blue and the highest firing rate is deep red; these values are indicated in the titles of each map. Note that these neurons fire spikes at all positions, without a large increase in firing rate in a restricted region of the environment. **b,** The information content, a standard measure of spatial selectivity for place cells, was quite small (0.28, [0.26, 0.31] bits/spike, n=523 pyramidal units) in the virtual water maze task, despite near-optimal behavioral performance (see Fig. 6-2). **c,** The information content in a 2-dimensional random foraging task in the same VR had comparable information content to information content in the Virtual Water Maze; both were substantially less than information content in a 2-dimensional random foraging task in RW. This indicates that the level of task demand is not a determining factor in the presence or absence of spatial information content. Subpanel **c** adapted from Aghajan et al., 2015[36].

minimal firing everywhere else; instead, firing is diffuse throughout the environment. This lack of spatial selectivity is quantified by the low information content (0.28 bits/spike, Fig. 6-3b). This is at a similar level as information content in cells from a previous study with rats performing a random foraging task in the same VR (Fig. 6-3c)[36]. This demonstrates that there is no simple task-type or task-complexity dependence of spatial selectivity in our VR. Because rats must pay attention to the visual cues to show the quality of behavior shown in Figure 6-1, this also rules out the possibility that cells in the random foraging task showed no selectivity because the rats were not paying attention to the visual cues.

Episodic Distance Selectivity

We next asked if there was any selectivity to distance traveled, as several neurons show such tuning during random forging[36] and one-dimensional running in VR[34]. We aligned position to the start of each trial, such that all trials began at 0 cm. In contrast to allocentric spatial selectivity, we saw robust distance selectivity (Fig. 6-4a). Different cells were tuned to different distances traveled, elevating their firing rates only around a particular distance, and suppressing their firing at other times, bearing a resemblance to place fields on one-dimensional tracks. This firing was largely independent of starting position. Of 523 putative pyramidal neurons, 127 (24%) had significant tuning to distance. All distances up to 300 cm were represented (Fig. 6-4b), with greater selectivity at shorter distances, perhaps reflecting an accumulation of error in path integration. For the entire population, the information content in the distance domain (0.56 bits/spike) was significantly higher ($p=1.1x10^{-74}$) than information content in the position domain, and the two measures were also positively correlated (r=0.70) (Fig. 6-4c).

We also compared the information content in the distance domain with information content in the time domain[99]. We calculated time as the total time spent moving since the trial start, excluding pauses. On a population level, information content for distance was comparable to but slightly lower (p=0.008) than information content for time (0.56 bits/spike). The two measures were also strongly correlated (r=0.94). This similarity is likely due to a high correlation between

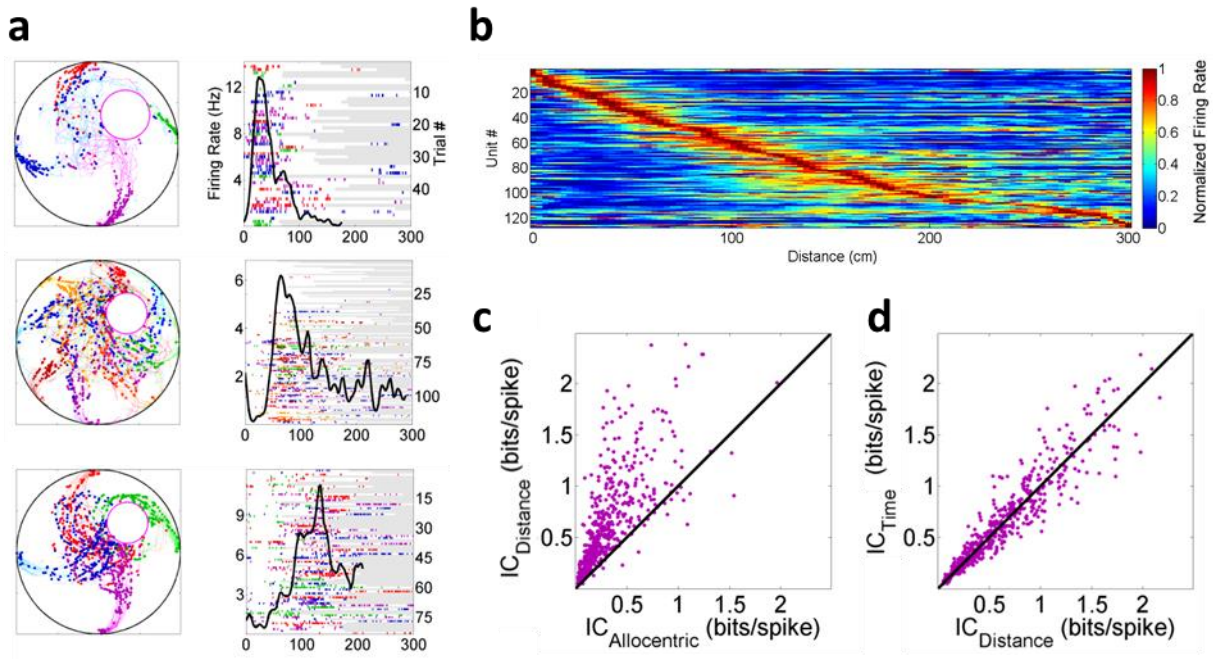

Figure 6-4 | CA1 Pyramidal Neurons Show Strong Egocentric Distance Selectivity in the Virtual Water Maze.
a, Example trajectory-spike (left) and distance raster (right) plots from three putative pyramidal cells in dorsal CA1. Raster ticks are color-coded based on starting position. All trials begin at distance 0 and end at the interface between the white and gray region. These neurons have high firing rates at specific distances along the rat's path, regardless of starting position. Different cells code for different distances. **b,** All units with significant information content in the distance domain (127/523, 24%) were sorted according to the location of the peak in their firing rate map, and normalized to their peak firing. All distances up to 300 cm are represented by the population of cells. **c,** Information content in the egocentric distance domain (0.56, [0.53, 0.61] bits/spike, n=523 pyramidal units) was significantly larger ($p=1.1x10^{-74}$, Wilcoxon signed-rank test) than information content in the allocentric domain (0.28, [0.26, 0.31] bits/spike, n=523 pyramidal units), and the two were strongly correlated (r=0.70, $p=2.5x10^{-79}$, two-sided *t* test). **d,** Information content in the egocentric distance domain was highly correlated (r=0.94, $p=2.6x10^{-237}$, two-sided *t* test) with information content in the time domain (0.56, [0.52, 0.62], n=523 pyramidal units). Information content in the time domain was slightly but significantly greater than that in the distance domain ($p=3x10^{-2}$, Wilcoxon signed-rank test).

distance and time in well-trained rats that run at a fairly constant velocity and do not spend much time pausing. Additional experiments with untrained rats or with modifications to the gain of the VR system will be needed to truly tell if these cells are responding to distance or time.

Head-Direction Selectivity

Another feature that pyramidal units respond to during random foraging is head direction within the virtual space[37]. However, due to the stereotyped trajectories the well-trained rats take in the virtual water maze, distance and head direction can be easily confounded. The best way to disentangle these sources of tuning is to analyze firing using a generalized-linear model[37]. Here, we approximated angular tuning by only considering the 365 units without significant distance tuning. 85 of these 365 units (23%) showed significant angular tuning, with elevated firing only at selective head-directions and minimal firing at other directions (Fig. 6-5a). The angular tuning maps of these units showed different preferred directions of firing and different types of selectivity; several maps show bimodal tuning, and some exhibit a "negative map[118]," with decreased firing for a limited range of head angles (Fig. 6-5a). The entire population of non-distance cells had a median angular sparsity of 0.17; units with significant angular tuning had a median angular sparsity of 0.27 (Fig. 6-5b). The nature of these responses, as well as their overall prevalence, is comparable to that seen in units during random foraging[37].

We next analyzed the tuning of the population of significantly tuned units, to see if there was a bias towards any particular salient distal visual cue[37] that might guide the rat to the reward zone. The distribution of the preferred direction for significantly tuned units (mean angle 51.4°) was not different from a uniform distribution ($p=0.37$), with a small mean vector length (0.11), indicating that there was no bias in the direction of peak firing (Fig. 6-5c, left). We also

computed the mean firing rate of all significantly tuned units as a function of head angle; this distribution, too, was not significantly different from a uniform distribution (p=0.85), with a small mean vector length (0.04, mean angle 118°) (Fig. 6-5c, right). This demonstrates that all

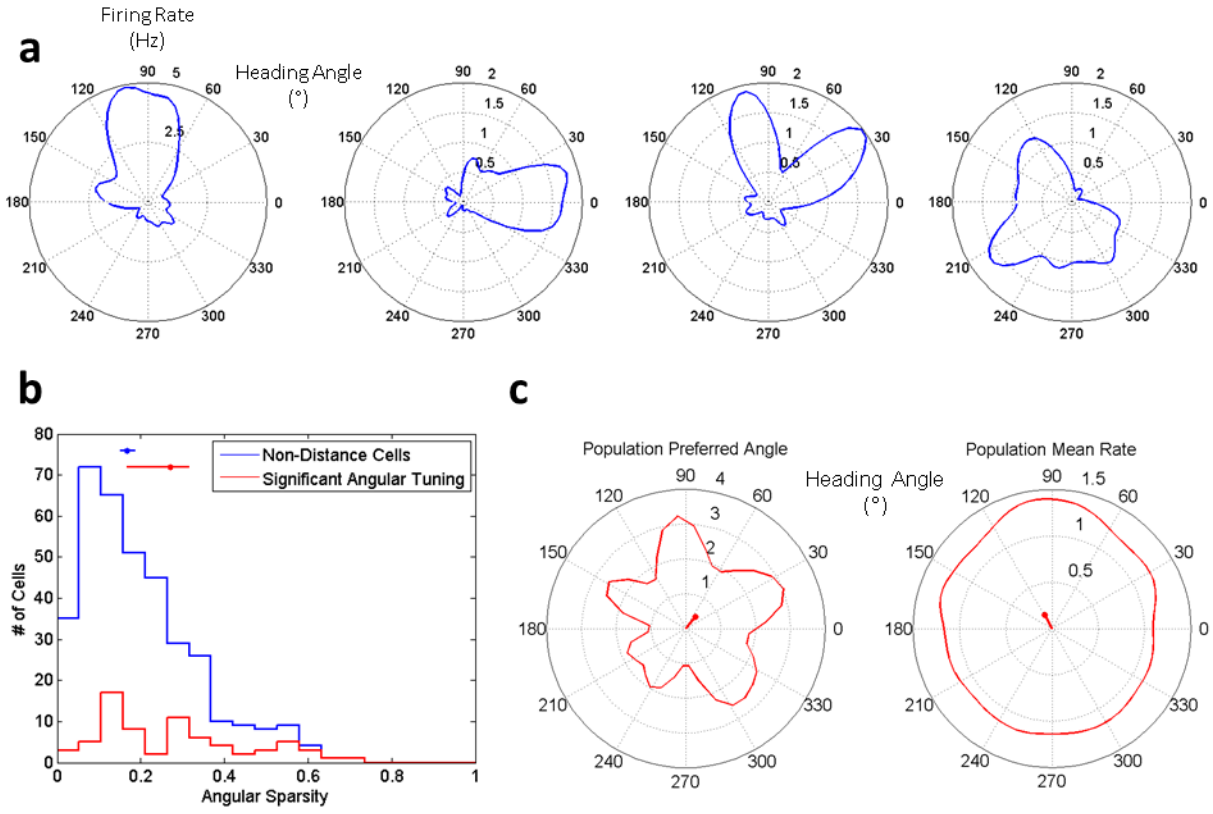

Figure 6-5 | Head-direction Tuning in the Virtual Water Maze.
a, Example polar rate plots from four pyramidal cells. The angles correspond with the environmental schematic in Figure 6-1. The first and second sample neurons are tuned for a single head angle, firing maximally in one direction and minimally in all others. The third sample neuron has multimodal tuning, preferring to fire in two separate directions. The fourth sample neuron has suppressed firing in 90 degrees of the head-angle space but equal firing at all other angles. **b,** To avoid confounds of distance and head angle, only units without significant distance selectivity (365 units) were used for population analyses. 85 of these 365 (23%) had significant angular sparsity. Histogram shows the distribution of angular sparsity for all non-distance modulated units (blue, 0.17, [0.15, 0.19], n=365 pyramidal units) and for the subset of units with significant angular sparsity (red, 0.27, [0.17, 0.31], n=85 pyramidal units). **c,** Left, distribution of the preferred direction of firing for units with significant angular sparsity covered the entire range of head angles and the distribution was not significantly different from a uniform distribution (p=0.37, Rayleigh test for circular data, n=85 pyramidal units). The mean vector of the distribution is plotted in the center, scaled up by a factor of 4 for visibility. Right, mean firing rate as a function of head angle for units with significant angular sparsity showed little clustering towards a particular angle; the distribution was not significantly different from a uniform distribution (p=0.85, Rayleigh test for circular data, n=85 pyramidal units). The mean vector of the distribution is plotted in the center, scaled up by a factor of 4.

head angles are represented during the virtual water maze task, and provides cellular-level evidence that the rats are not overly relying on any particular distal visual cue to help in navigation.

Modulation by Reward

We also investigated the response of these units to the delivery and anticipation of reward. Rather than align spikes to the beginning of a trial, we aligned spikes to the time at which the rat entered the reward zone for each trial, including 2.7 seconds before and after. Several cells showed elevated firing rates immediately before the reward was dispensed which then shut down as soon as the reward is given (Fig. 6-6a, top row). Note that there is no direct stimulus that represents the location of the reward, and the rats approach the reward from a range of places and angles (Fig. 6-2a); hence, these cells can be seen as responding to the expectation of reward, rather than any particular stimulus. Other cells were quiet before the reward was dispensed, and greatly increased their firing rates after reward (Fig. 6-6a, bottom row). Some cells even fired with a significant delay after reward. We quantified these responses with the reward modulation index (RMI, see Methods), calculated only for those cells with a mean firing rate greater than 1.5 Hz near the reward (94 units, 18%). Far more cells had a negative RMI, indicating a propensity to fire at higher rates before the reward than after. This is reminiscent of dopamine neurons coding for the discrepancy between expected reward and actual reward, though the purpose of such coding in hippocampal pyramidal neurons in unclear.

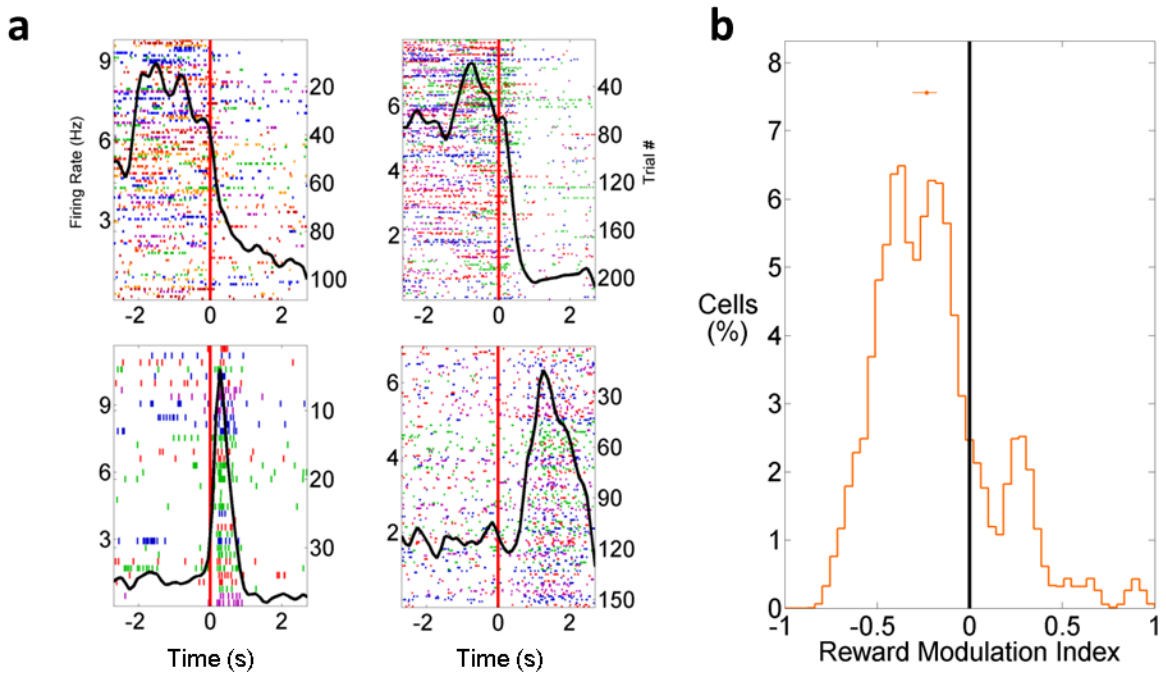

Figure 6-6 | Rate Modulation by Reward.
a, Example peri-reward raster plots from four pyramidal cells. 2.7 seconds before and after entry into the reward zone (red line at 0) are plotted. The neurons in the top row show anticipatory firing and then quickly shut off after reward. The neurons in the bottom row dramatically increase their firing after reward. Responses can be punctate (bottom left) or sustained (bottom right). **b,** Histogram of the reward modulation index for all units with a mean rate greater than 1.5 Hz across the time span of 2.7 seconds before and after the reward (94 pyramidal units). Both anticipatory and retrospective modulation is present, but the population has a bias towards negative values (-0.23, [-0.31, -0.18], n=94 pyramidal units; $p=9.2x10^{-8}$, Wilcoxon signed-rank test), indicating a preference to reduce firing rate after reward is dispensed.

Discussion

This is the first electrophysiological study of single-unit responses in a landmark-based navigation task. Rats demonstrated a clear ability to solve the task in a way which depended on the visual cues, and we made a number of exciting discoveries that call into question many assumptions about spatial navigation.

First, we find that there is very little allocentric spatial selectivity in the form of place fields in dorsal CA1. These responses are supposed to form the basis of the cognitive map required to perform the MWM, but our rats' performance is intact without this allocentric map. This is contrary to many theories of spatial navigation, but not without precedent: one of the original papers describing the water maze stated

"… given that place units detected so far in the hippocampus respond only with respect to places in which the rat is presently situated as opposed to places to which it intends to go, these results pose a challenge for electrophysiologists attempting to explain the neural mechanisms by which the hippocampus processes spatial information[30]."

This issue can partly be resolved by the finding of forward mental sweeps of place cells during decision points[119,120], but such activity has not been shown to be necessary for successful navigation, particularly in a water maze task. A possible explanation for the lack of spatial selectivity but intact navigational ability might be overtraining[107]. It is possible that the rats in the current study are overtrained to the point where the virtual water maze task is no longer hippocampus-dependent, but striatum-dependent[121]. We find this unlikely, as robust place fields are present during a linear track task in RW and VR[34], a simple task that is not hippocampus-dependent. There is also little precedent for neural representations totally degrading once they are no longer needed for a particular task.

Instead of allocentric spatial selectivity, we see an episodic distance map in about one quarter of units. This is expressed in terms of the distance traveled since the beginning of any trial, independent of start position, and covers all distances from the beginning of a trial up to 300 cm of distance traveled. This cutoff could be due to increased error accumulation with distance, or

might reflect the fact that rats had very few trials that went beyond 300 cm. Information content in the egocentric distance domain was greater than that in the allocentric spatial domain, and comparable to that in the time domain. Future experiments with changes in the gain of the VR ball or with untrained rats will be needed to differentiate tuning to distance from tuning to time.

In addition to coding for distance traveled, about one quarter of the remaining neurons had significant tuning to the rat's head angle. All directions were represented, with no bias in either the distribution of the preferred angles or the mean firing rate of the population. This serves as an additional, cellular level, verification that the rats' behavior was not unduly influenced by distal visual cues, as no particular angle was over-represented, at least in the hippocampus. Recording in other head-direction nuclei in this task may indeed reveal a bias. There may also be head-direction tuning not in a world-centered reference frame but a goal-centered frame, where neurons would have increased firing when facing the reward zone, independent of head angle. The stereotyped behavior of the rats in the current study precludes this kind of analysis, as there is insufficient sampling of all head angles at all positions or distances to detect such a difference. Similar future experiments with a larger table and rats more naïve to the task will be necessary to explore this possibility.

Finally, approximately 20% of neurons had increased activity around the time the rat entered the reward zone. Rather than responding to the delivery of reward, the majority of these units had a larger firing rate just before the reward was delivered, and suppressed their firing once the reward was delivered. These units may represent the discrepancy between expected reward and actual reward, operating in a similar manner to dopamine systems responding to reward. We observed some units that preferentially fired when the rat was in the reward zone, but there were

not enough to fully analyze. Additional data will be necessary to determine the short- and long-term dynamics of these reward-modulated neurons and their relation to learning the virtual water maze task.

Hence the allocentric "cognitive map" associated with place cells is not necessary for navigation based on distal visual cues. Without place cells, how is it possible for rats to navigate to the reward zone? We propose that a combination of episodic distance selectivity and allocentric head-direction selectivity provides sufficient information to be able to solve this task. In this model, head-direction selective neurons would first provide information about the starting position of the rat. Integration of continuous head-direction signals[122] coupled with distance will allow the construction of a path from any start position to the goal[122,123]. Distance coding, as well as firing at times near the presentation of reward, could represent each instant in one "episode" of a trial, with angular tuning anchoring these episodes to the allocentric space. Finally, it is possible that the receptive fields of these neurons may change with experience, as is the case on 1-dimensional tracks. Such changes, tracked over the course of learning the virtual water maze, may reveal important links between neural activity and behavior in a way not previously possible.

7. Conclusions

By utilizing the above novel technologies, we are bringing closer the two worlds of the hippocampus, one of *in vivo* electrophysiology of spatial coding, and the other of the integral function of the hippocampus in episodic memory. In view of the fact that sensorimotor information is egocentric by nature, our insights about self-movement representations, the possible computations carried out by dendrites, as well as the predictive nature of coding in PPC will be essential in determining how self-motion and self-referenced sensory information can be translated to an allocentric map. But it is clear from our studies in VR that the view of hippocampal cells as only representing allocentric space is in need of revision. This network also has representations of head-angle and distance that are sometimes, but not always, concurrent with allocentric spatial representations.

Quite surprising is our finding that rats can learn a landmark based navigation task, in the form of the Virtual Water Maze, in the complete absence of hippocampal spatial selectivity. While this does not mean that allocentric representations are never used during spatial navigation, it does mean that this behavior is not dependent on such a representation. In our hands, the representations of episodic distance and allocentric head angle are enough to support spatial navigation. In this view, hippocampal cells become active during particular points in an episode of a single trial, rather than at a particular location. Perhaps allocentric “place” is less of an absolute measure in the brain, and more akin to the representation of episodes of previous experiences. The way such representations form through nonlinear dendritic computations on multiple sources of information will be fascinating to study as these technologies improve further, and will lead us to a more complete understanding of episodic memory.

References

1. Scoville, W. B. & Milner, B. Loss of recent memory after bilateral hippocampal lesions. *J. Neuropsychiatry Clin. Neurosci.* **20,** 11–21 (1957).

2. Morris, R. Developments of a water-maze procedure for studying spatial learning in the rat. *J. Neurosci. Methods* **11,** 47–60 (1984).

3. Rudy, J. W. & Sutherland, R. J. The hippocampal formation is necessary for rats to learn and remember configural discriminations. *Behav. Brain Res.* **34,** 97–109 (1989).

4. O'Keefe, J. & Dostrovsky, J. The hippocampus as a spatial map . Preliminary evidence from unit activity in the freely-moving rat. *Brain Res.* **34,** 171–175 (1971).

5. O'Keefe, J. & Nadel, L. *The Hippocamps as a Cognitive Map*. *Hippocampus* (Oxford University Press, 1978).

6. O'Keefe, J. in *The Hippocampus Book* (Andersen, P., Morris, R., Amaral, D., Bliss, T. & O'Keefe, J.) 475–548 (Oxford University Press, 2007).

7. Muller, R. U. & Kubie, J. L. The Effects of Changes in the Environment on the Spatial Firing of Hippocampal Complex-Spike Cells. *J. Neurosci.* **7,** 1951–1968 (1987).

8. Quirk, G. J., Muller, R. U. & Kubie, J. L. The firing of hippocampal place cells in the dark depends on the rat's recent experience. *J. Neurosci.* **10,** 2008–2017 (1990).

9. Muller, R. U., Kubie, J. L. & Ranck, J. B. Spatial Firing Patterns of Hippocampal Complex-Spike Cells in a Fixed Environment. *J. Neurosci.* **7,** 1935–1950 (1987).

10. Save, E., Nerad, L. & Poucet, B. Contribution of multiple sensory information to place field stability in hippocampal place cells. *Hippocampus* **10,** 64–76 (2000).

11. Aikath, D., Weible, A. P., Rowland, D. C. & Kentros, C. G. Role of self-generated odor cues in contextual representation. *Hippocampus* **24,** 1039–1051 (2014).

12. Battaglia, F. P., Sutherland, G. R. & McNaughton, B. L. Local Sensory Cues and Place Cell Directionality: Additional Evidence of Prospective Coding in the Hippocampus. *J. Neurosci.* **24,** 4541–4550 (2004).

13. Knierim, J. J. Dynamic interactions between local surface cues, distal landmarks, and intrinsic circuitry in hippocampal place cells. *J. Neurosci.* **22,** 6254–6264 (2002).

14. Markus, E. J. *et al.* Interactions between location and task affect the spatial and directional firing of hippocampal neurons. *J. Neurosci.* **15,** 7079–94 (1995).

15. Wood, E. R., Dudchenko, P. A., Robitsek, R. J. & Eichenbaum, H. Hippocampal neurons encode information about different types of memory episodes occurring in the same location. *Neuron* **27,** 623–633 (2000).

16. Mehta, M. R., Barnes, C. A. & McNaughton, B. L. Experience-dependent, asymmetric expansion of hippocampal place fields. *Proc. Natl. Acad. Sci. U. S. A.* **94,** 8918–21 (1997).

17. Mehta, M. R., Quirk, M. C. & Wilson, M. A. Experience-dependent asymmetric shape of hippocampal receptive fields. *Neuron* **25,** 707–15 (2000).

18. Nitz, D. Parietal cortex, navigation, and the construction of arbitrary reference frames for spatial information. *Neurobiol. Learn. Mem.* **91,** 179–85 (2009).

19. Nitz, D. A. Tracking route progression in the posterior parietal cortex. *Neuron* **49,** 747–56 (2006).

20. Poucet, B. *et al.* Is there a pilot in the brain? Contribution of the self-positioning system to spatial navigation. *Front. Behav. Neurosci.* **9,** 1–10 (2015).

21. Johnston, D. & Narayanan, R. Active dendrites: colorful wings of the mysterious butterflies. *Trends Neurosci.* **31,** 309–16 (2008).

22. Mel, B. W. Synaptic integration in an excitable dendritic tree. *J. Neurophysiol.* **70,** 1086–101 (1993).

23. Häusser, M. & Mel, B. Dendrites: bug or feature? *Curr. Opin. Neurobiol.* **13,** 372–383 (2003).

24. Mehta, M. R. Cooperative LTP can map memory sequences on dendritic branches. *Trends Neurosci.* **27,** 69–72 (2004).

25. London, M. & Häusser, M. Dendritic computation. *Annu. Rev. Neurosci.* **28,** 503–532 (2005).

26. Muller, R. U., Bostock, E., Taube, J. S. & Kubie, J. L. On the directional firing properties of hippocampal place cells. *J. Neurosci.* **14,** 7235–7251 (1994).

27. Burgess, N., Cacucci, F., Lever, C. & O'keefe, J. Characterizing multiple independent behavioral correlates of cell firing in freely moving animals. *Hippocampus* **15,** 149–53 (2005).

28. Taube, J. S. The head direction signal: origins and sensory-motor integration. *Annu. Rev. Neurosci.* **30,** 181–207 (2007).

29. Morris, R. G. M. Spatial localization does not require the presence of local cues. *Learn. Motiv.* **12,** 239–260 (1981).

30. Morris, R. G. M., Garrud, P., Rawlins, J. N. P. & O'Keefe, J. Place navigation impaired in rats with hippocampal lesions. *Nature* **297,** 681 – 683 (1982).

31. Pinnell, R. C., Almajidy, R. K., Kirch, R. D., Cassel, J. C. & Hofmann, U. G. A Wireless EEG Recording Method for Rat Use inside the Water Maze. *PLoS One* **11,** e0147730 (2016).

32. Korshunov, V. A. & Averkin, R. G. A method of extracellular recording of neuronal activity in swimming mice. *J. Neurosci. Methods* **165,** 244–250 (2007).

33. Korshunov, V. A. Miniature multichannel preamplifier for extracellular recordings of single unit activity in freely moving and swimming small animals. *J. Neurosci. Methods* **206,** 15–22 (2012).

34. Ravassard, P. *et al.* Multisensory control of hippocampal spatiotemporal selectivity. *Science* **340,** 1342–6 (2013).

35. Cushman, J. D. *et al.* Multisensory Control of Multimodal Behavior: Do the Legs Know What the Tongue Is Doing? *PLoS One* **8,** e80465 (2013).

36. Aghajan, Z. M. *et al.* Impaired spatial selectivity and intact phase precession in two-dimensional virtual reality. *Nat. Neurosci.* **18,** 121–8 (2015).

37. Acharya, L. *et al.* Causal Influence of Visual Cues on Hippocampal Article Causal Influence of Visual Cues on Hippocampal Directional Selectivity. *Cell* **164,** 197–207 (2016).

38. Ramón y Cajal, S. *Histologie du systeme nerveux de l'homme & des vertebres*. (Rue de l'ecole-de-medecine, 1909).

39. Spencer, W. A. & Kandel, E. R. Electrophysiology of Hippocampal Neurons: IV. Fast Prepotentials. *Public Health* (1960).

40. Amitai, Y., Friedman, A., Connors, B. W. & Gutnick, M. J. Regenerative activity in apical dendrites of pyramidal cells in neocortex. *Cereb. Cortex* **3,** 26–38 (1993).

41. Kamondi, A., Acsády, L. & Buzsáki, G. Dendritic spikes are enhanced by cooperative network activity in the intact hippocampus. *J. Neurosci.* **18,** 3919–3928 (1998).

42. Larkum, M. E. & Zhu, J. J. Signaling of layer 1 and whisker-evoked Ca2+ and Na+ action potentials in distal and terminal dendrites of rat neocortical pyramidal neurons in vitro and in vivo. *J. Neurosci.* **22,** 6991–7005 (2002).

43. Jarsky, T., Roxin, A., Kath, W. L. & Spruston, N. Conditional dendritic spike propagation following distal synaptic activation of hippocampal CA1 pyramidal neurons. *Nat. Neurosci.* **8,** 1667–76 (2005).

44. Nevian, T., Larkum, M. E., Polsky, A. & Schiller, J. Properties of basal dendrites of layer 5 pyramidal neurons: a direct patch-clamp recording study. *Nat. Neurosci.* **10,** 206–14 (2007).

45. Larkum, M. E., Waters, J., Sakmann, B. & Helmchen, F. Dendritic spikes in apical dendrites of neocortical layer 2/3 pyramidal neurons. *J. Neurosci.* **27,** 8999–9008 (2007).

46. Ledergerber, D. & Larkum, M. E. Properties of layer 6 pyramidal neuron apical dendrites. *J. Neurosci.* **30,** 13031–44 (2010).

47. Golding, N. L. & Spruston, N. Dendritic sodium spikes are variable triggers of axonal action potentials in hippocampal CA1 pyramidal neurons. *Neuron* **21,** 1189–1200 (1998).

48. Golding, N. L., Staff, N. P. & Spruston, N. Dendritic spikes as a mechanism for cooperative long-term potentiation. *Nature* **418,** (2002).

49. Kim, Y., Hsu, C.-L., Cembrowski, M. S., Mensh, B. D. & Spruston, N. Dendritic sodium spikes are required for long-term potentiation at distal synapses on hippocampal pyramidal neurons. *Elife* **4,** (2015).

50. Stuart, G. J. & Sakmann, B. Active propagation of somatic action potentials into neocortical pyramidal cell dendrites. *Nature* **367,** 69–72 (1994).

51. Colbert, C. M., Magee, J. C., Hoffman, D. A. & Johnston, D. Slow recovery from inactivation of Na+ channels underlies the activity-dependent attenuation of dendritic action potentials in hippocampal CA1 pyramidal neurons. *J. Neurosci.* **17,** 6512–21 (1997).

52. Golding, N., Kath, W. & Spruston, N. Dichotomy of action-potential backpropagation in CA1 pyramidal neuron dendrites. *J. Neurophysiol* **86,** (2001).

53. Waters, J., Larkum, M., Sakmann, B. & Helmchen, F. Supralinear Ca2+ influx into dendritic tufts of layer 2/3 neocortical pyramidal neurons in vitro and in vivo. *J. Neurosci.* **23,** 8558–67 (2003).

54. Kumar, A. & Mehta, M. R. Frequency-Dependent Changes in NMDAR-Dependent Synaptic Plasticity. *Front. Comput. Neurosci.* **5,** 38 (2011).

55. Sakmann, B. & Neher, E. Patch clamp techniques for studying ionic channels in excitable membranes. *Annu. Rev. Physiol.* **46,** 455–472 (1984).

56. DeWeese, M. R. Whole-cell recording in vivo. *Curr. Protoc. Neurosci.* **Chapter 6,** Unit 6.22 (2007).

57. Alcami, P., Franconville, R., Llano, I. & Marty, A. Measuring the firing rate of high-resistance neurons with cell-attached recording. *J. Neurosci.* **32,** 3118–30 (2012).

58. Helmchen, F., Svoboda, K., Denk, W. & Tank, D. W. In vivo dendritic calcium dynamics in deep-layer neocortical pyramidal neurons. *Nature* **2,** 989–996 (1999).

59. Smith, S. L., Smith, I. T., Branco, T. & Häusser, M. Dendritic spikes enhance stimulus selectivity in cortical neurons in vivo. *Nature* **503,** 115–20 (2013).

60. Regehr, W. G., Pine, J., Cohan, C. S., Mischke, M. D. & Tank, D. W. Sealing cultured invertebrate neurons to embedded dish electrodes facilitates long-term stimulation and recording. *J. Neurosci. Methods* **30,** 91–106 (1989).

61. Hai, A., Shappir, J. & Spira, M. E. Long-term, multisite, parallel, in-cell recording and stimulation by an array of extracellular microelectrodes. *J. Neurophysiol.* **104,** 559–568 (2010).

62. Szarowski, D. H., Andersen, M. D., Retterer, S., Spence, A. J. & Isaacson, M. Brain responses to micro-machined silicon devices. *Brain Res.* **983,** 23–35 (2003).

63. Polikov, V. S., Tresco, P. A. & Reichert, W. M. Response of brain tissue to chronically implanted neural electrodes. *J. Neurosci. Methods* **148,** 1–18 (2005).

64. Gillespie, J. S. The electrical and mechanical responses of intestinal smooth muscle cells to stimulation of their extrinsic parasympathetic nerves. *J. Phy* 76–92 (1962).

65. Mcilwain, J. T. & Creutzfeldt, O. D. Microelectrode Study of Synaptic Excitation and Inhibition in the Lateral Geniculate Nucleus of the Cat. *J. Neurophysiol.* **30,** 1–21 (1967).

66. Singer, W. & Creutzfeldt, O. D. Reciprocal lateral inhibition of on- and off-center neurones in the lateral geniculate body of the cat. *Exp. Brain Res.* **10,** 311–330 (1970).

67. Coenen, A. M. L. & Vendrik, A. J. H. Determination of the transfer ratio of cat's geniculate neurons through quasi-intracellular recordings and the relation with the level of alertness. *Exp. Brain Res.* **14,** 227–242 (1972).

68. Finch, D. M., Derian, E. L. & Babb, T. L. Excitatory projection of the rat subicular complex to the cingulate cortex and synaptic integration with thalamic afferents. *Brain Res.* **301,** 25–37 (1984).

69. Henze, D. A. *et al.* Intracellular features predicted by extracellular recordings in the hippocampus in vivo. *J. Neurophysiol.* **84,** 390–400 (2000).

70. Gold, C., Girardin, C. C., Martin, K. A. C. & Koch, C. High-amplitude positive spikes recorded extracellularly in cat visual cortex. *J. Neurophysiol.* **102,** 3340–51 (2009).

71. Williams, J. C., Hippensteel, J. A., Dilgen, J., Shain, W. & Kipke, D. R. Complex impedance spectroscopy for monitoring tissue responses to inserted neural implants. *J. Neural Eng.* **4,** 410–423 (2007).

72. Lempka, S. F., Miocinovic, S., Johnson, M. D., Vitek, J. L. & McIntyre, C. C. In vivo impedance spectroscopy of deep brain stimulation electrodes. *J. Neural Eng.* **6,** 046001 (2009).

73. Harvey, C. D., Collman, F., Dombeck, D. A. & Tank, D. W. Intracellular dynamics of hippocampal place cells during virtual navigation. *Nature* **461,** 941–946 (2009).

74. Lee, A. K., Manns, I. D., Sakmann, B. & Brecht, M. Whole-cell recordings in freely moving rats. *Neuron* **51,** 399–407 (2006).

75. Jones, M. W. & Wilson, M. A. Theta rhythms coordinate hippocampal-prefrontal interactions in a spatial memory task. *PLoS Biol.* **3,** 1–13 (2005).

76. Hamill, O. P., Huguenard, J. R. & Prince, D. A. Patch-clamp studies of voltage-gated currents in identified neurons of the rat cerebral cortex. *Cereb. Cortex* **1,** 48–61 (1991).

77. Kaiser, K. M. M., Zilberter, Y. & Sakmann, B. Back-propagating action potentials mediate calcium signalling in dendrites of bitufted interneurons in layer 2/3 of rat somatosensory cortex. *J. Physiol.* **535,** 17–31 (2001).

78. Saraga, F., Wu, C. P., Zhang, L. & Skinner, F. K. Active dendrites and spike propagation in multi-compartment models of oriens-lacunosum/moleculare hippocampal interneurons. *J. Physiol.* **552,** 673–89 (2003).

79. Douglas, R. J. & Martin, K. A. C. Neuronal circuits of the neocortex. *Annu. Rev. Neurosci.* **27,** 419–451 (2004).

80. Petersen, C. C. H., Hahn, T. T. G., Mehta, M. R., Grinvald, A. & Sakmann, B. Interaction of sensory responses with spontaneous depolarization in layer 2/3 barrel cortex. *Proc. Natl. Acad. Sci. U. S. A.* **100,** 13638–43 (2003).

81. Azouz, R. & Gray, C. M. Dynamic spike threshold reveals a mechanism for synaptic coincidence detection in cortical neurons in vivo. *Proc. Natl. Acad. Sci. U. S. A.* **97,** 8110–8115 (2000).

82. Constantinople, C. M. & Bruno, R. M. Effects and mechanisms of wakefulness on local cortical networks. *Neuron* **69,** 1061–1068 (2011).

83. Chauvette, S., Crochet, S., Volgushev, M. & Timofeev, I. Properties of slow oscillation during slow-wave sleep and anesthesia in cats. *J. Neurosci.* **31,** 14998–5008 (2011).

84. Whitlock, J. R., Pfuhl, G., Dagslott, N., Moser, M. B. & Moser, E. I. Functional split between parietal and entorhinal cortices in the rat. *Neuron* **73,** 789–802 (2012).

85. Muller, R. U. & Kubie, J. L. The firing of hippocampal place cells predicts the future position of freely moving rats. *J. Neurosci.* **9,** 4101–10 (1989).

86. Rao, R. P. & Ballard, D. H. Predictive coding in the visual cortex: a functional interpretation of some extra-classical receptive-field effects. *Nat. Neurosci.* **2,** 79–87 (1999).

87. Engert, F., Tao, H. W., Zhang, L. I. & Poo, M. Moving visual stimuli rapidly induce direction sensitivity of developing tectal neurons. *Nature* **419,** 470–475 (2002).

88. Lenschow, C. & Brecht, M. Barrel Cortex Membrane Potential Dynamics in Social Touch. *Neuron* **85,** 1–8 (2015).

89. Margrie, T. W., Brecht, M. & Sakmann, B. In vivo, low-resistance, whole-cell recordings from neurons in the anaesthetized and awake mammalian brain. *Pflugers Arch.* **444,** 491–8 (2002).

90. Lee, D., Lin, B. J. & Lee, A. K. Hippocampal Place Fields Emerge upon Single-Cell Manipulation of Excitability During Behavior. *Science* **337,** 849–853 (2012).

91. Schmidt-Hieber, C. & Häusser, M. Cellular mechanisms of spatial navigation in the medial entorhinal cortex. *Nat. Neurosci.* **16,** 325–31 (2013).

92. Linsker, R. Neural network learning of optimal Kalman prediction and control. *Neural Networks* **21,** 1328–1343 (2008).

93. Deneve, S. Bayesian spiking neurons I: Inference. *Neural Comput.* **20,** 118–145 (2008).

94. Angelo, K. & Margrie, T. W. Population diversity and function of hyperpolarization-activated current in olfactory bulb mitral cells. *Sci. Rep.* **1,** 1–11 (2011).

95. Hubel, D. H. & Wiesel, T. N. Receptive fields of single neurones in the cat's striate cortex. *J. Physiol.* **148,** 574–591 (1959).

96. Merzenich, M. M., Knight, P. L. & Roth, G. L. Representation of cochlea within primary auditory cortex in the cat. *J. Neurophysiol.* **38,** 231–249 (1975).

97. Cacucci, F. Theta-Modulated Place-by-Direction Cells in the Hippocampal Formation in the Rat. *J. Neurosci.* **24,** 8265–8277 (2004).

98. Lepage, K. Q., Macdonald, C. J., Eichenbaum, H. & Eden, U. T. The statistical analysis of partially confounded covariates important to neural spiking. *J. Neurosci. Methods* **205,** 295–304 (2012).

99. MacDonald, C. J., Lepage, K. Q., Eden, U. T. & Eichenbaum, H. Hippocampal 'time cells' bridge the gap in memory for discontiguous events. *Neuron* **71,** 737–49 (2011).

100. Truccolo, W., Eden, U. T., Fellows, M. R., Donoghue, J. P. & Brown, E. N. A point process framework for relating neural spiking activity to spiking history, neural ensemble, and extrinsic covariate effects. *J. Neurophysiol.* **93,** 1074–89 (2005).

101. Nitz, D. A. Spaces within spaces: rat parietal cortex neurons register position across three reference frames. *Nat. Neurosci.* **15,** 1365–7 (2012).

102. Schwarz, G. Estimating the Dimension of a Model. *Ann. Stat.* **6,** 461–464 (1978).

103. Sutherland, R. J. & Dyck, R. H. Place navigation by rats in a swimming pool. *Can. J. Psychol.* **38,** 322–347 (1984).

104. Jeffery, K. J. & Morris, R. G. M. Cumulative long-term potentiation in the rat dentate gyrus correlates with, but does not modify, performance in the water maze. *Hippocampus* **3,** 133–40 (1993).

105. Moser, E. I., Krobert, K. A, Moser, M. B. & Morris, R. G. Impaired spatial learning after saturation of long-term potentiation. *Science* **281,** 2038–2042 (1998).

106. Morris, R. G. M., Anderson, E., Lynch, G. S. & Baudry, M. Selective impairment of learning and blockade of long-term potentiation by an N-methyl-D-aspartate receptor antagonist, AP5. *Nature* **319,** 774–776 (1986).

107. Bannerman, D. M., Good, M. A., Butcher, S. P., Ramsay, M. & Morris, R. G. M. Distinct components of spatial learning revealed by prior training and NMDA receptor blockade. *Nature* **378,** 182–186 (1995).

108. Wehner, J. M., Sleight, S. & Upchurch, M. Hippocampal protein kinase C activity is reduced in poor spatial learners. *Brain Res.* **523,** 181–187 (1990).

109. Vorhees, C. V *et al.* Adult learning deficits after neonatal exposure to D-methamphetamine: selective effects on spatial navigation and memory. *J. Neurosci.* **20,** 4732–9 (2000).

110. Broening, H. W., Morford, L. L., Inman-Wood, S. L., Fukumura, M. & Vorhees, C. V. 3,4-Methylenedioxymethamphetamine (Ecstasy)-Induced Learning and Memory Impairments Depend on the Age of Exposure During Early Development. *J. Neurosci.* **21,** 3228–35 (2001).

111. Grant, S. G. N. *et al.* Impaired Long-Term Potentiation, Spatial Learning, and Hippocampal Development in fyn Mutant Mice. *Science* **258,** 1903–1910 (1992).

112. Hollup, S. A., Kjelstrup, K. G., Hoff, J., Moser, M.-B. & Moser, E. I. Impaired Recognition of the Goal Location during Spatial Navigation in Rats with Hippocampal Lesions. *J. Neurosci.* **21,** 4505–4513 (2001).

113. Yang, J. *et al.* Acute behavioural stress facilitates long-term depression in temporoammonic-CA1 pathway. *Neuroreport* **17,** 753–7 (2006).

114. Aleisa, A. M., Alzoubi, K. H., Gerges, N. Z. & Alkadhi, K. a. Nicotine blocks stress-induced impairment of spatial memory and long-term potentiation of the hippocampal CA1 region. *Int. J. Neuropsychopharmacol.* **9,** 417–26 (2006).

115. Kim, J. J., Diamond, D. M., Haven, N. & Blvd, B. B. D. The stressed hippocampus, synaptic plasticity and lost memories. *Nat. Rev. Neurosci.* **3,** 453–62 (2002).

116. Foy, M. R., Stanton, M. E., Levine, S. & Thompson, R. F. Behavioral stress impairs long-term potentiation in rodent hippocampus. *Behav. Neural Biol.* **48,** 138–149 (1987).

117. Yang, C.-H., Huang, C.-C. & Hsu, K.-S. Behavioral Stress Enhances Hippocampal CA1 Long-Term Depression through the Blockade of the Glutamate Uptake. *J. Neurosci.* **25,** 4288–4293 (2005).

118. Wilent, W. B. & Nitz, D. A. Discrete place fields of hippocampal formation interneurons. *J. Neurophysiol.* **97,** 4152–4161 (2007).

119. Pfeiffer, B. E. & Foster, D. J. Hippocampal place-cell sequences depict future paths to remembered goals. *Nature* (2013).

120. Buzsáki, G. Hippocampal sharp wave-ripple: A cognitive biomarker for episodic memory and planning. *Hippocampus* **25,** 1073–1188 (2015).

121. Devan, B. D., Goad, E. H. & Petri, H. L. Dissociation of hippocampal and striatal contributions to spatial navigation in the water maze. *Neurobiol. Learn. Mem.* **66,** 305–323 (1996).

122. Valerio, S. & Taube, J. S. Path integration: how the head direction signal maintains and corrects spatial orientation. *Nat. Neurosci.* **15,** 1445–53 (2012).

123. Loomis, J. M., Klatzky, R. L., Golledge, R. G. & Philbeck, J. W. in *Wayfinding Behav. Cogn. Mapp. Other Spat. Process.* (Golledge, R. G.) 125–151 (Johns Hopkins Univer, 1999).